Title

Cosmic Choreography: Rethinking the Complex Dynamics of Common Envelope Binaries

Author

Everson, Rosa Wallace

Publication Date

2024

UNIVERSITY OF CALIFORNIA
SANTA CRUZ

COSMIC CHOREOGRAPHY: RETHINKING THE COMPLEX DYNAMICS OF COMMON ENVELOPE BINARIES

A dissertation submitted in partial satisfaction
of the requirements for the degree of

DOCTOR OF PHILOSOPHY

in

ASTRONOMY AND ASTROPHYSICS

by

Rosa Wallace Everson

June 2024

The Dissertation of Rosa Wallace Everson
is approved:

Ruth Murray-Clay, Chair

Silvia Toonen

Ryan J. Foley

Enrico Ramirez-Ruiz

Peter F. Biehl
Vice Provost and Dean of Graduate Studies

Table of Contents

List of Figures

Abstract

Cosmic Choreography: Rethinking the Complex Dynamics of Common Envelope Binaries

by

Rosa Wallace Everson

In the era of transient, multimessenger astrophysics, dramatic interactions between stellar partners are an essential ingredient in the production of the fantastic light show to which we bear witness. Common envelope interactions, in which a star engulfs a companion, are commonly invoked as the presumed formation channel of numerous exotic close binaries and merger products, from binary black holes to too-bright Algol-type stars and the elusive Thorne-Żytkow object. In this dissertation, I apply a combination of semi-analytical models and high-resolution hydrodynamical simulations in different dimensionalities to understand the role of inspiral dynamics in defining post-common envelope outcomes and to further the development of a fully descriptive, predictive theoretical framework for common envelope. I first define the range of applicability for the common envelope drag formalism, which offers a potential alternative to both global simulations and the oversimplified energy formalism in widespread use to model common envelope outcomes. I then develop a semi-analytical framework as an alternative to the energy formalism that incorporates the physical timescales most relevant to common envelope inspiral to predict how a common envelope event will proceed. Shifting to a focus on specific outcomes, I present a numerical framework that combines one- and three-dimensional hydrodynamics to capture the computationally restrictive range of timescales relevant to stellar mergers, constraining the origins of the B[e] supergiant R4 in the Small Magellanic Cloud as a post-common envelope merger product. Finally, I demonstrate through analytical and numerical modeling of merger via common envelope that Thorne-Żytkow objects are likely not a product of common envelope evolution in field binaries.

For my family.

Personal Acknowledgments

Graduate school is a very personal journey, even if no one makes that journey alone. Though its stated goal is, of course, the production of science, this process has taught me the most about myself: about the internal shape and practice of work, attention, dedication, courage, friendship, purpose, advocacy, authenticity, humility, independence, and the power of showing up. I wasn't always sure that I would reach the end of this journey, but through the collective love and support of many exceptional human beings, this, too, was possible.

First and foremost, I express profound love and thanks to my family. *Mike*, this never could have happened without your unwavering belief in my abilities as a student and a scientist. Even though life has presented us with unimaginable crises and heartbreaks, your ability to stand strong, listen, and always return to love has built the foundation for the beautiful life we share, enabling me to evolve and do the work I believe is important in the world. Thank you for making me laugh. I love you, all the way. *Maple*, you are a bright star in my heart, and no small part of the efforts in this book are motivated by the desire to show you that you can do what you set your mind to. It's not important that things be easy, but that they feel purposeful, and help you grow while giving back in some way. Your patience, generosity, and love astound me everyday, and I am blessed to get to spend this little bit of our lives together.

To my mom, you have accepted me through so many seasons of life that I was surprised when you took this idea seriously. I never would have thought it possible if I hadn't seen you find a way to get there yourself, but I am grateful that you did. I will never forget all that you have done to support me, and Maple since she was born, going above and beyond with wisdom, courage, and care. *To my stepfather Tom*, without your support and guidance, the life we have now would not be a reality. Thank you for providing a stable foundation for us, and for believing in me. I deeply appreciate and love you both.

To my dad, you've been my biggest cheerleader for as long as I can remember, even when I was taking phones apart to sate my curiosity. I know this work will make you proud. I love you.

What brought me to the Astronomy & Astrophysics Department at UC Santa Cruz was its people, and I have never doubted that I chose wisely. I am eternally grateful for the precious time I was able to spend with my dear friends and colleagues here. *Dave and Maggie*, I love you both, and it was my great pleasure to press the boundaries of knowledge alongside you in our little slice of caffeinated paradise. *Anne and Sophie*, even when we're half a world apart, this journey has been so much brighter because of the time we shared talking science and talking life. *Jamie and Diana*, I couldn't be more proud to be a part of whatever it is y'all are creating in the world, and I can't wait to see where life takes your beautiful family! *Evan*, your friendship has been priceless through incredibly challenging times, and you will always be family. *César*, you were my first friend in Santa Cruz, and your companionship and support helped me make it through the uncertainty of those first two years. I am so proud of you, and I'll never forget our time together. *Monine*, I am honored to count you as a dear friend. I adore you, appreciate all you have taught me, and can't wait to see what you pursue in your next chapter. *Ricardo*, thank you for being such a thoughtful and supportive friend and colleague through the years- I am delighted that there's more we get to work on together! *Sam*, your brilliance and diligence are truly inspiring. Thank you for your generosity in including the work we've done together in this text. *Sierra and Alex*, your futures are so bright- I cherish the little moments we've had along the way and am thrilled to see you create lives that are dazzling reflections of the incredible humans you are.

To my advisor, Enrico: You have changed the course of my life. Your conviction and advocacy have given me so much to live up to, and you have welcomed me into the fold of an incredible network of impressive scientists and thinkers that believe, like me, that science can be a conscious, human-centered endeavor. Your support made all of this possible for me and for my family. Thank you, thank you, thank you, for all that you've done for us. You are forever a part of *mi familia*.

To my Committee: Thank you so much for your insight, advice, patience, and support in navigating my journey to PhD.

To Deana: It can be rare in this line of work to find people that are acting from the heart. Getting to know you has felt like a port in the storm, and I am forever grateful for our heart-to-hearts and for your generous support through the labyrinthine processes that come with academia. Keep shining your light, friend.

Published Work

The text of this dissertation includes reprints of the following previously published or publicly released material led by myself, with the permission of the listed coauthors.

Chapter 2 was published in the literature as Everson et al. (2020). I was responsible for writing modeling and analysis code, generating the models, performing the analysis, writing the text, and creating all figures. I wish to thank coauthors Morgan MacLeod, Soumi De, Phillip Macias, and Enrico Ramirez-Ruiz for their guidance and feedback in the course of this research.

Chapter 4 was published in the literature as Wu et al. (2020), led by Samantha Chloe Wu and co-advised by myself. My role included defining the scope of the project, generating models, co-developing the numerical framework and mapping techniques, and assisting in outlining and writing the manuscript. I wish to thank coauthors Fabian Schneider, Philipp Podsiadlowski, and Enrico Ramirez-Ruiz for their technical guidance and support in the course of this research.

Chapter 5 was publicly released as Everson et al. (2023). I was responsible for writing simulation, modeling, and analysis code, generating models, running simulations, performing analysis, writing the text, and creating the figures. I wish to thank my coauthors Tenley Hutchinson-Smith, Alejandro Vigna-Gómez, and Enrico Ramirez-Ruiz for their support and insightful feedback in the course of this research.

Additionally, numerous coauthorship contributions have derived from this work, and have been published or publicly released in:

Rosselli-Calderon A., et al., 2024, arXiv:2404.08037
Hutchinson-Smith T., Everson R.W., et al., 2023, arXiv:2311.06741
Yarza R., et al., 2023, ApJ, 954, 176
Schrøder S.L., et al., 2021, arXiv:2107.09675
Law-Smith J.A.P., et al., 2020, arXiv:2011.06630
Murguia-Berthier A., et al., 2020, ApJL, 901, L24
De S., et al., 2020, ApJ, 897, 130

All of these works were led by early-career scientists, with that in boldface written in close collaboration: my role included developing core code for simulation, modeling, and analysis, assisting in writing the manuscript, and otherwise acting in an ongoing co-advisory role. These works are indicative of my collaborative, human-centered values and the productive and holistically supportive atmosphere I have endeavored to foster among my mentees, peers, students, and wider community while at UC Santa Cruz.

Scientific Acknowledgments

I gratefully acknowledge research support from the National Science Foundation Graduate Research Fellowship Program under Grant No. 1339067, with additional support from the National Science Foundation Grant Nos. 2150255 and 2307710, the University of California Eugene V. Cota-Robles Fellowship, the University of California President's Dissertation Year Fellowship, the Vera Rubin Presidential Chair for Diversity at UC Santa Cruz, the Heising-Simons Foundation, the Danish National Research Foundation (DNRF132), and the ARCS Foundation.

Calculations presented in this work used resources of the SCIENCE HPC Center at the University of Copenhagen, with the support of the DARK Cosmology Centre at the Niels Bohr Institute which hosted this research in part. I also acknowledge use of the lux supercomputer at UC Santa Cruz, funded by NSF MRI Grant AST1828315.

The 3D hydrodynamics software used in this work was developed in part by the DOE NNSA- and DOE Office of Science-supported Flash Center for Computational Science at the University of Rochester. Simulations in this work made use of the COMPAS rapid binary population synthesis code (version 02.13.01), which is freely available at `http://github.com/TeamCOMPAS/COMPAS`.

Chapter 1

Introduction

With the advent of high-cadence time-domain surveys and gravitational wave astronomy, we have entered an era of transient, multimessenger astrophysics in a dynamic universe evolving through an elaborate, cosmic dance. Many of the events that pluck the fabric of spacetime and explode into a cosmic light show are produced by the interactions of binary and multiple stellar systems. In order to effectively interpret the explosive interactions that will be observed by upcoming large-scale transient surveys, there is a pressing need for a better theoretical understanding of how these interactions proceed, especially in cases involving stellar binaries. Binaries undergoing common envelope episodes are the progenitors of some of the most exciting systems currently being studied, including gravitational wave sources, binary neutron stars, cataclysmic variables, and a wide range of optical transients. Common envelope interactions, in which a star engulfs a companion, are still very poorly understood and require complex 3D multi-physics simulations to capture the gas dynamics, yet those same simulations are not suitable to capture other important physical effects. A creative combination of the available numerical tools is necessary to capture the broad range of scales that are relevant to these events. In this dissertation, I present four major results from models and simulations of common envelope interactions with high-resolution hydrodynamics codes in different dimensionalities, tracking the evolution of a broad parameter space of interacting systems at all relevant scales through the strategic combination of analytical and 1D/3D numerical approaches.

In this chapter, context and motivation for the presented work is provided in Sections 1.1 and 1.2, followed by the outline (Section 1.3) of this dissertation.

1.1 Common Envelope: A Key to the Transient Universe

We now know that systems of multiple stars are much more common than we once imagined, with nearly half of solar-type stars (Moe & Di Stefano 2017) and the majority of massive stars (Sana et al. 2012, 2013a) forming with one or more companions. Though the evolution of individual main-sequence stars is well understood, the pervasiveness of binary and multiple-star systems demands that we reconsider our approach to stellar evolution, particularly for massive stars and the progenitors of the most exotic events and astrophysical objects we observe in the universe, by incorporating the impact of interactions between partners.

In stellar binaries, these interactions often involve mass exchange when one partner (hereafter, the primary) begins to expand as it leaves the main-sequence and its companion (hereafter, the secondary) begins accreting the primary's envelope material. Though the primary is typically a giant-branch star, the secondary may be a main-sequence star, stellar remnant, or planet. When this exchange becomes unstable, the envelope of the primary engulfs the secondary, creating a common envelope (CE, Paczynski 1976). Drag from the envelope then causes the orbit of the secondary to tighten, reducing the separation of the primary's core and the companion while depositing energy into the envelope. In some cases, this process continues until the secondary is tidally disrupted or a merger occurs; in others, the energy deposited is sufficient to unbind the CE and end the interaction with the secondary closely orbiting a stripped stellar core (see, e.g., Ivanova et al. 2013). A schematic of a CE interaction is shown in Figure 1.1.

This dynamic phase of interaction appears throughout the universe as a key component in a broad range of transient astrophysical phenomena. The gravitational wave outbursts detected by the LIGO-Virgo collaboration are created by merging binary black holes and neutron stars (e.g., Abbott et al. 2019) that coalesce from remarkably close orbits: one of the primary formation channels for such close binaries is CE evolution (e.g., Vigna-Gómez et al. 2020; Belczynski et al. 2022). Red novae (RNe), luminous red novae (LRNe), and luminous fast blue optical transients (FBOTs) are all proposed to be CE events (Pastorello et al. 2019; Soker 2022). The explosive mergers of neutron

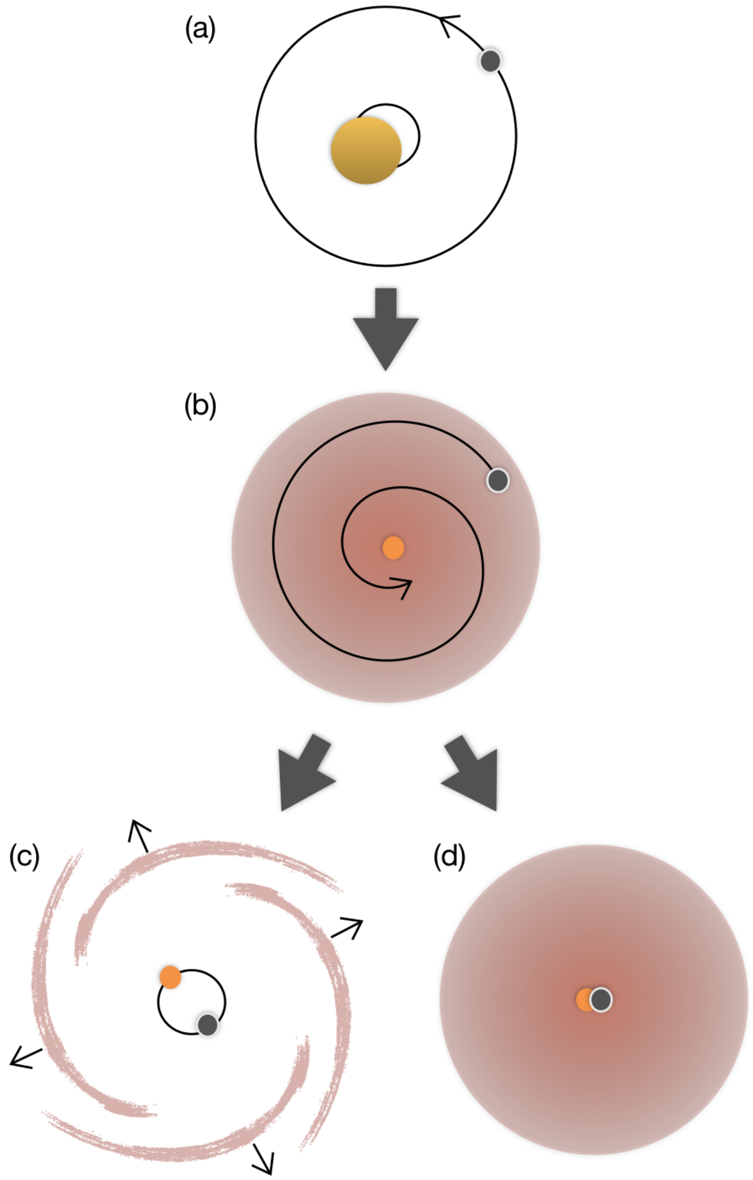

Figure 1.1 Schematic of CE evolution. (a) The envelope of a dying star begins to expand until (b) it engulfs its partner; drag acts on the partner and it plunges toward the stellar core until either (c) enough energy has been deposited to eject the envelope, leaving a close binary, or (d) a merger occurs.

stars with a stellar companion are fundamentally impacted by the CE phase (Everson et al. 2023), as well as planets being digested by their host star when it expands at the end of its stellar lifetime (Yarza et al. 2023). With the Vera Rubin Observatory coming online in the near future, many of these transients will be detectable with paradigm-changing time resolution and detection rates: in the case of LRNe alone, we are expected to go from less than a dozen known events to 500 detections per year (Howitt et al. 2020). The future of astronomy is in the time-domain, making detailed models and deep understanding of CE events essential to our ability to interpret the fantastic light show of the transient universe.

1.2 The Challenging Problem of Common Envelope Evolution

A comprehensive understanding of CE has remained elusive over nearly a half century of investigation, largely because the relevant physical and temporal scales in a CE event span many orders of magnitude (Ivanova et al. 2013). To illustrate, the relevant timescales range from that of the late-stage evolution of the primary ($\sim 10^6$ years) to the dynamical timescale of the stellar core (~ 20 seconds), and the relevant spatial scales range from the size of a neutron star ($\sim 10^6$ cm) to the size of a star at the tip of the giant branch ($\sim 10^{13}$ cm). Spiral shockwaves and the complex morphology of ejecta make CE an inherently three-dimensional (3D) problem, but even if we are confident of all pertinent physical processes, numerical limitations make it impossible to carry out global 3D simulations that can fully incorporate the physics on such a vast array of scales (Röpke & De Marco 2023).

Largely, our understanding of CE has progressed via a series of simplified models that either leave out various applicable physical processes or reduce the dimensionality of the problem to the point that results may not be broadly meaningful. For example, by far the most commonly used approach for calculating how CE events will progress is known as the energy formalism: a simple one-dimensional (1D) balance between the binding energy of the envelope of the primary and the cumulative orbital energy lost by the secondary through orbital tightening (van den Heuvel 1976; Webbink 1984):

$$E_{\mathrm{bind}} \leq \alpha \Delta E_{\mathrm{orb}}, \tag{1.1}$$

in which the change in orbital energy is modified by an efficiency term α to account for energy sources and sinks, such as losses due to radiation or contributions from recombination (for a detailed introduction, see Subsection 3.2.1).

The story goes, if the deposition of orbital energy via shocks is sufficient to overcome the envelope's binding energy, the envelope will be ejected. This is a gross oversimplification of the CE process and has so far been completely unsupported by simulation results (see Ivanova et al. 2020; Röpke & De Marco 2023, and references therein), but the energy formalism remains popular due to a lack of viable alternatives and the simplicity of parameterizing all unknowns into the efficiency term. 1D stellar evolution calculations are also widely used, which may incorporate all relevant physics but cannot capture the effects of rotation, spiral shocks, and other non-symmetrical features. Even in 3D hydrodynamic simulations of CE, simplified stellar models and polytropes are most often used due to numerical limitations. As with any multi-scale, multi-physics problem, a solution is required that can creatively make use of the available computational resources while ensuring that essential physical processes are not being excluded.

An innovative approach to increasing resolution around the secondary and avoiding the numerical losses seen in global 3D CE simulations was introduced by MacLeod & Ramirez-Ruiz (2015b), using a 3D "wind tunnel" setup that centers the domain on the embedded secondary as an idealized envelope flows past in the moving frame of reference (Figure 1.2). Their approach adapted the framework for flows and accretion developed by Hoyle & Lyttleton (1939) and Bondi & Hoyle (1944) for CE events, and detailed drag force and accretion measurements led to the development of the CE drag formalism (MacLeod et al. 2017b; De et al. 2020). This formalism provides a suite of drag and accretion coefficients that can be applied in CE inspiral calculations using 1D stellar profiles, and has led to remarkable results linking the density gradient of the envelope to increased drag and reduced accretion during inspiral, explaining the mass distribution of post-CE binary neutron stars (MacLeod & Ramirez-Ruiz 2015a) and revealing the potential of CE as a formation chan-

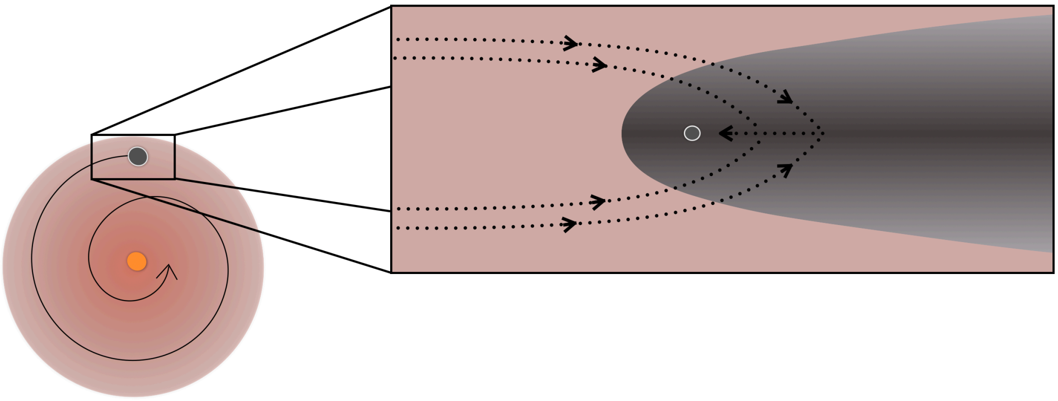

Figure 1.2 Schematic of the CE drag formalism "wind tunnel" setup, in which the computational domain centers on the embedded secondary as the stellar envelope flows past. In a medium of uniform density, the shock formed in the flow will be symmetrical, encouraging a high accretion rate onto the secondary. The presence of density gradients in realistic stellar envelopes breaks this symmetry, leading to increased drag and decreased accretion rates.

nel for LIGO-type binary black holes due to jet suppression (Murguia-Berthier et al. 2017). The results from the CE drag formalism provide the foundation for the work presented here with a unique perspective that infuses the dynamics of inspiral into the standard analytical treatments for CE evolution, and has inspired further development of the formalism in the domains of planetary engulfment (Yarza et al. 2023) and triple system CE evolution (Rosselli-Calderon et al. 2024).

In the last decade, the study of CE has gained momentum largely due to the effort to explain the progenitor systems of close LIGO-type progenitor binaries (e.g., Kruckow et al. 2016; Ivanova 2017; Ricker et al. 2019) with a focus on envelope ejection, but the role of CE in mergers should not be ignored. Many of the most intriguing transients in the night sky are produced via merger, with CE dynamics playing a crucial role in the resulting ejecta and electromagnetic signatures of these events (e.g., MacLeod et al. 2017a). Interest has also renewed in recent years in exotic merger products, such as Thorne-Żytkow objects (TŻO; see, e.g., Levesque et al. 2014; O'Grady et al. 2023; Hutchinson-Smith et al. 2023) and Algol-type systems (e.g., Wu et al. 2020; van Rensbergen & de Greve 2021; Sen et al. 2023), which often have CE invoked to explain their formation. Studying CE events that are both successful and unsuccessful at envelope ejection will holistically develop our understanding of the impact of the CE phase on the evolution of a broad range of systems and ultimately determine what factors dominate post-CE outcomes.

1.3 Outline

This dissertation is structured as follows.

In Chapter 2, I demonstrate the self-similarity of dynamical inspiral across a broad range of CE events in a dimensionless parameter space informed by envelope drag, which presents the possibility that CE inspiral may be modeled without the use of stellar profiles. This has implications for the prescriptions used for CE events in binary population synthesis, as it suggests a method informed by inspiral dynamics rather than energy balance alone.

In Chapter 3, I develop an alternative framework for the analysis of CE inspiral and prediction of CE ejection, with promising results when compared to 3D hydrodynamical simulations. Though this framework does require the use of stellar profiles, it is an additional step forward in the pursuit of an alternative to the CE energy formalism.

In Chapter 4, I present a flexible numerical framework that maps results from a 3D, core-resolved hydrodynamics setup utilizing a realistic equation of state to a 1D hydrodynamic stellar evolution code to follow the evolution of a CE system through stages dominated by the dynamical and thermal timescales. As proof-of-concept, the origin of the B[e] supergiant R4 in the Small Magellanic Cloud is constrained as a post-CE merger product.

In Chapter 5, I present the results of a broad study on the implications of the CE phase on the formation of TŻOs from field binaries, suggesting that the CE formation channel does not produce TŻOs, but in fact may explain an interesting subset of X-ray sources and produce a series of transients with signatures across the electromagnetic spectrum during and after CE evolution.

I conclude and offer an outlook on compelling future directions of CE research in Chapter 6.

Chapter 2

Common Envelope Wind Tunnel: Range of Applicability and Self-Similarity in Realistic Stellar Envelopes

Abstract

Common envelope evolution, the key orbital tightening phase of the traditional formation channel for close binaries, is a multistage process that presents many challenges to the establishment of a fully descriptive, predictive theoretical framework. In an approach complementary to global 3D hydrodynamical modeling, we explore the range of applicability for a simplified drag formalism that incorporates the results of local hydrodynamic "wind tunnel" simulations into a semi-analytical framework in the treatment of the common envelope dynamical inspiral phase using a library of realistic giant branch stellar models across the low, intermediate, and high mass regimes. In terms of a small number of key dimensionless parameters, we characterize a wide range of common envelope events, revealing the broad range of applicability of the drag formalism as well its self-similar nature across mass regimes and ages. Limitations arising from global binary properties and local structural quantities are discussed together with the opportunity for a general prescriptive application for this formalism.

2.1 Introduction

It is well known that stars, rather than forming singly, are often formed in a binary or a triple system in which the stars orbit about their mutual center of mass (e.g. Sana et al. 2012; Toonen et al. 2016). The evolution and fate of individual main sequence stars are well understood, and in multi-body systems in which the stars are separated by large distances relative to their sizes, we expect them to evolve much as they would alone. However, the evolution of binary systems in which the stars are close enough to interact is not as well understood, largely due to the countless variations of possible parameters: initial separation, mass ratio, evolutionary stage, and so forth. Though we may establish limits to these parameters via observation, such limits are constrained largely to local short-period systems (close binaries).

However, close binaries in general are of great interest due to their role as possible precursors to many types of high-energy transients (see, e.g. Bethe & Brown 1998; Lee & Ramirez-Ruiz 2007; Dan et al. 2011; Postnov & Yungelson 2014), including binary neutron star and binary black hole mergers detected by LIGO (e.g. Abbott et al. 2019).

All close binary systems in which stellar remnants orbit at a separation smaller than the radii of their progenitor stars must have undergone some type of orbital transformation. In high stellar density regions, dynamical interactions may be a viable formation channel for close binaries (see, e.g. Samsing 2018; Rodriguez et al. 2018), and in binaries that initially form close to contact, chemically homogeneous evolution may forego the need for any tightening (see, e.g. Mandel & de Mink 2016), but in other cases orbital tightening of a pre-existing binary must be accomplished by one or more phases of common envelope (CE) evolution. A CE phase occurs when one member in a binary, hereafter called the primary, moves off the main sequence and expands beyond its Roche lobe, engulfing the other typically lower mass member, or secondary, and creates a system in which the core of the primary interacts with the secondary within a shared envelope (e.g. Paczynski 1976; Taam & Sandquist 2000; Taam & Ricker 2010; Ivanova et al. 2013; Iben & Livio 1993; Vigna-Gómez et al. 2020). Though the primary is always a star in its giant phase, the secondary may be a planet, a lower mass main sequence star, or any kind of stellar remnant.

Though several stages of CE evolution may occur for a given binary, there are only two final outcomes: either the envelope is ejected and binarity is preserved, or the envelope is not fully ejected and the secondary merges with the core of the primary. The structure of the envelope and the properties of the embedded secondary both play a role in deciding the outcome of CE evolution; decades of analytical and computational study have provided insight into precisely how, but still leave many questions unanswered (see Ivanova et al. 2013; Ivanova 2017, for extensive reviews).

Extensive work has been done to produce global 3D simulations of CE evolution (e.g. Ricker & Taam 2008, 2012; Passy et al. 2012; Nandez et al. 2014; Nandez & Ivanova 2016; Ivanova & Nandez 2016; Ohlmann et al. 2016b,a, 2017; Staff et al. 2015, 2016; Iaconi et al. 2017; Chamandy et al. 2018, 2019b,a; Prust & Chang 2019; Wu et al. 2020), but these efforts have faced many challenges, including (but not limited to) resolving adequately at all relevant physical scales, which span many orders of magnitude. An alternative and complementary approach has been developed by MacLeod & Ramirez-Ruiz (2015a,b); MacLeod et al. (2017b), and greatly extended by De et al. (2020) in a companion paper, to explore the local CE behavior around an embedded compact object using a "wind tunnel" morphology. This morphology, rather than modeling the plunge of the secondary through the envelope globally, focuses on a region centered on the (fixed) secondary in the interior of the envelope and subjects it to a wind representing the passing envelope material, reducing the relevant scales within the simulation domain. This is achieved numerically by modeling the secondary as a fixed, accreting compact object that is subject to a supersonic wind with a density structure consistent with polytropic extended stellar envelopes. Key flow parameters are described by specific dimensionless quantities as described in Section 2.3. Due to the use of Cartesian geometry, the "wind tunnel" approximation is appropriate only for systems in which the extent of gravitational influence of the embedded object on the envelope material is much less than the extent of the envelope itself.

The broad range of masses and configurations of systems that undergo CE evolution tend to be investigated in separate regimes due to the differences in possible outcomes, structure, and key physics of the objects that comprise each system. However, the dynamical inspiral phase appears to be governed by just a few dimensionless parameters (see Section 2.3.1) that can be calculated for any and all configurations for which the "wind tunnel" approximation is appropriate. Any self-similarity that exists in these parameters, regardless of the global characteristics of the binary, can be exploited via their connection to drag forces and accretion rates (De et al. 2020; MacLeod & Ramirez-Ruiz 2015a,b; MacLeod et al. 2017b) to constrain and inform models of the dynamical inspiral phase and binary properties at the end of that phase.

In this work, we examine a range of realistic stellar models in terms of these parameters to determine the range of applicability for the formalism of MacLeod et al. (2017b) and, by extension, the mapping of the results from De et al. (2020) to envelope parameters for the calculation of inspiral trajectories. In Section 2.2, we discuss the relevant aspects of late stage stellar evolution across mass regimes, noting key features that differentiate these regimes. In

Section 2.3, we present the flow parameters and numerical results that together makeup the "drag formalism" as established by MacLeod & Ramirez-Ruiz (2015a,b); MacLeod et al. (2017b) for which we seek to establish firm limits of applicability. In Section 2.4, we map a broad range of CE events into the parameter space defined by the drag formalism, detailing how the properties of realistic stellar envelopes allow for general use. We address in detail the limitations and exceptions that define the range of applicability in Section 2.5, including the validity of our results across additional model parameters and indications that the drag formalism naturally differentiates inspiral phases. In Section 2.6, we discuss how these results may be combined with those from De et al. (2020) to further application of the drag formalism.

2.2 Properties of Evolved Stars

In CE events, the primary has evolved beyond the main sequence into the giant branch. All stars in the giant branch have some structural similarities, namely extended, diffuse envelopes and a small, dense core that is no longer centrally burning hydrogen. However, the specifics of a given giant's structure vary widely depending on the mass and age of the star, in turn varying the applicable physics pertaining to energy transport in the envelope, distinguishing core from envelope, and of course, success or failure of envelope ejection, among other things. In exploring the limits of the drag formalism, which depends upon a few key dimensionless parameters, we first endeavor to

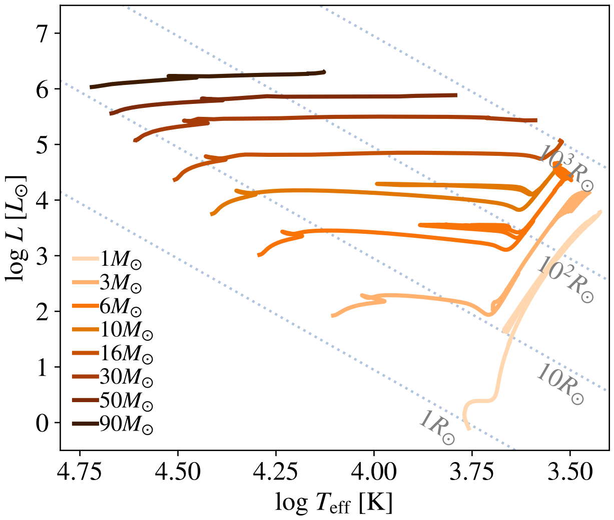

Figure 2.1 HR diagram of evolutionary tracks from ZAMS for a selection of primary stars used in this study. Contours of fixed radius are shown. For a given initial separation and mass ratio, primaries of vastly different mass are able to initiate a CE phase at some point in their post-main sequence evolution. However, the corresponding differences in envelope structure impact the dynamics and outcome of the CE phase in fundamental ways.

understand which similarities and differences in familiar structural terms are relevant to the dynamical inspiral phase of CE.

The HR diagram shown in Figure 2.1 traces the evolution from the zero-age main sequence (ZAMS), as simulated using the MIST package with `MESA` (for details, see Subsection 2.4.1), of a selection of stars across a mass range that spans two orders of magnitude. Stars of vastly different mass and evolutionary track can expand to similar extent, with implications for the traditional formation channel of close binaries and CE evolution. Stars of different mass will reach the same extent at different stages of their giant branch, with corresponding differences in envelope structure related to mass and evolutionary stage.

To make such a comparison, we look at a range of stars that have all reached an extent of $\approx 250R_\odot$. In Figure 2.2, envelopes are shown in the $\rho - T$ plane overplotted against adiabatic index and opacity values. Notably, none of the envelopes shown could be described as perfectly polytropic. In fact, the outer envelope often contains one or more regions of highly compressible material interspersed with convective or radiative regions, including density inversions that correspond to hydrogen and helium opacity peaks at $T \sim 5500$K and 13000K (Sanyal et al. 2015; Guzik et al. 2018). The differences in structure seen here affect key processes in CE evolution, namely orbital decay due to drag and the ability of released energy to escape the envelope (see, e.g. Wilson & Nordhaus 2019; Wilson & Nordhaus 2020; Grichener et al. 2018). How impactful these differences are on CE inspiral, however, is dependent on how much of the envelope contains these variations.

In Figure 2.3, we examine the structure of the same stellar profiles seen in Figure 2.2 in terms of the familiar structural quantities of sound speed and density against mass and radius. In mass coordinates, we can clearly see how the mass of each star is distributed differently, even amongst stars in the same mass regime. In the lower mass stars, the core-envelope boundary can be identified as a steep increase in density/sound speed, while in the higher mass stars a sharp, local peak in sound speed is the clearest indicator. This gives a sense of how much mass is held in the envelope, hence where the most binding energy lies within the star, and that the region relevant for CE inspiral contains only a fraction of the star's total mass, often less than half. In radial coordinates, the envelopes look similar in density structure, though

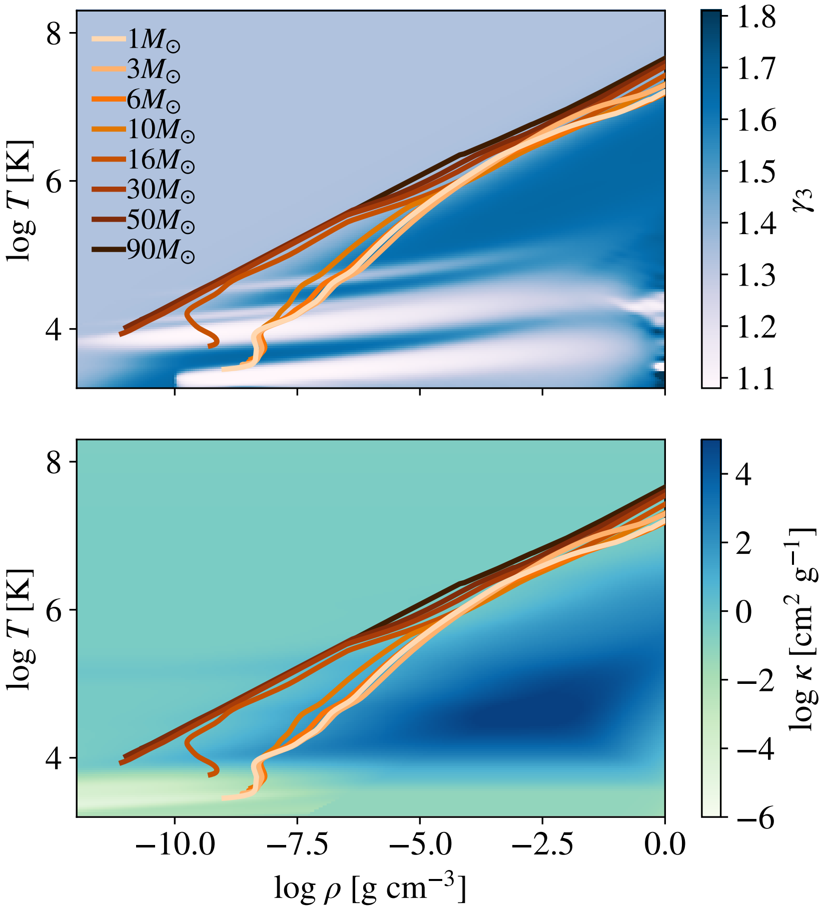

Figure 2.2 The selection of stars from Figure 2.1 shown in the ρ–T plane during the giant branch at $\approx 250R_\odot$. Initial stellar masses are labeled. Adiabatic index is shown in blue in the upper panel and log opacity is shown in blue and green in the lower panel. The core of each star lies outside the upper right of each panel while envelopes are shown. Density inversions near the limb are seen in the stars with mass $\leq 16M_\odot$ due to hydrogen and helium opacity peaks. In the upper panel, regions of low adiabatic index correspond to zones of partial ionization. For extended stars, the envelope equation of state tends to be dominated by convection ($\gamma \sim 5/3$) in lower mass stars and radiation pressure ($\gamma \sim 4/3$) in higher mass stars, seen here in the shift to lower adiabatic index for tracks of increasing mass. In the lower panel, the envelopes of more massive stars can be seen to have fairly constant opacity throughout, with more variability in those of lower mass stars.

the differences in sound speed impact the orbital decay during inspiral. Worth noting, however, are the minor density inversions that occur very close to the limb of most of these models, which coincide with the regions of highly compressible gas seen in white in Figure 2.2 and are an important consideration when choosing how to apply the drag formalism (for details, see Subsection 2.5.3).

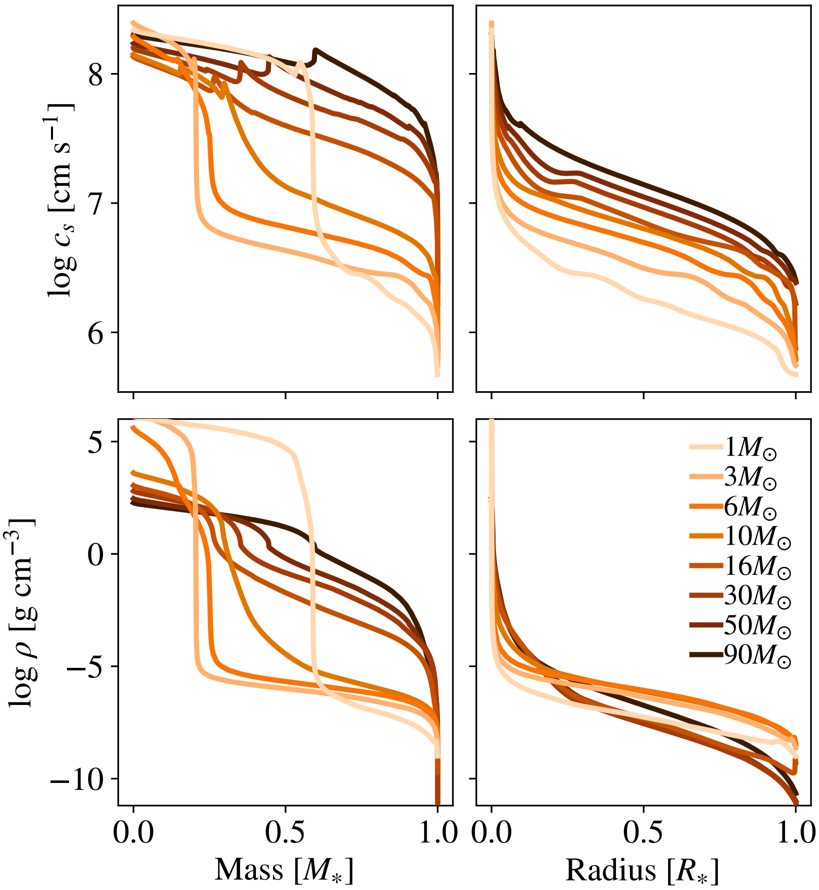

Figure 2.3 Selected giant branch stars extending to $\sim 250R_\odot$, with upper panels showing sound speed c_s and lower panels showing density in mass and radius coordinates. Differences in structure shown in mass coordinates are less apparent in radial coordinates, as these relate to core structure and how much relative mass is contained in the core and envelope respectively. Density structure through the envelopes of all the stars shown is similar, with sound speed increasing with mass due to a corresponding increase in luminosity/temperature, as seen in Figures 2.1 & 2.2.

2.3 Flow Parameters in the Stellar Envelope

The application of simulation results from De et al. (2020); MacLeod & Ramirez-Ruiz (2015b); MacLeod et al. (2017b) requires that we interpret envelope structure as it relates to CE inspiral using the dimensionless quantities used in those studies. This allows us to characterize a dynamic process that involves many relevant physical quantities and variations with a few key parameters that combine information about the structure of the envelope, properties of the binary, and inspiral mechanics. For additional details beyond the brief introduction given here, the reader is referred to MacLeod & Ramirez-Ruiz (2015a,b) and MacLeod et al. (2017b).

2.3.1 Relevant Scales and Parameters

We model our typical CE system in simplest terms as a binary in which the primary, with mass M_1, is more massive and extended, and the secondary is a compact, lower mass object of mass M_2. We define the global mass ratio of the binary as $q_{\rm B} = M_2/M_1$. The center of the primary is separated from the secondary by a distance a. At any given point after the onset of CE, the primary mass enclosed at separation a is defined as $M_{\rm enc} < M_1$. We define the mass ratio between the secondary and the mass enclosed at separation a as

$$q_{\rm r} = \frac{M_2}{M_{\rm enc}}. \tag{2.1}$$

This quantity will increase as inspiral progresses since $M_{\rm enc}$ decreases with a, though this is most pronounced in the inner envelope. Any accretion onto the secondary will serve to boost this effect.

Following the formalism of MacLeod et al. (2017b), we approximate our inspiral to first order as a modified keplerian orbit, giving the velocity of the secondary relative to the envelope material as

$$v_\infty = f_{\rm k}\sqrt{\frac{G(M_{\rm enc}+M_2)}{a}} \tag{2.2}$$

in which $f_{\rm k}$ reflects the degree to which the rotation of the envelope and the orbit of the secondary are non-synchronous (ie. $f_{\rm k} = 1$ gives a perfectly keplerian orbit with no co-rotation, and $f_{\rm k} = 0$ gives an orbit in which the envelope and secondary are tidally locked).

Moving into dimensionless terms, we use the framework for flows and accretion first introduced by Hoyle & Lyttleton (1939), hereafter HLA (Hoyle & Lyttleton 1939; Bondi & Hoyle 1944). We characterize the relative velocity v_∞ with Mach number

$$\mathcal{M}_\infty = \frac{v_\infty}{c_{\rm s}} \tag{2.3}$$

in which c_s is the local sound speed of the undisturbed envelope material at separation a. Generally, dynamical inspiral spans a range of low Mach numbers, on order of a few. As the secondary moves through the envelope, it will affect oncoming material gravitationally as it passes by; the cross-section of oncoming material that is within this gravitational “sphere of influence” is characterized by the accretion radius

$$R_{\mathrm{a}} = \frac{2GM_2}{v_\infty^2} \tag{2.4}$$

which is a function of not only the secondary's mass, but the changing enclosed mass and separation a. To get a sense of how strong the impact of an envelope density gradient may be on the flow and accretion, we compare R_{a} to the density scale height at the location of the secondary

$$H_\rho = -\rho \frac{dr}{d\rho}, \tag{2.5}$$

which describes the local density normalized by the local density gradient with respect to radius. From this comparison arises the quantity

$$\epsilon_\rho = \frac{R_{\mathrm{a}}}{H_\rho}, \tag{2.6}$$

which is a measure of how many local scale heights are traversed by the local accretion radius (ie. $\epsilon_\rho = 0$ corresponds to a constant density medium and a symmetric HLA-type flow and accretion, while $\epsilon_\rho > 1$ corresponds to density gradients that break the symmetry in the flow and suppress accretion significantly).

2.3.2 Envelope Equation of State

The drag formalism was developed with the assumption of a polytropic envelope, out of which arises a structural polytropic index,

$$\Gamma_{\mathrm{s}} = \left(\frac{d\ln P}{d\ln \rho}\right)_{\mathrm{env}}, \tag{2.7}$$

which is evaluated along the envelope profile, such that $P \propto \rho^{\Gamma_{\mathrm{s}}}$. For MIST/`MESA` stellar profiles, we smooth the numerical derivative with a Gaussian filter with standard deviation of $\sim 1\%$ of the envelope's extent.

However, the envelope material does not always behave as an ideal gas, requiring an equation of state (EOS) with several adiabatic indices to describe its behavior when compressed during the inspiral of the secondary. The indices of interest to us are as follows:

$$\gamma_1 = \left(\frac{d\ln P}{d\ln \rho}\right)_{\mathrm{ad}}, \tag{2.8}$$

which is used to compute the local sound speed, and

$$\gamma_3 - 1 = \left(\frac{d\ln T}{d\ln \rho}\right)_{\mathrm{ad}}, \tag{2.9}$$

which is used to relate pressure, density, and internal energy. These indices are the same in an ideal gas, and are equivalent to Γ_{s} at constant entropy.

In Figure 2.4, we present for comparison these three indices, as well as the familiar structural quantities of sound speed c_s and density ρ, with the corresponding $\mathcal{M}_\infty$ and ϵ_ρ values calculated for MIST models of initial mass 3 and $50 M_\odot$, respectively, with a secondary of mass ratio $q_{\rm B} = 0.1$. Throughout most of the envelope in both cases, $\Gamma_{\rm s} \sim \gamma_1$, with noted exception upon approaching the core. Features are naturally mirrored among all of these quantities, to a greater or lesser extent, yet the monotonic decrease we would expect in $\mathcal{M}_\infty$ and ϵ_ρ from the limb to the core for a polytropic envelope is still represented here. Therefore we cautiously move forward with a simplified approach that may allow us to parameterize dynamical inspiral further.

2.3.3 Polytropic Formalism

When assuming a polytropic stellar profile, the relationships of the flow parameters of Subsections 2.3.1 and 2.3.2 can be constructed in the following manner, as in MacLeod et al. (2017b):

$$\epsilon_\rho = \frac{2q_{\rm r}}{(1+q_{\rm r})^2} \frac{\mathcal{M}_\infty^2}{f_{\rm k}^4} \left(\frac{\gamma_1}{\Gamma_{\rm s}} \right). \tag{2.10}$$

In the simplified case in which the inspiral velocity is approximated to first order as keplerian and the envelope has constant entropy, this expression simplifies to

$$\epsilon_\rho = \frac{2q_{\rm r}}{(1+q_{\rm r})^2} \mathcal{M}_\infty^2. \tag{2.11}$$

This implies that for these special cases, our flow parameters are intrinsically linked, and that two of these quantities may be sufficient to characterize the flow at a given location.

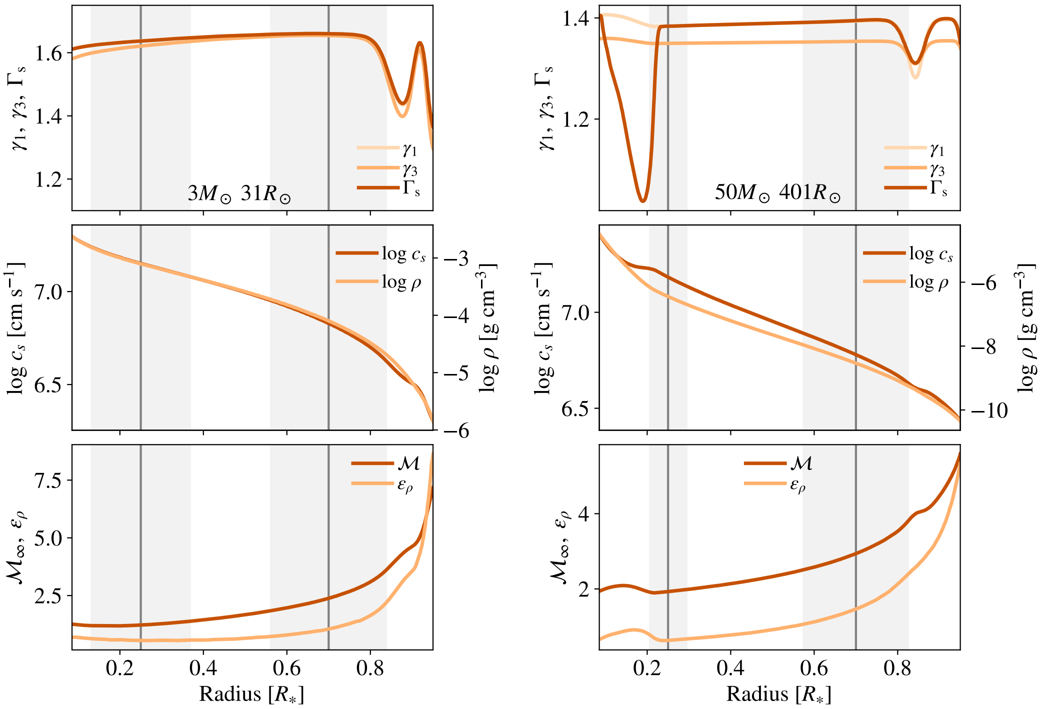

Figure 2.4 A comparison of standard EOS and structural quantities against drag formalism parameters for initial mass $3M_\odot$ and $50M_\odot$ stars at $31R_\odot$ and $401R_\odot$, respectively, with a secondary of mass ratio 0.1. Only the envelope is shown. For the secondary located at a given dark grey line, shaded regions show the span of R_a to the left and right of that location. Note that R_a has a location dependence. The extent of this region illustrates the envelope material that is gravitationally influenced by the secondary during inspiral. *Left panels:* The envelope in this case is largely convective, the majority having $\Gamma_\mathrm{s} \sim 5/3$ with some higher compressibility regions in the outer part. In convective envelopes, we expect $\Gamma_\mathrm{s} \sim \gamma_1 \sim \gamma_3$ due to constant entropy. *Right panels:* The envelope is largely radiative, giving different values for γ_1 and γ_3: $\Gamma_\mathrm{s} \sim \gamma_1 \sim 1.4$ until approaching the core, but γ_3 maintains a slightly lower value $\sim 4/3$.

2.3.4 Key Results of Hydrodynamic Simulations

Using a traditional HLA framework, the drag force on the secondary is expected to be

$$F_{\mathrm{d,HLA}} = \pi R_{\mathrm{a}}^2 \rho_\infty v_\infty^2 \tag{2.12}$$

and the corresponding accretion rate on to the secondary

$$\dot{M}_{\mathrm{HLA}} = \pi R_{\mathrm{a}}^2 \rho_\infty v_\infty, \tag{2.13}$$

in which ρ_∞ is the density of undisturbed oncoming wind. However, these expressions assume ρ_∞ to be constant, and are unlikely to match that measured when a wind with a density gradient is used and symmetry in the wake is broken. A key result from the suite of simulations performed by MacLeod & Ramirez-Ruiz (2015b); MacLeod et al. (2017b); De et al. (2020) is a grid of drag force measurements

$$F_{\mathrm{d}} = C_{\mathrm{d}} F_{\mathrm{d,HLA}} \tag{2.14}$$

and accretion rates

$$\dot{M} = C_{\mathrm{a}} \dot{M}_{\mathrm{HLA}} \tag{2.15}$$

in which C_{d} and C_{a} are drag and accretion coefficients, respectively, that characterize the steady-state time-averaged drag force and accretion rate from a specific simulation setup normalized by the calculated HLA values based on the undisturbed envelope density ρ at the location of the secondary. As each simulation setup reflects a single value for each of $\mathcal{M}_\infty$, q_{r}, ϵ_ρ, and γ (for setups in which $\gamma = \Gamma_{\rm s} = \gamma_1 = \gamma_3$), each pair of $C_{\rm d}$ and $C_{\rm a}$ then maps to a specific combination of these four quantities, all of which may be calculated or approximated with a basic stellar model and global properties of the pre-CE system.

These coefficients form the basis for broad application of the drag formalism to any type of CE event that may be of interest, using the above quantities to map coefficient values via interpolation or fitting functions. Examples include integration of the equation of motion of dynamical inspiral using a static stellar model (e.g. Figures 11, 12 of MacLeod et al. 2017b), introduction of a heating term in 1D hydrodynamic simulations of CE (Fragos et al. 2019) through the relation $\dot{E} \approx F_{\rm d} v_\infty$ (MacLeod & Ramirez-Ruiz 2015b), and calculation of drag force for comparison against that produced by global 3D hydrodynamic simulations (Chamandy et al. 2019b). Notably, Chamandy et al. (2019b) found that during dynamical inspiral, when the assumptions of the drag formalism are met, the drag force calculated with the coefficients is in excellent agreement with that measured in a global simulation. This encouraging result shows the drag formalism to be an effective prescription for dynamical inspiral, and motivates its further development.

2.4 Mapping of Dynamical Inspiral in Simulation Parameter Space

Any binary system that results in a merger or close binary via the traditional formation channel must go through at least one CE phase. The flow parameters discussed in Section 2.3 allow us to analyze CE inspiral not in terms of familiar quantities (ie. ρ, $v_{\rm orb}$, etc.) that keep structural and dynamical information separate, but in terms of dimensionless quantities (ie. ϵ_ρ, $\mathcal{M}_\infty$, $q_{\rm r}$) that combine properties of the system with local structure and dynamics. Translated into the latter, a given system's inspiral corresponds to a curve in parameter space that traces the evolution of the three flow parameters from the outer regions of the envelope to a transitional region near the core boundary. Each point in this parameter space corresponds to a unique drag coefficient $C_{\rm d}$ and accretion coefficient $C_{\rm a}$ (see Subsection 2.3.4) that, when included in inspiral calculations, alters the orbital decay expected from the HLA formalism. By understanding the curves through this parameter space for a range of different progenitor systems, we can apply these drag coefficients to any stellar envelope based on the properties derived directly from stellar models.

2.4.1 Methodology

In utilizing the results of the numerical simulations from MacLeod & Ramirez-Ruiz (2015b), MacLeod et al. (2017b), and De et al. (2020), we assume progenitor systems that span a wide range of mass, age, internal structure, and separation that include one giant branch star (hereafter, the primary) and one compact star (hereafter, the secondary) with q_{B} ranging from $0.1 - 0.35$. To ensure that the envelope material encountered is structured consistently with the simulations, we limit the range of mass ratio such that throughout dynamical inspiral the accretion radius of the secondary does not exceed the remaining separation. We generate a library of stellar models spanning the aforementioned axes using the `MESA` Isochrones and Stellar Tracks (MIST) (Dotter 2016; Choi et al. 2016) package with `MESA` v7503 (Paxton et al. 2011, 2013, 2015). We have chosen MIST models for analysis due to the observational calibrations of the framework, though there are limitations to its use at very high mass and low metallicity (see Subsection 2.5.4, in which we address results from alternative libraries).

To get an agnostic view of flow parameters across a range of binary systems, we evolve stars of solar metallicity from $1 - 90 M_{\odot}$ through the giant branch, including profiles in our analysis based on the criterion of increasing radius in log space (a proxy for binary separation at onset) up to the maximum radius (R_{max}) produced by the code. Due to mass dependent differences in late stage evolution as well as winds/mass loss, the maximum radius of each primary is unique; for any system, the maximum possible separation for which a CE phase will occur is defined to first order by this value.

CE inspiral takes place only in the stellar envelope, therefore we limit our analysis to that region. Dynamical inspiral occurs after CE onset, which disrupts the outer layers of the envelope (MacLeod et al. 2017a). Due to the "wind tunnel" morphology that the drag formalism is based upon, in particular the presence and undisturbed structure of oncoming material, it is appropriate for use only after the secondary is embedded. Thus we begin our analysis at a very conservative limit of $a = 0.95R_*$ for each model as an ersatz starting point for the dynamical plunge of the secondary, which is considered to be embedded and desynchronized post-onset (see Subsection 2.5.1), and stop our analysis outside the core (see Subsection 2.5.2). Due to the uncertainties regarding the conditions for successful envelope ejection, we make no claims about the termination of our calculated inspirals in connection with the outcome of a given CE event. Rather, we choose to map the entire range in which the drag formalism might be applied, and discern general trends as well as the region of parameter space in which the formalism breaks down.

Combining the global properties and structural quantities from our realistic stellar models with a range of $q_{\rm B}$ values with constant (non-accreting) M_2, we then calculate the drag formalism parameters to produce characteristic curves for each inspiral in the parameter space.

2.4.2 Characteristic Curves of Dynamical Inspiral

The shape of the characteristic curve for a given dynamical inspiral in the $\mathcal{M}_\infty - \epsilon_\rho$ parameter space is influenced by the structure of the envelope of the primary. In Figure 2.5, we show selected curves for events with mass ratio $q_{\rm B} = 0.2$ from various stages in the time evolution of initial mass $10M_\odot$

and $80M_\odot$ giants for comparison. These correspond to a range of binary separations: each panel represents a CE inspiral initiating at a separation equal to the model's extent, noted at the top of each panel. The color of the curve reflects the region in the extended primary where each set of combined $(\mathcal{M}_\infty, \epsilon_\rho)$ conditions exist in radial coordinates, with inspiral proceeding from the upper right to lower left corner of the parameter space.

In general, inspiral is characterized by the highest values and broadest ranges of $\mathcal{M}_\infty$ and ϵ_ρ in the outer envelope, with lower values in the inner half of the envelope by radius. Though each curve is distinct, features which are present due to fluctuations in the envelope EOS (see Subsection 2.5.3) are minor.

The effect of mass ratio on inspiral characteristic curves is shown in Figure 2.6. Using an example primary of $6M_\odot$ evolved to $250R_\odot$, we calculate curves for mass ratios $q_\mathrm{B} = 0.05$, 0.1, 0.2, and 0.3, which might represent, for example, a white dwarf, neutron star, or companion main sequence star secondary. There is a clear inverse relation between the slope of the curve and q_B value. According to the drag formalism, each point on a curve corresponds to a C_d and C_a value; however, these coefficients depend on the local mass ratio q_r to be correctly applied. Figure 2.6 demonstrates that q_r remains nearly constant for the duration of dynamical inspiral, increasing appreciably only when the secondary reaches the innermost regions of the envelope. Thus we may justify a simplified application using something like an average mass ratio as by De et al. (2020), especially when energy considerations indicate an outcome of

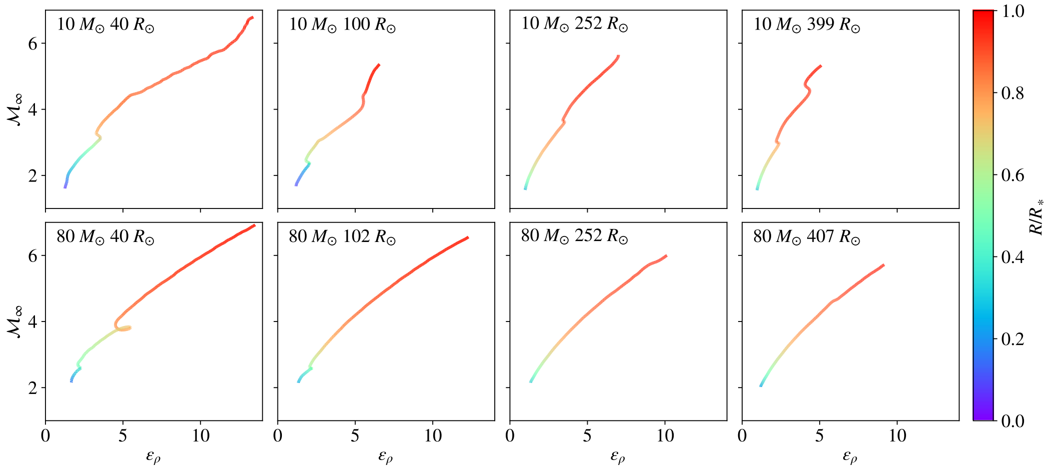

Figure 2.5 Representative examples of characteristic curves for CE events with $q_\mathrm{B} = 0.2$ in the $\mathcal{M}_\infty - \epsilon_\rho$ parameter space. In panels from left to right, stellar models increase in age and extent, with models of initial mass $10M_\odot$ and $80M_\odot$ represented on the top and bottom rows respectively. The upper right portion of each curve represents conditions in the outer envelope and the lower left portion of each curve represents conditions in the inner envelope, with normalized radius mapped in color. Each point on a curve corresponds to unique drag and accretion coefficients, making each characteristic curve a mapping of the dynamics occurring during a dynamical inspiral phase consistent with the setup, ie. primary and secondary masses, separation at onset, etc. This curve can be calculated for any appropriate binary with a sufficiently detailed stellar model for the primary.

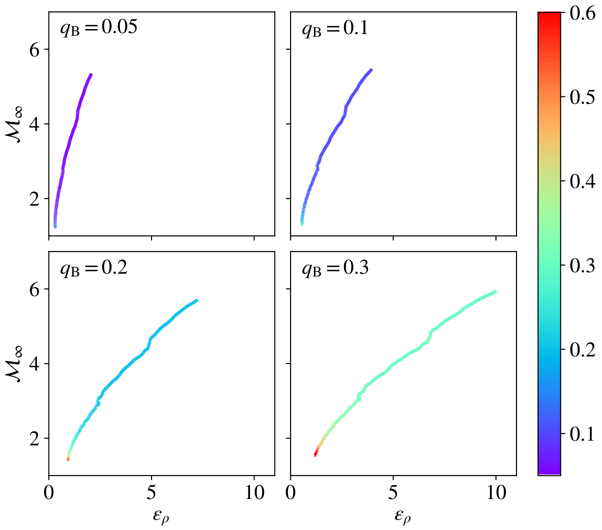

Figure 2.6 Additional examples of characteristic curves for CE events in the $\mathcal{M}_\infty - \epsilon_\rho$ parameter space involving a primary of $6M_\odot$ at $250R_\odot$ and a selection of q_B values. Curve color corresponds to the local value of q_r. Due to the diffuse nature of envelope material, q_r is nearly constant until the secondary approaches the core. The slope of the curve decreases with increasing q_B, reaching slightly higher $\mathcal{M}_\infty$ values and notably higher ϵ_ρ values for the same primary. This is due to the effect of the increase in M_2 on orbital velocity v_∞ and the accretion radius R_a, respectively.

successful envelope ejection, therefore avoiding the material near the core.

2.4.3 Self-Similarity Across Axes

In Figure 2.7, we produce characteristic curves for inspirals with a range of q_B appropriate for the drag formalism across the axis of mass. The primary profiles used are giant stars of initial mass 6, 10, 50, and $80M_\odot$ extended to $250R_\odot$. These curves are representative across the entire library of stellar profiles, and repeat the trends seen in Figures 2.5 and 2.6. The decrease in slope corresponding to the increase in mass ratio combined with the similarity of these curves repeats this familiar fan shape throughout, and lends itself to further simplification.

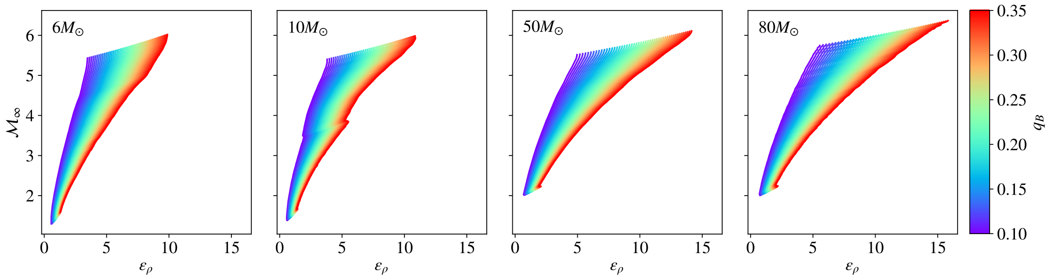

Figure 2.7 Characteristic curves of dynamical inspiral for primaries of initial mass 6, 10, 50, and $80M_\odot$ and binary separation/radial extent of $250R_\odot$. An appropriate range of q_B values for application of the drag formalism are plotted by color. Curves are shown to be self-similar in the $\mathcal{M}_\infty - \epsilon_\rho$ parameter space.

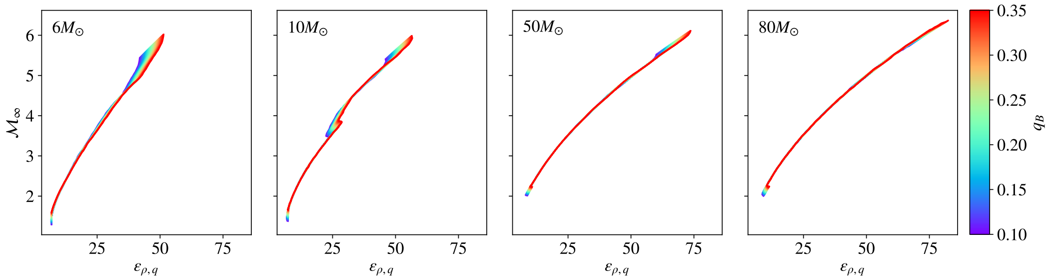

Figure 2.8 Shown are the same characteristic curves from Figure 2.7 normalized for the mass ratio term in Equations 10 and 11. In the “collapsed” $\mathcal{M}_\infty - \epsilon_{\rho,q}$ parameter space, dynamical inspirals for a given primary and separation are characterized by a single, nearly quadratic curve.

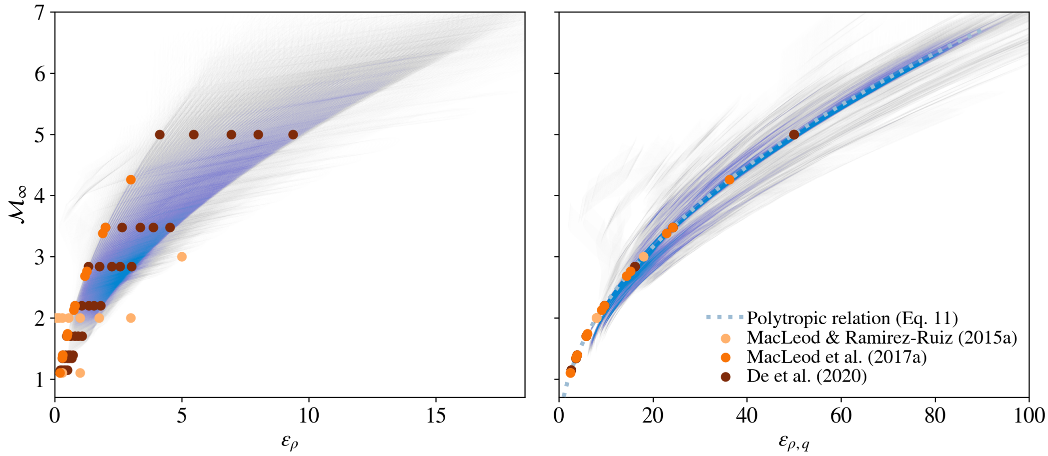

Figure 2.9 In the left panel are shown the overlaid characteristic curves for dynamical inspirals in the $\mathcal{M}_\infty - \epsilon_\rho$ parameter space for primaries of initial mass 1, 3, 6, 10, 16, 20, 30, 40, 50, 60, 70, 80, and 90 $M_\odot$ from the end of core H-burning, through each profile of increasing radius up to the maximum reached, for a range of q_B from 0.1-0.35. Transparent, grey regions in this parameter space have values less commonly encountered, while opaque, blue regions cover values that are extremely common. Overplotted are points in the parameter space for which local envelope drag and accretion coefficients have been calculated from "wind tunnel" simulations by MacLeod & Ramirez-Ruiz (2015b); MacLeod et al. (2017b); De et al. (2020). In the right panel are shown the same curves normalized over the mass ratio term, defined as $\epsilon_{\rho,q}$ in Equation 16. Consistency with the simplified polytropic relation of Equation 11, based on MacLeod et al. (2017b), suggests an effective functional form requiring only a few envelope parameters may be possible to characterize the dynamical inspiral phase.

Using Equations 10 and 11 as our guide, we normalize these curves over the $q_{\rm r}$ term in Figure 2.8 using the following definition:

$$\epsilon_{\rho,q} = \epsilon_{\rho} \frac{(1+q_{\rm r})^2}{q_{\rm r}}. \tag{2.16}$$

Upon normalization, the fans collapse into a simple, approximately quadratic curve. Again, these curves are representative of the same calculations across the entire library of stellar profiles. The truncation of these curves in the outer envelope lie near $\mathcal{M}_{\infty} \sim 6$, and in the inner envelope are a function of how distinct the transition is from envelope to core, ranging from $\mathcal{M}_{\infty} \sim 1 - 2$.

In Figure 2.9, we repeat the above calculations for all post-main sequence stellar profiles from 1-90 $M_{\odot}$. The left panel reveals the region of the $\mathcal{M}_{\infty} - \epsilon_{\rho}$ parameter space that is represented in realistic stellar profiles and therefore ideal for simulation in order to support inspiral calculations more broadly. Though initial simulations by MacLeod & Ramirez-Ruiz (2015b) and MacLeod et al. (2017b) cover the low mass ratio regime of this region, the full relevant parameter space is well-covered by the simulations in a companion paper, De et al. (2020). Furthermore, in the right panel, the region in "collapsed" parameter space that is most densely covered reveals the most basic characteristic curve for dynamical inspiral, and fits the polytropic relation of Equation 2.11, which in such a broad range of non-polytropic envelopes reveals they are nonetheless polytropic "enough" for the drag formalism to be a good approximation of the conditions, and that there are fairly distinct truncation points to the overlay that we may take advantage of, to first order, in a prescriptive capacity.

Through a systematic comparison and analysis of characteristic curves across multiple axes, we find that nearly all dynamical inspirals that meet the basic criteria for application of the drag formalism (ie. $q_{\rm B} \lesssim 1/3$) are self-similar in $\mathcal{M}_\infty - \epsilon_\rho$ space. This self-similarity holds across the axes of primary mass M_1, the initial binary separation a (or likewise the post-main sequence age/radius of the primary), and binary mass ratio $q_{\rm B}$ (for a discussion of the same across metallicity, see Subsection 2.5.4).

2.5 Range of Applicability: Limitations and Exceptions

2.5.1 Onset and Initial Mass Loss

The dynamics of CE onset is an area of active study (see, e.g. Iaconi et al. 2017; MacLeod et al. 2018a; Reichardt et al. 2019; Shiber et al. 2019; MacLeod & Loeb 2020a,b) which is not yet well understood and has not yet been incorporated into the drag formalism. CE events occur after some initial destabilization of the binary: for some systems, this is a result of the Darwin tidal instability, and for others a result of unstable Roche lobe overflow (MacLeod et al. 2017a). The dependence on both mass ratio and primary stellar structure requires that both types of systems are represented in the range of binaries used in this work. The setup of the "wind tunnel" simulations assumes a plunge into undisturbed stellar envelope, and the envelope depth at which we may assume this criterion to be satisfied post-onset is variable and dependent on many factors which have not been accounted for in a general formalism.

Therefore, we choose to map the broadest range of envelope parameters, which assumes little or no mass loss prior to CE as in the case of Darwin instability, rather than removing large portions of envelope based on incomplete understanding. Incorporation of mass loss during onset, assuming no changes to the structure of the remaining envelope material, will bring the upper right truncation point of a given dynamical inspiral into a lower range of $\mathcal{M}_\infty$ and ϵ_ρ values, reducing the coverage of parameter space traced by that inspiral.

Depending on the duration of the pre-CE phase, the bound envelope material may adjust its structure relative to the static models used in this study. The application of this framework to such adjusted models would not have an impact on the drag and accretion coefficients as they correlate to the parameter space, but would simply change the extent and region of parameter space crossed during a particular dynamical inspiral relative to a static model. Due to the representation of a broad range of envelope configurations and their consistent tracing of the same parameter space, it is unlikely that these changes would push a characteristic curve outside of the region represented here. Further work is needed to explore the junction of onset mechanics and the drag formalism for self-consistent application.

2.5.2 The Dynamical Boundary

The appropriate definition of the core boundary for purposes of CE calculations is difficult to pinpoint for stars in different mass regimes and various stages of post-main sequence evolution. In attempting to account for the varying criteria used in the literature to define that boundary (Tauris & Dewi 2001; Ivanova et al. 2013), we applied different definitions to characteristic curve calculations across the full model library and found that the drag formalism presents its own unique termination point - the dynamical boundary.

In Figure 2.10, we use a $6M_{\odot}$ primary extended to ~ 100, 200, and $500R_{\odot}$ to plot raw characteristic curve calculations (upper left), ^{1}H mass fraction (upper right), nuclear energy generation (lower left), and entropy (lower right). In the upper left panel, the steeper curves represent the dynamical inspiral phase with calculations beginning at the blue diamonds. These descend from the top right to bottom left, then have a sharp inflection point at or near the minimum Mach value: this is the dynamical boundary, marked by dark brown dots. The tails that then pass from left to right fall outside the applicable range of the drag formalism. The sharp increase in ϵ_{ρ} mirrors the steep density gradient which occurs at the core boundary, but doesn't coincide with the location at which the traditional $X_{^{1}\mathrm{H}} = 0.1$ criterion is met, marked by blue dots. In all panels, it can be seen that the dynamical boundary precedes the structural core boundary in all cases - this is due to the R_{a} dependence in calculating ϵ_{ρ}, which incorporates the core boundary into the characteristic curve "before" the secondary arrives at the core.

For CE events, it is often more desirable to identify the so-called bifurcation point: the location that marks the extent of the remaining material, which may include the core and some envelope remnants, if CE ejection is successful. Estimates for this location are readily calculated using the well-known energy formalism (van den Heuvel 1976; Webbink 1984; Livio & Soker 1988; de Kool 1990; Iben & Livio 1993):

$$E_{\mathrm{bind}}(r) = \alpha \Delta E_{\mathrm{orb}}, \tag{2.17}$$

in which $E_{\mathrm{bind}}(r)$ is the gravitational binding energy of the envelope at r, ΔE_{orb} is the change in orbital energy of the secondary from the separation at onset to r, and α is an efficiency term of order unity. For cases in which $\alpha = 1$, all orbital energy that is lost through inspiral is used to eject the envelope (assuming no additions or losses from other physical processes), and the location r at which they are equated (marked in Figure 2.10 by crosses), meaning there has been enough energy deposited to eject the envelope from that point outward, is a loose proxy for the bifurcation point.

The dynamical boundary is not the bifurcation point. Rather, because the drag formalism applies strictly to dynamical inspiral, the dynamical boundary represents the innermost location at which a dynamical inspiral is possible, not accounting for the timescales of energy transport. Comparisons by Chamandy et al. (2019b) show a break in agreement between the drag force as calculated using the drag formalism and that measured in a 3D global hydrodynamic simulation; this break occurs not so much due to changes in local mass ratio, as they suggest, but because the dynamical boundary has been reached and the secondary is entering a self-regulating inspiral, in which the drag formalism is not applicable.

In general, a secondary that has reached the dynamical boundary has the following possible outcomes: the secondary is plunging in and will merge with the core of the primary, or the secondary is transitioning to a self-regulated inspiral and, if energy considerations permit ejection of the envelope, binarity will be preserved. As such, it is consistent that the dynamical boundary should lie some small distance outside the core and bifurcation point, as in Figure 2.10 the dynamical boundary for each model lies external to the location at which the $\alpha = 1$ ejection criterion is satisfied. This allows us to apply the drag formalism to the full extent of the envelope as long as the conditions for dynamical inspiral are met. Future work will explore the relationship of the dynamical boundary with the initiation of self-regulated inspiral.

2.5.3 Effects and Consequences of EOS

Though the majority of characteristic curves in this work show few or no features, there are exceptions. In a polytropic envelope, any characteristic curve would be featureless and follow the shape seen in the right panel of Figure 2.9. Because we use realistic stellar models in which the envelope does not always behave as an ideal gas, the values of Γ_s, γ_1, and γ_3 may diverge, creating notable features on the curve.

In Figure 2.11, we compare the γ_3 values in the envelope against characteristic curves for inspirals of $q_{\rm B} = 0.2$ in stars of initial mass 1, 3, 16, and $50 M_\odot$ from the end of H-burning (purple) to the maximum radius achieved during the giant branch (red). Demonstrating our baseline, envelopes with $\gamma_3 \sim 5/3$ (purple and dark blue in the four left panels) or 4/3 (most curves in the rightmost panels) align with the expected featureless morphology of a polytropic curve (Murguia-Berthier et al. 2017).

In several characteristic curves in the lower panels, loops can be seen, which represent regions in which $\Gamma_{\rm s}$ diverges from γ_1. When such curves are collapsed over the q term as seen above, these loops also collapse. Such variations, as they pertain to drag and accretion coefficients, may be well represented by an averaged featureless curve.

In other profiles, some of the features visible are bands of convective and radiative regions within the same envelope, as well as spikes near the limb that represent density inversions in the outermost envelope. The bands generally do not appear in the characteristic curves, but the density inversions, which are a result of steep temperature gradients in zones of partial ionization (Harpaz 1984) that correspond to hydrogen and helium opacity "bumps" (Sanyal et al. 2015; Guzik et al. 2018), fall outside simulated parameters and force ϵ_ρ values to be negative; thus models that have such density inversions are not appropriate for the drag formalism. It is worth noting that, due to mass loss during onset, the regions containing this feature may possibly be stripped from the star prior to CE, and envelope regions internal to this feature fit comfortably within the established parameter space. However, also worth noting is that there is evidence such density inversions may be a result of 1D simulation that are short-lived (when they appear at all) in 3D simulation and may be non-physical (Jiang et al. 2015). As prescriptions in 1D improve, we may expect an even broader range of models for which the drag formalism is applicable.

In Figure 2.12, we map the ratio $\gamma_1/\Gamma_\mathrm{s}$ for all post-main sequence stellar profiles in our library using overlaid $\mathcal{M}_\infty - \epsilon_\rho$ tracks calculated with $q_\mathrm{B} = 0.1$ (left panel) and overlaid $\mathcal{M}_\infty - \epsilon_{\rho,q}$ tracks calculated for $q_\mathrm{B} = 0.1 - 0.35$ (right panel). Increased color saturation indicates increased incidence of the corresponding $\gamma_1/\Gamma_\mathrm{s}$ value in the tracks. The left panels shows that even with realistic stellar envelopes, for any given mass ratio the slope dependence of Equation 10 on $\gamma_1/\Gamma_\mathrm{s}$ holds, with higher values to the right and lower values to the left, and that ratios around 1 are most common. In the right panel, we validate this for all q_B values. This is encouraging, and suggests that a prescriptive parameterization of dynamical inspiral may make use of Equation 11 for simplicity, while covering the most relevant part of parameter space for most cases.

2.5.4 Alternative Models: Effects of Metallicity

In CE events, an analysis of stellar profiles across the axis of metallicity is of interest due to the impact of metallicity on winds, mass loss, and maximum radial extent during late stage stellar evolution. These issues are pronounced in the cases of LIGO binary black hole progenitors due to the need to form

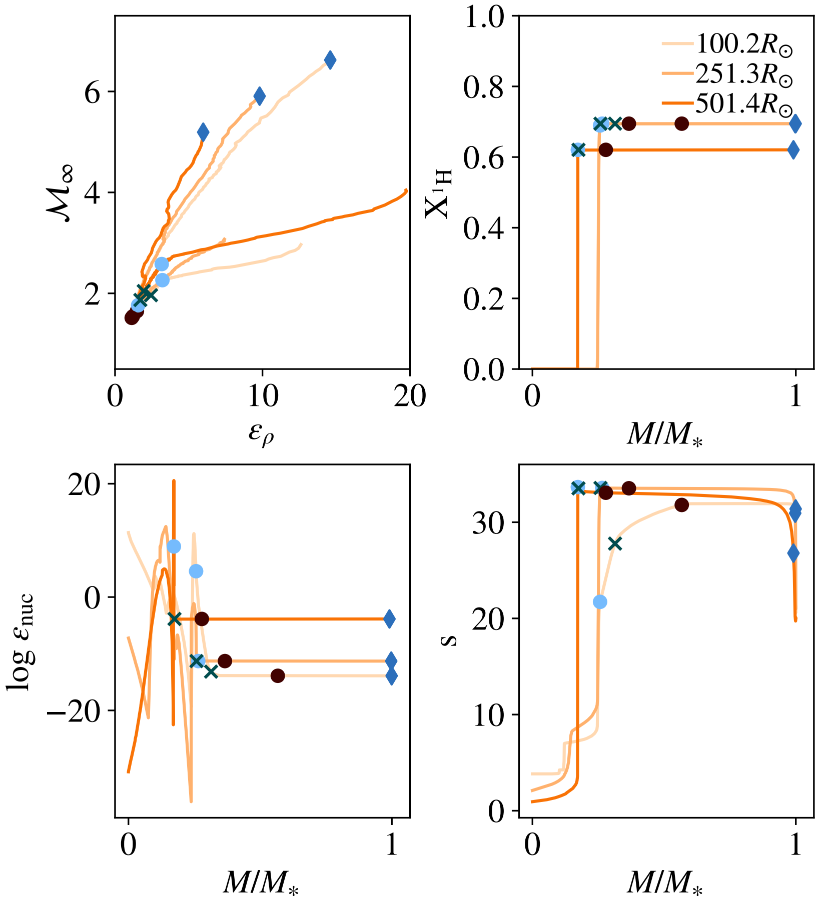

Figure 2.10 Quantities shown are drawn from stellar models of initial mass $6M_\odot$ at extents of $100.2R_\odot$, $251.3R_\odot$, and $501.4R_\odot$. For each stellar profile, blue diamonds mark the beginning of inspiral calculations near the limb, blue dots mark the location of $X_{^1\mathrm{H}} = 0.1$, brown dark dots mark the location of the dynamical boundary, and crosses mark the location at which the $\alpha = 1$ criterion for envelope ejection is satisfied. *Upper left:* Raw calculations of characteristic curves for dynamical inspiral in $\mathcal{M}_\infty - \epsilon_\rho$ parameter space with $q_\mathrm{B} = 0.3$. Lines descending from the blue diamonds represent dynamical inspiral through envelope material, while shallow tails crossing left to right beyond the inflection point are the same calculations across and beyond the core boundary. Remaining panels reflect various structural quantities used in the literature to discern the core boundary. *Upper right:* Hydrogen mass fraction versus mass. Note that the curve for the $100.2R_\odot$ profile lies beneath that of the $251.3R_\odot$. *Lower left:* Nuclear energy generation versus mass. *Lower right:* Entropy versus mass.

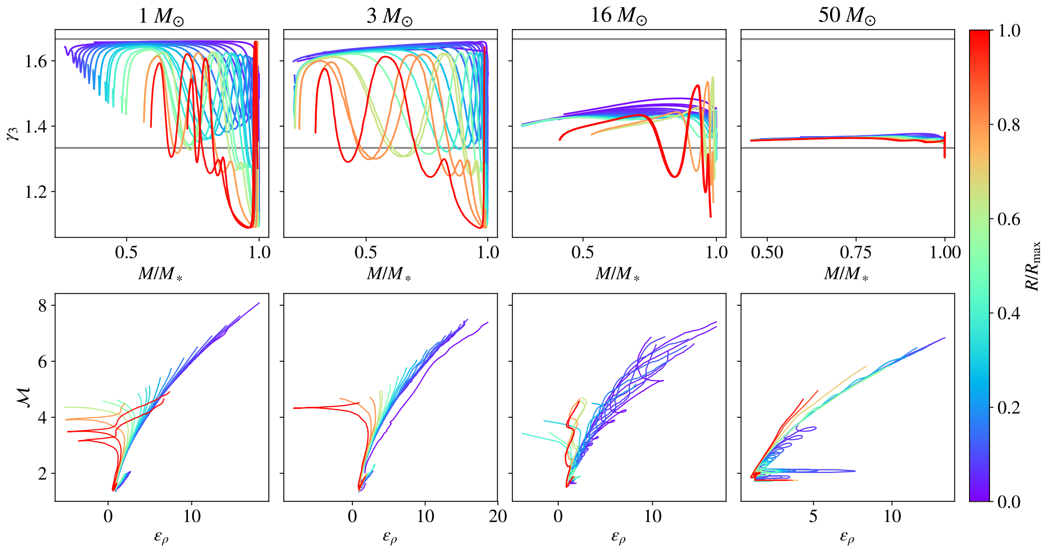

Figure 2.11 A comparison of γ_3 values in the envelope and characteristic curves for inspiral with mass ratio 0.2 for stars of initial mass 1, 3, 16, and $50 M_\odot$. Each star is followed from the end of Hydrogen burning to its maximum extent on the giant branch, $R_{\max}$. Color represents the radius of each stellar profile as a fraction of $R_{\max}$, with the envelope expanding from purple to red through time. *Upper panels:* Horizontal gray lines are placed at $\gamma_3 = 5/3$ and $4/3$ for reference. In the lower mass stars, envelopes are seen to evolve from purely convective to bands of convective and radiative regions, with highly compressible regions of partially ionized material in the outer portions of the star near $R_{\max}$. Large spikes in the outermost regions are density inversions. *Lower panels:* Characteristic curves in $\mathcal{M}_\infty - \epsilon_\rho$ parameter space, matched by color to corresponding EOS curves above. Banded regions do not impact the curves, but density inversions near the limb appear as negative ϵ_ρ values, precluding these regions from application of the drag formalism. Loops occur in regions where Γ_s diverges from γ_1.

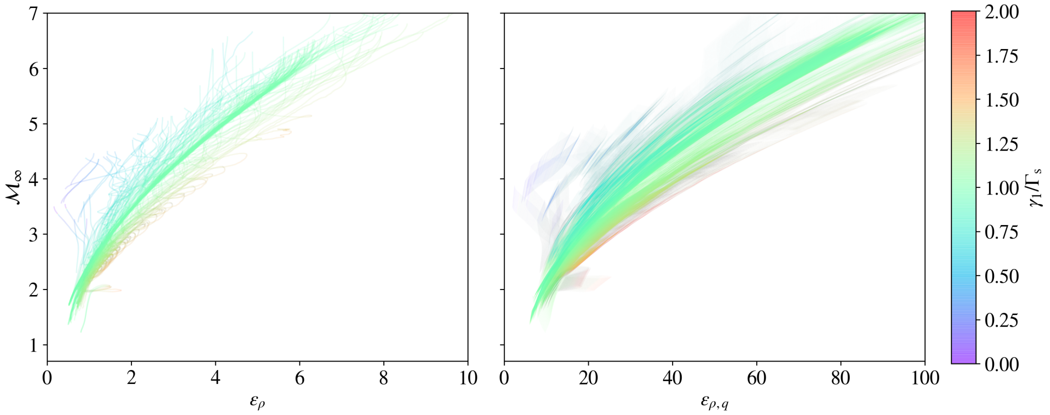

Figure 2.12 Overlaid values of $\gamma_1/\Gamma_\mathrm{s}$ for all post-main sequence stellar profiles for masses $1-90M_\odot$, mapped onto $\mathcal{M}_\infty-\epsilon_\rho$ curves for inspirals with $q_\mathrm{B}=0.1$ (left panel) and collapsed $\mathcal{M}_\infty-\epsilon_{\rho,q}$ curves for $q_\mathrm{B}=0.1-0.35$ (right panel). Intensity of color denotes frequency of incidence of the corresponding ratio. The slope dependence of Equation 10 on $\gamma_1/\Gamma_\mathrm{s}$ is clearly shown, supporting its use even with realistic stellar profiles. In addition, most characteristic curves throughout the giant branch have $\gamma_1/\Gamma_\mathrm{s}$ at or near 1, suggesting that a simplified expression like that of Equation 11 may be useful for a general prescriptive framework.

massive stellar mass black holes while bringing their giant progenitors into very close proximity. Limitations in the MIST models prevent analysis of stellar envelopes of stars that are very high mass and low metallicity.

To address this in part, we generated models using `MESA` v10398 (Paxton et al. 2011, 2013, 2015, 2018) from $16-90M_\odot$ with $1/50Z_\odot$ to apply the same analysis. The self-similarity seen in Section 2.4 holds across this axis of metallicity in high mass giant stars, tracing the same parameter space covered by the MIST models. Due to the uncertainties of stellar models at these masses and metallicities, they did not form the basis of this work, but nonetheless present an encouraging possible application in attempting to model the formation of LIGO-type systems.

2.6 Discussion and Conclusions

The overall self-similarity shown here in the characteristic curves of dynamical inspiral, and the relatively few limitations and exceptions to that self-similarity, suggest that there may be broad prescriptive applications of these results. One key area where a detailed, prescriptive treatment of common envelope may be useful is in population synthesis studies, which currently depend on variations of the energy formalism to discern the success or failure of envelope ejection.

Despite its many variations, the energy formalism fails to account for the dynamics of CE in a satisfactory way. CE events generally include several distinct stages:

- Onset, which occurs after an initial destabilization of the binary and likely results in some mass loss and desynchronization of the secondary and the envelope;
- Dynamical inspiral, in which the secondary plunges quickly, deep into the envelope;

after which a system will merge unless energy conditions for envelope ejection are met, in which case we include:

- Self-regulated inspiral, in which the secondary slowly loses orbital energy on a timescale similar to that of the remaining envelope's thermal timescale;

- Envelope ejection, in which the outer envelope escapes and the remaining envelope contracts, preserving binarity at some final separation.

The outcome of a CE event may be impacted by these stages, beyond what may be accounted for by energy considerations alone. The energy formalism cannot address how the envelope is unbound (see, e.g. Soker 1992, 2017; Clayton et al. 2017; Glanz & Perets 2018), as it does not address energy transport unless it is assumed to be instantaneous. In addition, the current energy formalism assumes a change in orbital energy based on the energetics of circular orbits, while the recent work of Wu et al. (2020) suggests that the energetics of a steep spiral plunge may differ significantly.

This work, when combined with the corresponding drag and accretion coefficients from MacLeod & Ramirez-Ruiz (2015b); MacLeod et al. (2017b); De et al. (2020), provides the basis for a framework for calculating inspiral trajectories with only basic information about a given binary: the masses of the objects, their separation at CE onset, and the core mass of the primary. This can provide timescales for the duration of dynamical inspiral for a variety of CE events, especially as the dynamical boundary provides a natural end point to dynamical inspiral, but cannot speak to onset or final outcome. To improve such trajectories and make predictions about post-CE outcome, complementary frameworks for mass loss during onset and evolution of self-regulated inspiral are needed, as well as adjustments to the energy formalism that take into account the rate of energy transport within the envelope, such as that done by Wilson & Nordhaus (2019) for the low mass regime, and the energetics of non-circular inspiral. Future work will discern if these additions may also be applied in general, without the need for stellar profiles.

The main conclusions of this work are the following:

1. Properties of dynamical inspiral through a broad range of realistic giant branch stellar envelopes are well-described by the dimensionless parameters of the drag formalism (left panel of Figure 2.9 and Section 2.4). This allows for the broad application of corresponding drag and accretion coefficients to calculate quantities of interest for dynamical inspirals using basic stellar profiles, rather than requiring hydrodynamic simulations (Subsection 2.3.4).

2. Characteristic curves of dynamical inspiral in the $\mathcal{M}_\infty - \epsilon_\rho$ parameter space are self-similar across the axes of primary mass, separation (age/radius of primary), and binary mass ratio (Figures 2.7, 2.8, and 2.9). Additional work suggests the same holds across metallicity as well (Subsection 2.5.4). This presents the possibility of a general prescriptive framework that may be applied without the use of a stellar profile, with the addition of treatments for onset, self-regulated inspiral, and energy deposition.

3. The drag formalism presents a natural termination point for dynamical inspiral: the dynamical boundary, which may be intrinsic to the end of CE via the transition to self-regulated inspiral (Subsection 2.5.2). Further work will clarify this relationship.

2.7 Software Utilized

`MESA` (Paxton et al. 2011, 2013, 2015, 2018), `matplotlib` (Hunter 2007), `NumPy` (van der Walt et al. 2011), `py_mesa_reader` (Wolf & Schwab 2017).

Chapter 3

A Framework for Incorporating the Impact of Characteristic Timescales on Common Envelope Ejection

3.1 Introduction

In order to explain the formation of a broad range of close binary systems, as well as exotic transients and their progenitor systems, common envelope (CE) interactions are often invoked. A canonical CE event occurs when one star in a binary system (hereafter, the primary) expands enough to engulf its partner (the secondary), leading to the tightening of the binary's orbit (Paczynski 1976). In simplest terms, a CE episode can lead to the expulsion of the primary's stellar envelope, preserving the binary at a much smaller separation (e.g., Law-Smith et al. 2020a), or it can lead to a merger (e.g., Wu et al. 2020; Hutchinson-Smith et al. 2023), though it is possible for a binary to undergo multiple CE interactions during its lifetime along with episodes of mass transfer and other changes due to stellar evolution (Kaplan et al. 2012; Vigna-Gómez et al. 2020). As such, CE evolution is a critical part of binary (and multiple) star system evolution, without which the formation of some of the most exotic configurations in the universe, such as the progenitors of gravitational wave sources (see, e.g., Belczynski et al. 2002), unique products of interacting triples (e.g., Wu et al. 2020; Rosselli-Calderon et al. 2024), and Thorne-Żytkow objects (Everson et al. 2023; Hutchinson-Smith et al. 2023), could not be understood.

CE evolution is a deeply complex problem which involves physical processes across a vast range of length- and timescales, creating enormous computational and numerical challenges that must be overcome in order to study these episodes in detail (Röpke & De Marco 2023). Nevertheless, it is the details of how a CE event proceeds that determine the outcome of the event (Iben & Livio 1993; Taam & Sandquist 2000; Taam & Ricker 2010; Ivanova et al. 2013; Postnov & Yungelson 2014), and extensive efforts have been undertaken to attempt to map pre-CE systems to their post-CE products (e.g., Davis et al. 2010; Kruckow et al. 2016; Vigna-Gómez et al. 2020; Marchant et al. 2021). Due to the difficulty and expense of modeling CE with state-of-the-art, three-dimensional (3D) numerical tools, nearly all studies that focus on populations of pre- and post-CE systems use one-dimensional (1D) hydrodynamics or binary population synthesis, sometimes in combination (Gallegos-Garcia et al. 2021). However, CE evolution is an inherently 3D problem, in which asymmetry, rotation, and energy and angular momentum transport play a role that can only be approximated by these methods.

The standard treatment for CE events in binary population synthesis is a decades-old energy formalism (see Subsection 3.2.1) which parameterizes a simple energy criterion for envelope ejection via an efficiency term. It is well known that this prescription for envelope ejection is incomplete, if not problematic (see, e.g., Soker 1992, 2017; Clayton et al. 2017; Glanz & Perets 2018; Ivanova et al. 2020), folding many physical processes into a few parameters when perhaps additional criteria should be included. In fact, a structural term was added to this formalism to include the effects of stellar structure on envelope ejection (de Kool 1990), and though there are several functional forms applied in binary population synthesis (e.g., Xu & Li 2010a,b; Claeys et al. 2014), it is often simply set to a value of $\lambda = 0.5$ (e.g., van den Heuvel et al. 2017; Priyatikanto et al. 2022). In addition, there are known systems, such as close double white dwarfs and stellar-mass binary black holes, that the CE energy formalism cannot reproduce (Nelemans et al. 2000; Gallegos-Garcia et al. 2021).

This is especially apparent in instances of high mass ratio binary systems ($q \gtrsim 0.5$) with massive progenitors, in which the secondary may be of similar mass to the compact core of the primary. In these systems, the secondary provides enough energy to eject the entire envelope at large separation, implying that the remnant binary should be widely separated, yet dozens of gravitational wave detections of merging massive stellar-mass binary black holes (BBHs; Abbott et al. 2023) suggest that there may be more to the story. Though the dynamical formation channel may dominate the rates for these systems (Safarzadeh 2020; Rodriguez et al. 2021), there are studies that suggest CE binaries are still viable progenitors (e.g., Murguia-Berthier et al. 2017; Zevin et al. 2021), and the consideration of other important physical processes in the 1D treatment of CE is critical to understanding when the energy criterion for envelope ejection might be relevant to these and other CE binaries.

Additionally, the numerous studies that apply 3D hydrodynamics codes to the CE problem provide important clues that suggest the energy budget alone is not predictive of envelope ejection (for an in-depth review, see Röpke & De Marco 2023). No global simulations of a CE episode have been able to reproduce the envelope ejection and close orbits expected based on the energy formalism, with the notable exception of Law-Smith et al. (2020a), who remove the outer envelope of the primary prior to starting their suite of simulations. Other energy sources, such as recombination energy, are invoked to account for these deficits (e.g., Moreno et al. 2022), but the degree to which these sources contribute to envelope ejection is still debated. The focus of this work grew out of an oft-cited reason for ending these computationally expensive simulations: after the secondary settles into some larger-than-expected orbit, even if the remnant of the primary is still adjusting or ejecting material, the evolution timescale simply becomes too long. This suggests that some combination of inspiral and envelope adjustment timescales may carry more predictive power about envelope ejection than the energy formalism.

Importantly, it is not just the global timescales for the envelope that are meaningful for CE ejection. Because the main heating source during CE inspiral are asymmetrical shocks created in the envelope by the plunging secondary, the manner in which the local envelope interacts with and is impacted by the secondary must be considered. To illustrate, in the energy formalism's treatment of CE (e.g., initial conditions for simulations of Law-Smith et al. 2020a; Wu et al. 2020), energy deposition from the secondary's orbital decay is assumed to be instantaneous and fully distributed throughout the envelope at the radius of the secondary's position, meaning that once the energy budget is sufficient to unbind the envelope beyond that radius, it is more or less assumed that the envelope material outside that radius is both unbound and ejected. In more sophisticated models using 1D hydrodynamics (e.g., Fragos et al. 2019), energy deposition is still instantaneous and fully distributed throughout the envelope at the radius of the secondary's position, though allowing the envelope to respond in a slightly more physical way by expanding; therefore that material is energetically unbound but not instantaneously ejected. In reality, CE ejecta do not appear to have experienced instantaneous or spherically uniform energy deposition as evidenced by large discrepancies between ejecta velocity and escape velocity in luminous red novae (Matsumoto & Metzger 2022), and global 3D CE models are in agreement, displaying complex outflow morphology and velocity distributions (e.g., MacLeod et al. 2018b).

The manner in which shock-heating occurs locally in the envelope affects the timescales for both envelope expansion and ejection, as well as the inspiral of the secondary. The impact of these shocks during dynamical CE inspiral has been extensively explored and parameterized through a combination of 1D stellar model analysis and a large suite of 3D hydrodynamical simulations using a "wind tunnel" morphology focused locally on the secondary (CE drag formalism; MacLeod & Ramirez-Ruiz 2015a,b; MacLeod et al. 2017b; De et al. 2020; Everson et al. 2020), the results of which are foundational to this work. Crucially, orbital energy deposited in the envelope is shared inward as well as outward, effectively reducing the energy available to unbind external material, and even material that is energetically unbound may take time to be ejected, depending on conditions exterior to that material. It is possible for envelope material to be both unbound and still present to create drag on the secondary and further reduce its orbital separation. Hence, as we will demonstrate, incorporating these timescales into a framework for CE ejection not only shifts expected outcomes from CE binaries, but provides nuanced information about how inspiral will proceed.

In what follows, we examine a range of binary systems applying tools from the CE drag formalism (see Subsection 3.2.2) to 1D stellar models and analyze a selection of representative binaries simulated with 3D hydrodynamics in order to determine the role of several characteristic timescales in successful CE ejection. In Section 3.2, we present various considerations regarding the energy budget of a CE event and introduce the ejection parameter. In Section 3.3, we discuss energy transport in the envelope and introduce basic timescales for orbital decay and energy sharing in the stellar envelope through the dynamical parameter. We proceed to combine the dynamical and ejection parameters to analyze a selection of representative binary systems in Section 3.4, comparing expected outcomes and showing results consistent with our high-resolution 3D simulations. In Section 3.5, we discuss special considerations for the presented CE framework and future improvements. Finally, we conclude in Section 3.6.

3.2 Drag and the Energy Formalism

3.2.1 The Energy Criterion

The natural outcomes of a CE phase include either the merger of the core of the primary with the secondary or the preservation of the binary through the ejection of the envelope. According to the standard CE energy formalism (van den Heuvel 1976; Webbink 1984; Livio & Soker 1988; de Kool 1990; Iben & Livio 1993), the resulting configuration depends on the fulfillment of an energy criterion in which the orbital energy deposited into the envelope by the secondary is compared to the binding energy of the envelope: if the energy deposited is at least equal to the binding energy, the envelope ejection is said to be successful. The orbital energy deposited due to orbital tightening is defined as

$$\Delta E_{\rm orb} = \frac{GM_1M_2}{2a_{\rm init}} - \frac{GM_{\rm enc}M_2}{2r}, \tag{3.1}$$

in which G is the gravitational constant, M_1 is the total mass of the extended primary star, M_2 is the mass of the embedded secondary, $a_{\rm init}$ is the initial separation of the primary and secondary, r is the distance of the secondary from the primary's core after tightening, and $M_{\rm enc}$ is the enclosed mass of the primary within radius r (i.e., $M_{\rm enc} = M(r)$).

It is understood that not all of the orbital energy may be deposited, or will contribute to the ejection of the envelope. In fact, it is likely there are other sources of energy that could be tapped to assist in ejecting the envelope. Therefore, this quantity is modified by an efficiency term α that functions as a "catch-all" for energetic contributions and deficits during a CE phase: if considering only orbital energy deposition, then $\alpha \leq 1$, but if folding in contributions from other sources such as recombination energy, α can increase the available energy budget by up to a factor of ~ 5 (Sand et al. 2020). It is this modified quantity that must be sufficient to unbind the envelope; this defines the so-called α-formalism: $\alpha \Delta E_{\rm orb} \geq E_{\rm bind}$. We define the total binding energy of the envelope as equivalent to the gravitational binding energy

$$E_{\rm grav} = \int_{M_{\rm core}}^{M_1} -\frac{G M_{\rm enc}}{r} dm \equiv \frac{G M_1 M_{\rm env}}{\lambda R}, \tag{3.2}$$

in which $M_{\rm core}$ is the mass of the core of the primary, $M_{\rm env}$ is the total mass of the envelope of the primary ($M_1 - M_{\rm core}$), and λ is a parameter included to account for differences in stellar structure amongst primaries. We use the integrated form in the analysis that follows. For simplicity, we assume $\alpha = 1$

and do not include additional energy source terms nor the specific internal energy of the gas in our binding energy calculation (Equation 3.2). This places our results in the limiting case in which all available energy due to orbital decay contributes to the unbinding of the envelope, but the envelope itself is more difficult to unbind.

3.2.2 Energy Deposition and Drag

The main mechanism by which orbital energy is deposited during a CE phase is dynamical friction from shocks caused by the embedded object's motion through the envelope. The framework of the CE drag formalism quantifies the local effects of these shocks by detailing the relationships between key flow parameters and the accretion and drag force that act upon the secondary (MacLeod & Ramirez-Ruiz 2015a,b; MacLeod et al. 2017b; De et al. 2020; Everson et al. 2020). We briefly introduce the relevant binary and flow parameters here; for a more in-depth introduction, we refer the reader to MacLeod & Ramirez-Ruiz (2015a,b) and MacLeod et al. (2017b).

A typical CE binary, in which the primary is more massive than the secondary, is characterized by the global mass ratio $q = M_2/M_1 < 1$. Inspiral and envelope ejection, however, are partially characterized by the radius-dependent local mass ratio

$$q_{\rm r} = \frac{M_2}{M_{\rm enc}}, \tag{3.3}$$

which increases as the orbit decays and can approach unity in high mass, high mass ratio ($q > 0.4$) systems as the secondary nears the core.

The velocity of the secondary during inspiral can be described as a modified Keplerian orbit:

$$v_\infty = f v_{\rm Kep} = f\sqrt{\frac{G(M_{\rm enc} + M_2)}{r}}, \tag{3.4}$$

in which f is the fraction of Keplerian velocity of the embedded object relative to the envelope. In the f term is incorporated both the degree of corotation with the envelope and the degree to which drag has reduced the velocity from Keplerian.

The relative velocity v_∞, when combined with the stellar structure of the primary and the mass ratio of the system, defines several key quantities relevant to how inspiral proceeds, borrowing from the framework for flows and accretion developed by Hoyle & Lyttleton (1939) and Bondi & Hoyle (1944), hereafter HLA. The movement of the secondary relative to the flow of the envelope is characterized by the Mach number

$$\mathcal{M}_\infty = \frac{v_\infty}{c_{\rm s}}, \tag{3.5}$$

in which $c_{\rm s}$ is the sound speed of the oncoming gas. Except in cases of very low mass ratio, typical CE inspirals span a range of $\mathcal{M} \sim 1 - 5$, with higher values possible in the outer envelope, though these regions are often disturbed or expelled due to mass transfer before CE onset (MacLeod & Loeb 2020b).

In HLA and the CE drag formalism, the characteristic length scale for the impact of the secondary on the envelope during inspiral is the accretion radius

$$R_{\rm a} = \frac{2GM_2}{v_\infty^2}, \tag{3.6}$$

effectively a gravitational "sphere of influence" on the surrounding gas. The accretion radius quantifies the extent of the reach of the secondary deeper into the star, such that any gas within this distance of the secondary will be attracted and produce a drag force. Thus, for envelope ejection to effectively end inspiral, all envelope with an $R_{\rm a}$ of the secondary must first be unbound. This presents $R_{\rm a}$ as a proxy, to first order, for the inward radial extent of envelope material that must be impacted by the initial energy deposition from shocking (see Subsection 3.2.3). This is justified by CE wind tunnel simulation results (MacLeod & Ramirez-Ruiz 2015a; MacLeod et al. 2017b; De et al. 2020), which show at typical values of $\mathcal{M}_\infty$ and $q_{\rm r}$ that shock-heating does travel inward, but its reach is limited as the dimensionless density gradient ϵ_ρ of the stellar envelope increases.

For envelopes that can be approximated as a constant entropy polytrope, this density gradient is directly related to the Mach number and mass ratio by the following relation shown by Everson et al. (2020):

$$\epsilon_\rho = \frac{2q_{\rm r}}{(1+q_{\rm r})^2}\mathcal{M}_\infty^2, \tag{3.7}$$

meaning only two of these flow parameters must be known in order to characterize the effects of the flow on the CE inspiral.

These effects are quantified in the CE drag formalism by the drag coefficient C_d, the value of which derives from the steady-state time-averaged drag force F_d measured in the suite of CE wind tunnel simulations normalized by the HLA drag force such that

$$F_\mathrm{d} = C_\mathrm{d} \pi R_\mathrm{a}^2 \rho_\infty v_\infty^2, \tag{3.8}$$

in which ρ_∞ is the local density at radius r. The functional forms of C_d for $\gamma = 4/3$ and $5/3$ polytropic equations of state were introduced by De et al. (2020), allowing the straightforward integration of the drag force for inspirals through a broad range of stellar profiles, and in turn the orbital energy deposition rate through the relation

$$\dot{E}_\mathrm{orb} = -F_\mathrm{d} v_\infty. \tag{3.9}$$

In Figure 3.1, we show a comparison of the change in orbital energy due to tightening (ΔE_orb) as a function of mass for HLA ($C_\mathrm{d} = 1$, top panel) and the CE drag formalism (bottom panel) in a range of systems we will presume are undergoing CE evolution. The stellar models used in these calculations and all that follow are generated using the MIST package (Choi et al. 2016; Dotter 2016) with `MESA` v7503 (Paxton et al. 2011, 2013, 2015) for primaries with $Z = Z_\odot$ (appropriate for modeling galactic CE events) and, due to limitations in MIST at low metallicity and high mass, `MESA` v10398 (Paxton et al. 2011, 2013, 2015, 2018) for primaries with $Z = 1/50 Z_\odot$ (appropriate for modeling

Population III binaries, such as those suggested as possible BBH progenitors). This analysis and those that follow are performed for primaries across a wide range of mass (1-90 $M_{\odot}$), age (TAMS to stellar death), and initial separation with global mass ratio q ranging from 0.1 to 0.5. We assume that all secondaries are non-accreting during inspiral and apply a core-envelope boundary definition of hydrogen mass fraction $X_{\rm H} < 0.1$. It is worth noting that the core-envelope boundary is not well defined in all evolved stars (Tauris & Dewi 2001); in this work, we choose this boundary according to the standard definition. The system in Figure 3.1 is selected to illustrate a problematic high mass case (mentioned above) in which the binding energy (green) as calculated with the standard energy formalism is lower than the change in orbital energy (dashed lines) at every stage of inspiral, implying that, should a CE episode take place, the secondary will easily eject material deep enough into the primary that inspiral will be interrupted, leaving the binary preserved but at wide separation. The integrated values for $\Delta E_{\rm orb}$ (dot-dashed lines) agree with such a narrative, with only minor differences within a factor of a few between the integrated HLA and CE drag formalism energy deposition rates.

We emphasize here that there is nothing in the CE drag formalism that impacts the energy budget of a CE event. What this formalism adds to the 1D analysis of a CE event, however, is two-fold: it provides a proxy for the reach of energy deposition during inspiral, illustrated in the following subsection, and it provides a timeline for energy deposition and inspiral, which we explore further in Subsection 3.3.2.

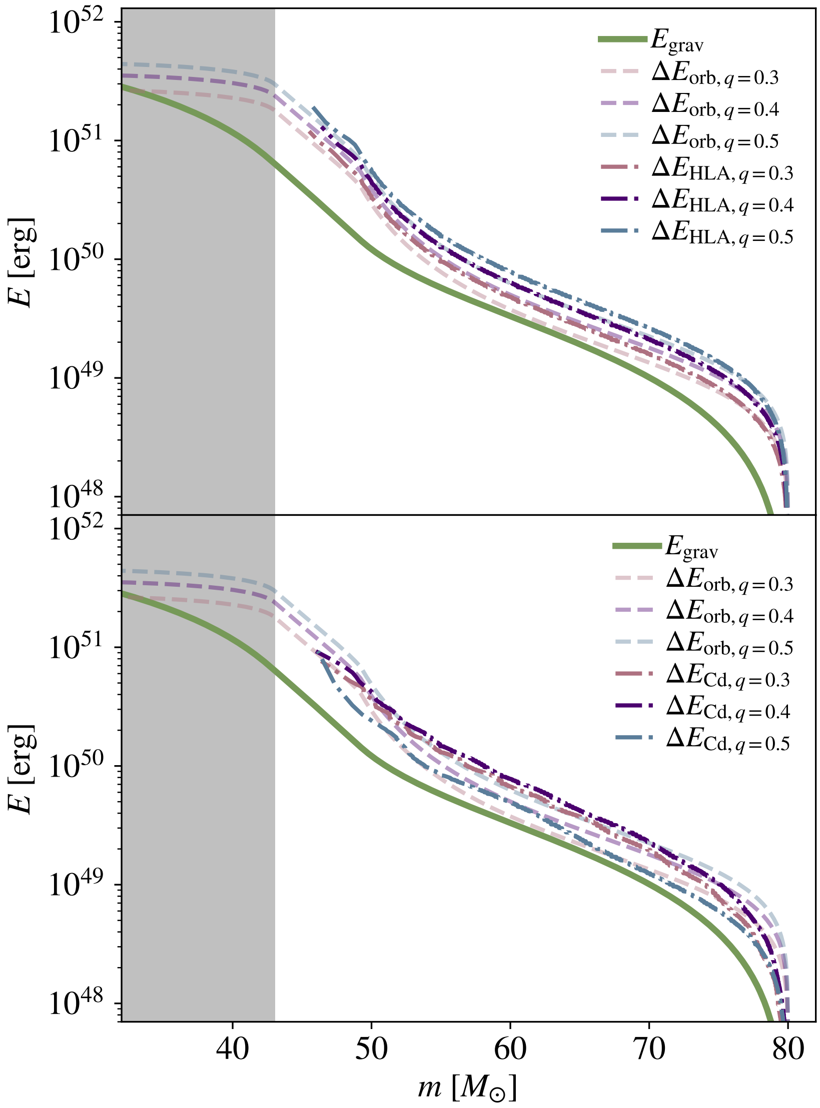

Figure 3.1 Comparison of integrated $\Delta E_{\rm orb}$ using the HLA drag force (upper panel) and the CE drag formalism (lower panel) over the CE energy budget according to the standard energy formalism for an $80M_\odot$, $\sim 800R_\odot$ primary with metallicity of $1/50Z_\odot$. The green curve represents the integrated gravitational binding energy. Pink, purple, and blue curves represent the change in orbital energy during inspiral for mass ratios of 0.3, 0.4, and 0.5, respectively, with dashed lines calculated as in Equation 3.1 and dot-dashed lines integrated numerically with the energy dissipation rate as described in Equations 3.8 and 3.9. The drag coefficient for the top panel is set to unity, and the drag coefficient for the bottom panel varies according to the fitting function for a gas of $\gamma = 4/3$ from De et al. (2020). Though some variation exists between the $\Delta E_{\rm orb}$ curves produced by the energy and drag formalisms, they are in agreement within a factor of a few. The energy budget from orbital tightening is not impacted by the inclusion of drag, which is to be expected.

3.2.3 Inspiral and Energy Balance

In spite of its flaws, the energy formalism remains in widespread use and is therefore a well-established foundation for any theoretical framework for CE ejection. As mentioned above, the types of curves shown in Figure 3.1 are often used to select likely progenitor systems for the attempted modeling of known post-CE systems with 3D hydrodynamics (with a notable lack of success), and even to make assessments about the final separation of systems undergoing CE based on the coordinate where the $\Delta E_{\rm orb}$ curve outpaces that of $E_{\rm grav}$. This is of course an oversimplification of the ejection process, and precludes the modeling of systems that appear to have too much orbital energy to initiate a CE phase without interruption. The extent of the envelope that must be ejected in order to stop or prevent inspiral is not considered. Similarly, in systems in which the outer regions of the envelope are very loosely bound, the initiation of a CE phase appears unlikely, yet results from 3D hydrodynamical models of CE onset by MacLeod & Loeb (2020b) suggest that these same regions are stripped prior to onset and do not prevent the CE phase.

Without changes in the total energy budget of the CE binary, it is possible to incorporate more physical aspects of the ejection process into the type of 1D analysis championed by the energy formalism. In Figure 3.2, we show two examples based on the system from Figure 3.1. The binding energy according to the standard energy formalism (green) lies below the curves representing the change in orbital energy (dashed lines) for mass ratios of 0.3 (pink), 0.4, (purple), and 0.5 (blue). The expected primary mass remaining after pre-CE mass loss of $0.25M_2$ according to the prescription of MacLeod & Loeb (2020b) is denoted by vertical lines colored according to their corresponding mass ratio.

As discussed in Subsection 3.2.2, any material that is not ejected within R_a of the secondary will gravitationally interact and create drag, furthering the inspiral. In the top panel, to approximate the binding energy that must be overcome not simply to eject the envelope beyond mass coordinate m but to stop inspiral, we adjust E_grav to include the binding energy of material within an accretion radius of the secondary such that

$$E_{\mathrm{grav}+R_\mathrm{a}} = \int_{M_1}^{M(r-R_\mathrm{a})} \frac{GM_\mathrm{enc}}{r-R_\mathrm{a}} dm, \tag{3.10}$$

shown in solid pink, purple, and blue. Alternatively, the bottom panel makes a similar approximation by substituting the effective radius of the secondary's Roche lobe R_Roche according to Eggleton (1983), such that

$$\frac{R_\mathrm{Roche}}{r} = \frac{0.49q_\mathrm{r}^{2/3}}{0.6q_\mathrm{r}^{2/3} + \ln(1+q_\mathrm{r}^{1/3})}, \tag{3.11}$$

for R_a in Equation 3.10. Immediately apparent is that the narrative for this system's CE evolution is dramatically altered for the q values shown: if we assume onset occurs at the mass loss boundary, both approaches suggest the secondary will inspiral through $10 - 25M_\odot$ of envelope before ejection that could interrupt inspiral is energetically favorable. A binary that the energy formalism suggests would not undergo CE at all could, in fact, be a close BBH progenitor.

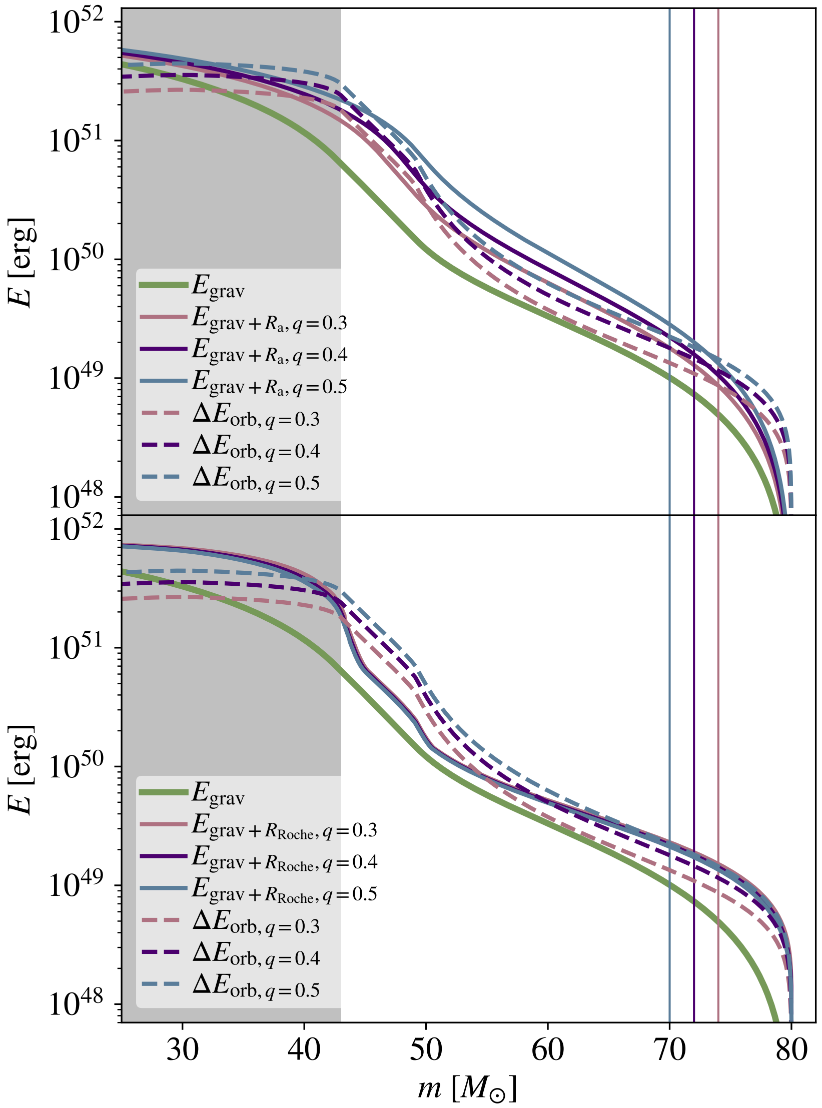

Figure 3.2 The CE energy budget according to the standard and adjusted energy formalism for an $80 M_\odot$ stellar model at $1/50 Z_\odot$ and sample secondaries of $q = 0.3$ (pink), 0.4 (purple), and 0.5 (blue). $E_{\rm grav}$ according to the standard energy formalism is shown in green, with dashed lines representing $\Delta E_{\rm orb}$ values. The expected remnant envelope mass after pre-CE mass loss is denoted by vertical lines with color corresponding to the relevant q value. The stellar core of the primary is shown in grey. *Upper panel*: $E_{\rm grav}$ adjusted to include material within R_a of the secondary for $q = 0.3, 0.4, 0.5$ is shown in solid pink, purple, and blue, respectively. *Lower panel*: $E_{\rm grav}$ adjusted to include material within $R_{\rm Roche}$ of the secondary for $q = 0.3, 0.4, 0.5$ is shown in overlapping solid pink, purple, and blue, respectively. Differences in $R_{\rm Roche}$ for these q values are on order of 10%, which is comparable to the width of the curve in mass coordinates.

Caveats for this approach include the treatment at small separation, particularly when R_{a} or R_{Roche} penetrate the core. As shown in the CE wind tunnel simulations (MacLeod & Ramirez-Ruiz 2015a; MacLeod et al. 2017b; De et al. 2020), the presence of a steep density gradient sharply redirects shock-heated material outward; the core boundary in a post-main sequence star possesses a much stronger density gradient than any portion of the envelope, suggesting that the core may be preserved and no part of its binding energy need be overcome for the CE episode to be brought successfully to its end. In addition, these adjustments to E_{grav} shift where envelope ejection is shown to be energetically favorable, but they still fail to account for non-instantaneous energy sharing throughout the envelope, which we address in Section 3.3.

3.2.4 Binary Profiles in Terms of Ejection Parameter

To more easily parse where the aforementioned energy criterion for ending the CE episode is satisfied in a CE system profile, we introduce an ejection parameter ξ which specifies the total change in orbital energy at r normalized by the gravitational binding energy of the envelope at $r - R_{\mathrm{a}}$, such that

$$\xi = \frac{\Delta E_{\mathrm{orb}}(r)}{E_{\mathrm{grav}}(r - R_{\mathrm{a}})}. \tag{3.12}$$

When this ratio is above unity at a given position, envelope ejection sufficient to end inspiral (hereafter, sufficient ejection) is energetically favorable.

A few representative examples of ξ values for four types of CE systems are shown in Figure 3.3 with primary mass and global mass ratio denoted. The dark blue curves represent ξ with respect to r, with energetically favorable ejection regions shaded in blue. We exclude regions in which pre-CE mass loss is expected (dotted). The selected binary profiles represent typical progenitors of a merger (upper left), double white dwarf (DWD; upper right), binary neutron star (BNS; lower left), and BBH (lower right).

In the merger case (upper left), the only region with $\xi > 1$ lies where mass loss is expected during onset, showing that inspiral will continue until the secondary reaches the core, as the remaining orbital energy is insufficient to unbind the envelope. These features are reproduced in the 3D hydrodynamic merger simulation discussed in Subsection 3.4.3. The DWD and BNS systems (upper right and lower left, respectively) show similar profiles with sufficient ejection only becoming possible very close to the core. These cases are consistent with values of $\alpha \sim 0.2 - 0.3$, similar to those found in detailed models of these types of systems (e.g. Law-Smith et al. 2020a; Scherbak & Fuller 2023). In the BBH case (lower right), a very slim margin for success is shown within $10 R_\odot$ of the core, though ξ values are likely higher in this region if the effects of the steep local density gradient are accounted for.

As mentioned above, ξ alone cannot predict if binarity will be preserved in a CE system. Because energy transport does not occur instantaneously throughout the envelope, envelope properties related to energy sharing must be incorporated to provide a better prediction of the degree to which envelope ejection is successful and the final separation of the remnant binary.

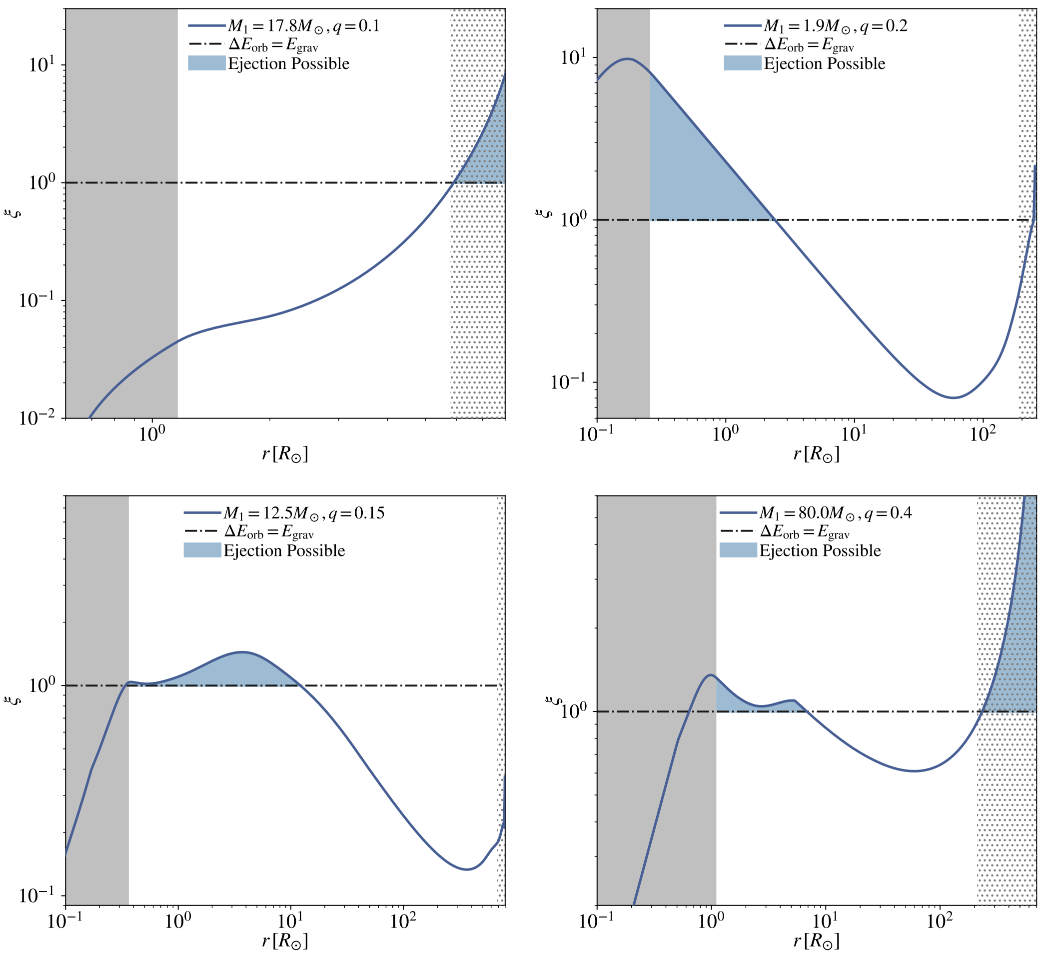

Figure 3.3 Representative examples of ejection parameter ξ in four types of CE systems. Dark blue curves denote the change in orbital energy $\Delta E_{\rm orb}$ with respect to r normalized by the local value of gravitational binding energy $E_{{\rm grav}+R_{\rm a}}$. Shaded blue regions represent where the energy criterion for ejection of the stellar envelope outside of location $r - R_{\rm a}$ is met. The core of the primary is shown in grey, with expected pre-CE mass loss denoted by the dotted outer region. *Upper left*: A merger progenitor system with TAMS primary of $17.8 M_\odot$ and mass ratio 0.1, as used for the merger simulations of Hutchinson-Smith et al. (2023) and Everson et al. (2023). *Upper right*: A DWD progenitor system of a $1.9 M_\odot$ red giant primary with mass ratio 0.2. *Lower left*: A BNS progenitor system with a $12.5 M_\odot$ red supergiant with mass ratio 0.15, as used for the BNS progenitor CE simulations of Law-Smith et al. (2020a). *Lower right*: A BBH progenitor system with an AGB primary of $80 M_\odot$ and mass ratio 0.4.

3.3 Energy Sharing in the Envelope

3.3.1 Thoughts on Energy Transport

Though common use of the energy formalism depends upon the assumption of instantaneous energy sharing in the envelope to make prescriptions about the final configuration of post-CE binaries, global 3D hydrodynamical simulations of the CE phase have shown a stubborn lack of envelope ejection even when the energy criterion is satisfied (see Röpke & De Marco 2023, and references therein). Worth noting is that many of these simulations model the primary as a polytrope or envelope with point mass core, which may also impact the final stages of the CE phase in important ways since the response of the core to mass loss is neglected. However, such simplifications are often a computational necessity due to resolution constraints, and where resolution isn't the issue, the timescales in play often are.

Yet, these results may not all be caused by numerical shortcomings; the initial conditions chosen for simulations often derive from the use of the energy formalism as a sort of "pre-screening" tool that informs whether successful CE ejection should be expected. Without consideration of how the energy deposition from the secondary is diffused through the envelope as a whole, and how the envelope might respond, the energy formalism may be able to predict whether the envelope is ejected, but alone it cannot predict whether or not binarity will be preserved. The envelope, bound or unbound, must effectively vacate the secondary's orbit in order to stop inspiral, and if it's unable to do so, the continued drag force will further tighten the orbit. In other words, we cannot equate being unbound with being ejected.

Here we take a closer look at how inspiral and envelope structure can be used to characterise non-instantaneous heating in the envelope, presenting a possible constraint on where sufficient ejection may occur.

3.3.2 Relevant Timescales

Typical timescales for orbital decay and thermal diffusion fail to capture key aspects relevant to the CE phase, especially in extended, high mass ratio systems in which the thermal diffusion timescale is often much longer than the duration of inspiral. Of interest here are how the orbital decay is related to the gas with which the secondary is interacting, and how quickly the resulting shocks are able to diffuse through the envelope.

We define a CE-specific timescale for orbital decay due to drag as

$$\tau_{\rm insp} = -\frac{R_{\rm a}}{\dot{a}}, \tag{3.13}$$

in which a is the semi-major axis of the secondary's orbit. In a nearly circular inspiral, $\dot{a} \approx v_{\rm rad}$ for the secondary. We invoke the accretion radius $R_{\rm a}$, the standard length scale for the CE drag formalism, as a measure of the depth of envelope material that the secondary is effecting gravitationally as it moves through the medium. The inspiral timescale quantifies how long it takes for the secondary to plunge on the order of its gravitational reach: if $\tau_{\rm insp}$ is similar to or less than the orbital period throughout inspiral, then in principle the secondary is continuously plunging through undisturbed envelope.

We approximate the timescale range for energy transport through a local shell of envelope material:

$$\frac{\pi r}{v_{\rm Kep}} < \tau_{\rm SH} < \frac{\pi r}{c_{\rm s}}, \tag{3.14}$$

in which the maximum velocity for the shock induced by the secondary ($v_{\rm Kep}$) and the sound speed of the gas at r ($c_{\rm s}$) provide limiting cases. This is a measure of the traversal time of the heat source in the envelope and increases with increasing drag.

3.3.3 Binary Profiles in Terms of Dynamical Parameter

It is the way in which these two timescales relate that reveals how inspiral proceeds. We introduce the dynamical parameter β as the ratio of interest:

$$\beta = \frac{\tau_{\rm insp}}{\tau_{\rm SH}}. \tag{3.15}$$

This is a measure of the efficiency of shock-heating in the envelope relative to the steepness of the secondary's plunge. If the energy criterion for ejection is met, this ratio indicates whether inspiral continues or begins to regulate: if $\beta < 1$, heating is not effective enough to cause envelope ejection within $R_{\rm a}$ of the secondary before the secondary encounters undisturbed material, but if $\beta > 1$, shocks have enough time to heat the material within $R_{\rm a}$ while the secondary is still inspiraling through it, leading to expansion and reduced drag.

Figure 3.4 shows β values for inspiral of a BBH progenitor system with $M_1 = 80M_\odot$ and $q = 0.4$ in radial and mass coordinates, calculated with drag prescriptions from HLA (pink) and the CE drag formalism (blue). The integrated curve for the HLA case (dark rose) suggests efficient shock-heating relative to the steepness of inspiral through more than half the envelope, implying that as long as energetically favorable, sufficient ejection is most likely in the outer regions. Such features lend themselves to post-CE binaries with wide separation. The integrated curve for the CE drag formalism case (dark blue) suggests a steep plunge through most of the envelope, outpacing shock-heating of material within $R_{\rm a}$, leaving a window where heating is comparatively efficient within $\sim 25R_\odot$ of the core. If energetically feasible, these features lend themselves to a close post-CE binary. We note here that not all CE binaries have drastically different outcomes between the drag prescriptions, especially those with relatively shallow density gradients in the envelope (De et al. 2020).

Even the highest β value does not imply ejection if the energy criterion is not met. Conversely, a low β profile can reveal that a merger is possible even when there is sufficient energy for ejection. What the dynamical parameter provides is a nuanced view of the type of inspiral that can take place in different envelope regions based on binary properties and stellar structure, and whether the secondary is likely to interact with material that is already shock-heated.

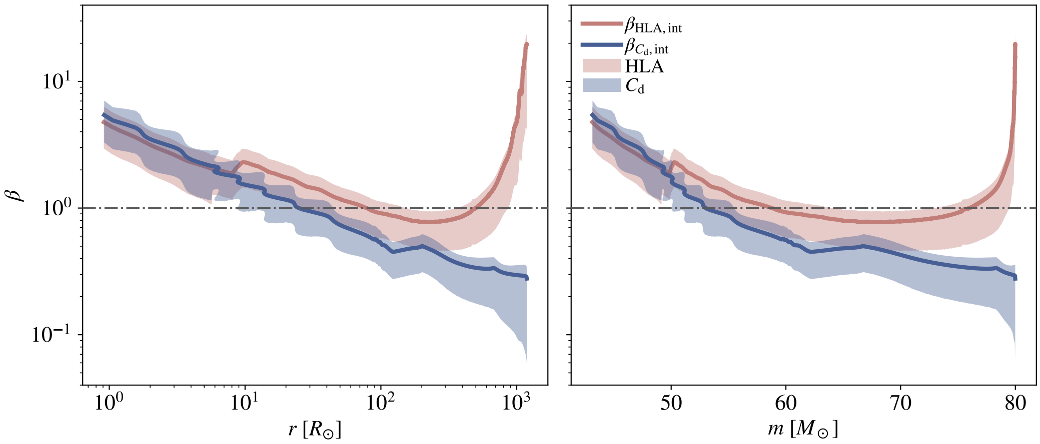

Figure 3.4 Dynamical parameter β values for a BBH progenitor system of primary mass $80M_{\odot}$, initial separation $\sim 1000R_{\odot}$, and mass ratio 0.4 in radial (left panel) and mass (right panel) coordinates. The range of integrated values using the drag prescription from HLA are shown in pink, and those using the drag prescription from the CE drag formalism (C_{d}) are shown in blue, with maximum and minimum values corresponding to those shown in Equation 3.14. The integrated HLA curve (dark rose) and C_{d} curve (dark blue) utilize τ_{SH} values incorporating the integrated velocity of the secondary during inspiral. The HLA curve shows $\beta > 1$ through $\approx 60\%$ of the stellar envelope (by radius), suggesting sufficient ejection may occur anywhere in the outer half of the stellar envelope as long as the energy criterion is satisfied. The C_{d} curve shows $\beta < 1$ in all but a few percent of the envelope, suggesting a steep plunge that slows or ends in a region with comparatively efficient energy sharing within a few tens of solar radii from the core.

3.4 Combining Ejection Criteria

3.4.1 Dynamical vs. Self-Regulated Inspiral

The narrative for a typical successful CE event is as follows:

1. After an initial destabilization or mass transfer/loss episode, onset occurs and the secondary is engulfed in the envelope;
2. Dynamical inspiral takes place, in which the secondary takes a steep plunge through a large fraction of the remaining envelope;
3. Upon encountering steep density gradients near the core boundary, the secondary transitions to a self-regulated inspiral, in which further losses of orbital energy occur on a similar timescale to the remnant envelope's thermal timescale;
4. As the envelope has had time to respond, it is finally ejected, leaving a dramatically tightened remnant binary.

The dynamical parameter β and the ejection parameter ξ provide insight into the second and third stages of this narrative when combined, especially with regard to the location where a dynamical inspiral may transition to self-regulated inspiral during a CE event.

First, we briefly discuss the expected profile for β and ξ during these two phases of inspiral. A dynamical inspiral should show inefficient energy sharing relative to the orbital decay timescale ($\beta < 1$), regardless of ξ value. This is because β is essentially normalized by the secondary's traversal time. As the defining feature of dynamical inspiral is the secondary's encountering undisturbed material as it plunges, this is guaranteed by a value of $\beta < 1$. In order to transition to a self-regulated inspiral, energy sharing should become efficient relative to the orbital decay timescale ($\beta > 1$), while the energy deposition from the secondary should be sufficient to eject the envelope ($\xi > 1$; in principle, the interface of $\beta = 1$ in a successful CE ejection is coincident with the dynamical boundary as described by Everson et al. (2020)). These combined values highlight a region of the parameter space where the secondary will encounter material it has already heated, encouraging both ejection and dramatically reduced drag.

3.4.2 Sufficient Ejection Region

Here we combine the dynamical and ejection parameters to hone in on a suggested envelope ejection region in which inspiral is likely to be interrupted. Two examples from Figure 3.3 are illustrated in Figure 3.5 with regions of $\beta > 1$ shaded in pink. In the BNS progenitor case (left), the region where the energy criterion is satisfied does not completely coincide with the region where the dynamical criterion is satisfied, creating a split between the outer and inner locations where ejection is possible. Notably, the 3D hydrodynamical simulations of Law-Smith et al. (2020a) did not pass through the outer self-regulated region, but initiated inside of it at $\sim 8R_{\odot}$ with envelope beyond $10R_{\odot}$ already removed, leading to envelope ejection and circularization at $\sim 2R_{\odot}$. In a way, that outcome is consistent with what we see here, in that

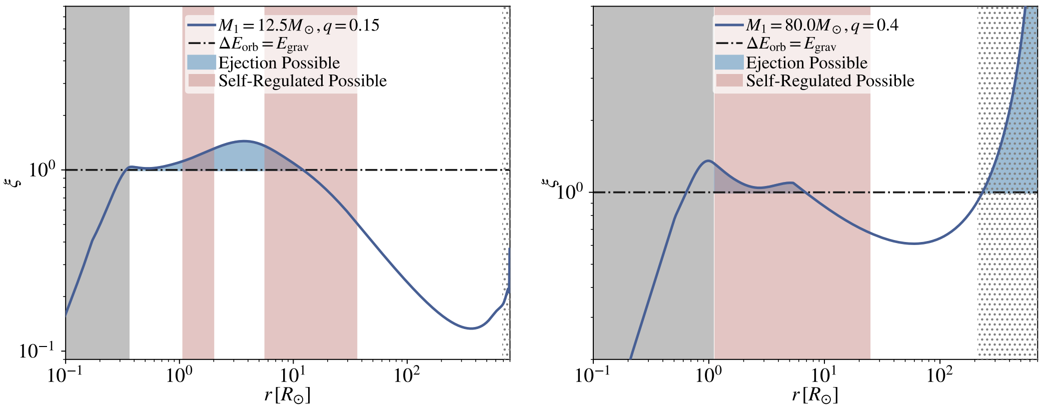

Figure 3.5 Examples of ejection parameter ξ (dark blue) in two CE example systems with regions of $\beta > 1$ highlighted in pink. Shaded blue regions represent where the energy criterion for sufficient ejection is met. Shaded grey regions represent the core of the primary, with pre-CE mass loss indicated by the dotted outer region. *Left*: A BNS progenitor system with red supergiant primary of $12.5M_\odot$ and mass ratio 0.15, as used by Law-Smith et al. (2020a). *Right*: A BBH progenitor system with an AGB primary of $80M_\odot$ and mass ratio 0.4.

the intervening envelope in which $\beta \not> 1$ is not ejected until the secondary has already passed through it. However, the β profile here suggests that if Law-Smith et al. (2020a) had initiated at a distance beyond the outer self-regulated region, sufficient ejection might have occurred at a distance of $\sim 10R_\odot$ instead, interrupting further tightening.

In the BBH case (right), the ejection region is coincident with approximately half of the self-regulated region. This highlights a clear sufficient ejection region, but also has implications for the energy formalism: recall that this system, according to the standard energy formalism, is presumed to have an orbital energy budget capable of ejecting the envelope at very wide separation (i.e., Figure 3.1) to the point of avoiding a CE episode altogether, but its β profile suggests that after initial mass loss prior to onset, a dynamical inspiral is favored even with an energy surplus, allowing a degree of tightening that would reduce the system's separation by nearly two orders of magnitude.

As the energy formalism has been used for decades to "pre-screen" successful CE systems prior to more complex modeling and simulations, the combination of ξ and β carries valuable additional information about the dynamic process of CE inspiral, rather than just the energy budget, that lends it to such a use.

The $\xi - \beta$ parameter space for a selection of representative CE binaries applying the HLA drag prescription and the CE drag formalism prescription are shown in Figures 3.6 and 3.7, respectively. In this parameter space, the upper right quadrant satisfies both the β and ξ criteria for sufficient ejection, i.e., the sufficient ejection region. The lower right quadrant satisfies the requirements for dynamical inspiral in which the energy deposition is sufficient for ejection, but only after the secondary has plunged further in. The lower left quadrant represents dynamical inspiral through envelope that is retained. The upper left quadrant satisfies the conditions for a shallow inspiral with low drag, such as those in very diffuse envelopes or with very low mass ratio.

The HLA curves (Figure 3.6) have higher β values across the board, which is expected as the HLA drag prescription tends to underestimate drag in CEs, leading to shallower inspiral overall (MacLeod & Ramirez-Ruiz 2015a,b; MacLeod et al. 2017b). The merger system (green) is seen to transition from a relatively slow inspiral at first (likely with pre-CE Roche lobe overflow) to a dynamical inspiral that eases as the secondary merges with the core. The

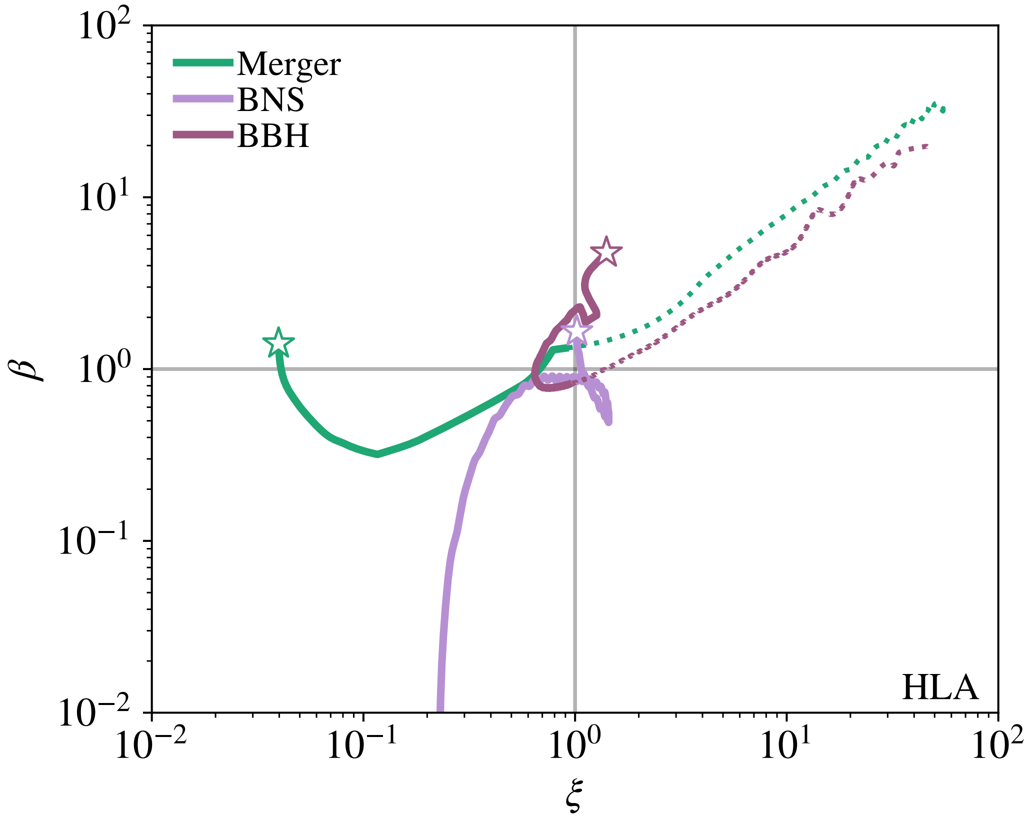

Figure 3.6 Integrated results for the HLA drag prescription in the $\xi - \beta$ parameter space for three representative example CE binaries: a merger progenitor of a TAMS $17.8 M_\odot$ star with secondary $q = 0.1$ (green), a BNS progenitor of $12.5 M_\odot$ with secondary $q = 0.15$ (purple), and a BBH progenitor of $80 M_\odot$ and secondary $q = 0.4$ (dark plum). Dotted lines denote pre-CE mass loss, solid lines denote integrated CE inspiral, and stars denote the core boundary where integration was stopped.

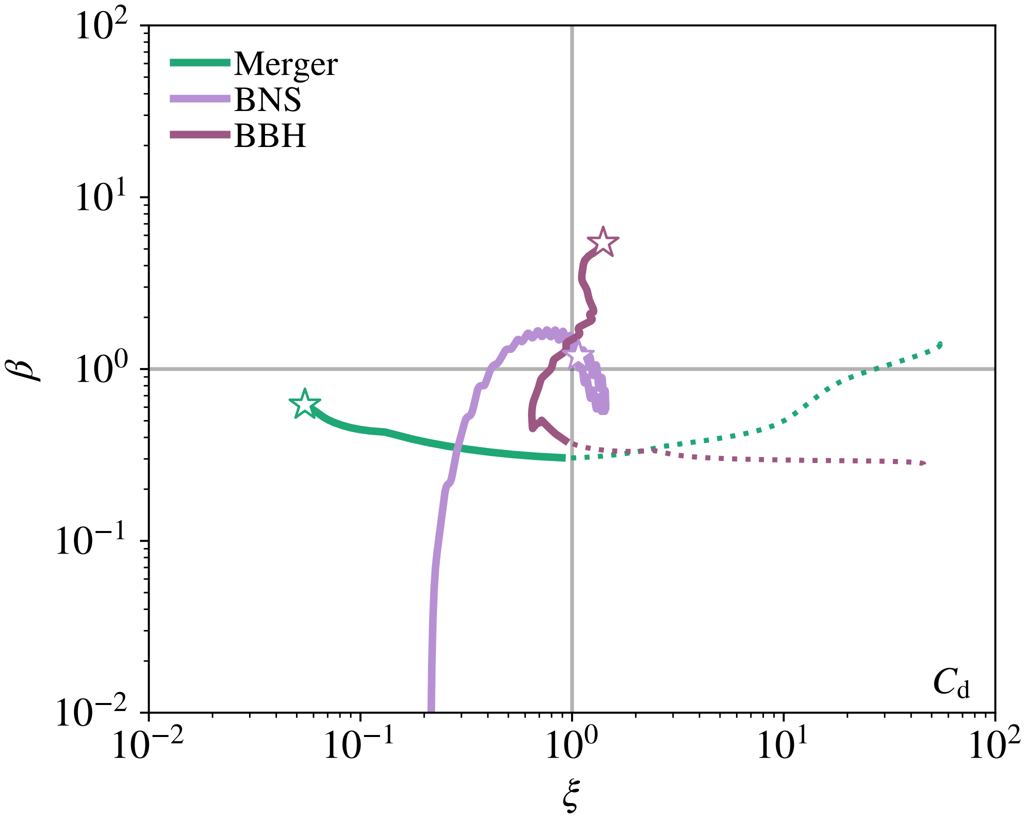

Figure 3.7 Integrated results for the CE drag formalism prescription ($C_{\rm d}$) in the $\xi - \beta$ parameter space for four representative example CE binaries: a merger progenitor of a TAMS $17.8 M_\odot$ star with secondary $q = 0.1$ (green), a BNS progenitor of $12.5 M_\odot$ with secondary $q = 0.15$ (purple), and a BBH progenitor of $80 M_\odot$ and secondary $q = 0.4$ (dark plum). As in Figure 3.6, dotted lines denote pre-CE mass loss, solid lines denote inspiral, and stars denote the core boundary where integration was stopped.

BNS progenitor system (purple) begins with a very steep plunge that slows, then steepens slightly before reaching a self-regulated phase and ejecting the envelope. The BBH system (dark plum) transitions from a brief initial plunge to a relatively shallow inspiral, then reaches the sufficient ejection region while in the self-regulated regime.

The CE drag formalism curves (Figure 3.7) have lower values overall, excluding the BNS progenitor system (purple). Though we see the same shallowing and steepening of inspiral as in the HLA case for the BNS system, the steepening includes a shift into the self-regulated and sufficient ejection regions prior to a short dynamical inspiral that again slows and leads to self-regulated inspiral. The implication is that ejection would likely occur on the first pass, rather than the second. In the merger case (green), a steep plunge ejects the outer envelope without slowing inspiral, and the secondary merges with the core dynamically. In the BBH case (dark plum), a dynamical plunge that ejects the outer envelope is slowed as it enters material that is more efficiently shock-heated, leading to successful ejection again with self-regulated inspiral.

The ability to interpret the narrative of a CE event through the $\xi - \beta$ parameter space is notable if these narratives can be validated. We proceed to initiate that process with two 3D hydrodynamical models.

3.4.3 Application to Simulations

Though it's straightforward enough to calculate these parameters from stellar models, we are in many ways trusting that the initial configuration and structure of the CE binary holds enough information to give us some predictive power. After decades of study, it is not entirely clear that this is a reasonable assumption in the case of CE evolution (Ivanova et al. 2013; Ivanova 2017). With the understanding that 3D hydrodynamical simulations also have their shortcomings, we apply the $\xi - \beta$ framework to two detailed simulation results to assess at a preliminary level whether parameter behavior is as expected.

We apply a customized setup using the 3D adaptive-mesh refinement hydrodynamics code `FLASH` v4.3 (Fryxell et al. 2000) that is able to load and fully resolve `MESA` stellar profiles in 3D with a Helmholtz equation of state for the simulation of CE interactions (for further details, see Guillochon et al. 2009; Guillochon & Ramirez-Ruiz 2013; Law-Smith et al. 2020a; Wu et al. 2020; Hutchinson-Smith et al. 2023). Due to the computationally prohibitive resolution required to simulate core-resolved extended primaries, we choose here to adapt the models of Hutchinson-Smith et al. (2023) to simulate a merger scenario and Law-Smith et al. (2020a) to simulate a BNS progenitor scenario. In the merger case, we increase the resolution to $\Delta X_{\rm min} \approx 0.029 R_\odot$ to improve fidelity around the stellar core, and adjust initial conditions to reflect those of the CE drag formalism inspiral integration with inspiral beginning at the limb of the primary. In the BNS progenitor case, we use a resolution of $\Delta X_{\rm min} \approx 0.0098 R_\odot$ and trim the envelope to $10 R_\odot$ with inspiral beginning at $8 R_\odot$ as described by Law-Smith et al. (2020a), but again adjust inspiral initial conditions to reflect those of the CE drag formalism inspiral integration.

The simulation results in the $\xi - \beta$ parameter space are shown in Figure

3.8. The dynamical inspiral in the merger simulation (green), though more extreme, is qualitatively similar to that seen in the CE drag formalism inspiral integration in Figure 3.7. As the curve proceeds right to left, a steep plunge ejects $\approx 10\%$ of the envelope by mass without interrupting the inspiral, then begins to relax before the secondary settles into the core.

Though less obvious, the BNS progenitor simulation (purple) also shows a qualitative similarity to that seen in the inspiral integration, but only the final stage leading to sufficient ejection. In Figures 3.6 and 3.7, there is an inflection point in the $\xi - \beta$ trajectory of the BNS progenitor system in which the inspiral quickly switches from becoming more dynamical to becoming less dynamical: this inflection point occurs at the peak ξ value, seen in Figure 3.5 (left panel) between two sufficient ejection regions, and the starting radius of inspiral in the simulation is just beyond this peak. The integrated curves and the simulated curves proceed upwards until they reach the sufficient ejection region next to the core, tracing very similar trajectories. The simulation ends with approximately twice the change in orbital energy of the HLA and CE drag formalism inspirals, which would likely be resolved with an improved method for calculating ξ near the primary's core in non-simulated cases.

The qualitative similarity between the simulations and integrated inspirals for both the merger and BNS progenitor cases is remarkable when considering the simplicity of the framework developed here. Though more work is needed to validate its predictive power, these preliminary results are encouraging.

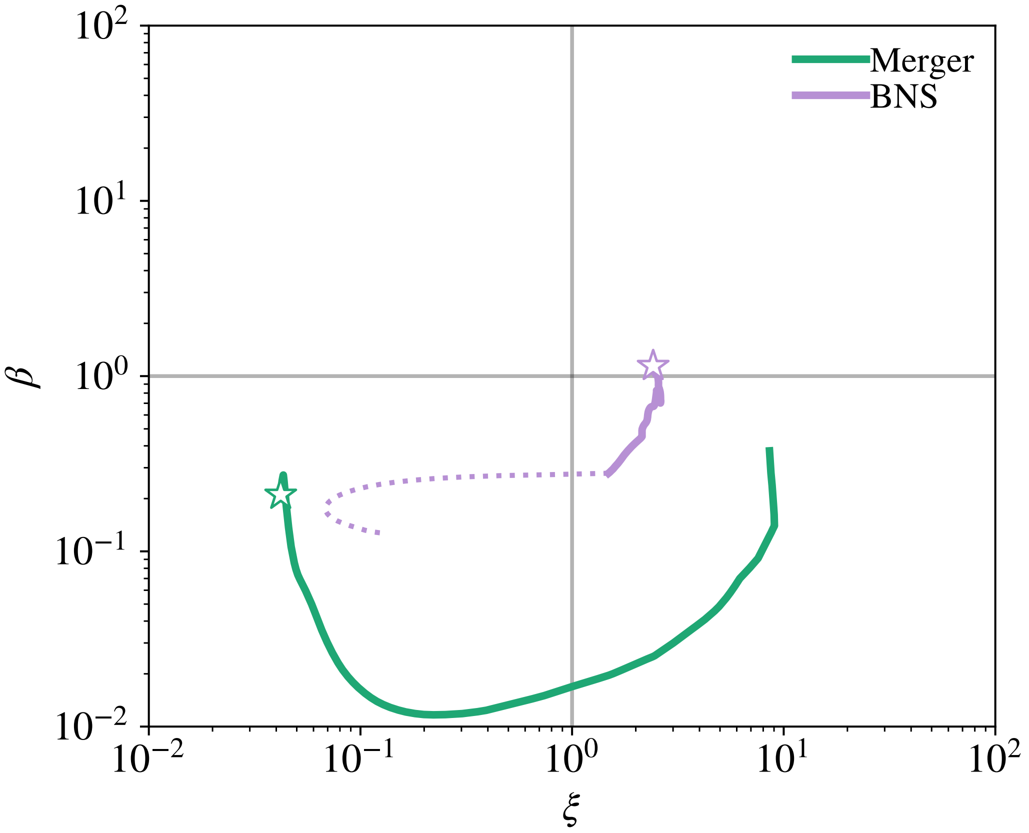

Figure 3.8 Simulation results from 3D hydrodynamical models of two CE binaries in the $\xi - \beta$ parameter space. A high-resolution core-resolved model of the merger of a $1.57M_\odot$ neutron star with a TAMS $18M_\odot$ primary is shown in green, based on the setup of Hutchinson-Smith et al. (2023) and Everson et al. (2023). A high-resolution core-resolved model of a successful CE ejection with a $1.4M_\odot$ neutron star and a $12M_\odot$ red supergiant stripped to $10R_\odot$ is shown in purple, based on the setup of Law-Smith et al. (2020a). Solid lines denote calculations from simulated inspiral, dotted lines denote calculations from integrated inspiral in non-simulated regions, and stars denote the final position of the secondary: central in the case of the merger, and circularized at $\approx 2R_\odot$in the case of the BNS progenitor.

3.5 Discussion

The promise of a simple, 1D framework to treat CE events has been elusive for decades. In spite of community consensus on its shortcomings, the standard energy formalism remains in widespread use because of its simplicity, rather than its accuracy. Our attempt here to improve upon the energy formalism with some additions and adjustments is not the first (e.g., de Kool 1990; Hirai & Mandel 2022), but is uniquely motivated by insights gleaned from the use of the CE drag formalism in investigating how inspiral proceeds in various CE systems (Everson et al. 2020).

The results outlined in Subsection 3.4.3 motivate future work analyzing additional simulation results that are representative of the general types of CE systems that are of interest, including DWD progenitors, BBH progenitors, post-main sequence stars partnered with main sequence companions, and planetary engulfments. If broadly validated, the integration tools required to perform the above analyses would provide a useful alternative approach for the community to apply in lieu of the standard energy formalism to quickly analyze CE systems, or even predict outcomes.

3.5.1 Additional Considerations

This framework still has certain shortcomings that will need to be considered moving forward. The calculation for ξ near the core boundary would benefit from the inclusion of information about the envelope's response to mass loss, as remnant envelope that will retract due to mass loss need not be included in the binding energy that must be overcome to end inspiral. Also, the CE systems detailed in this work generally have primary cores massive enough to avoid disruption by the secondary during inspiral, but this is not always the case. Some treatment for the tidal disruption of either the primary or the secondary should be included to enhance the framework's predictive capabilities.

The use of the drag coefficients from the CE drag formalism also has limitations. Though fitting formulae were developed by De et al. (2020), they are unstable at $q_{\rm r} \gtrsim 0.7$. A persistent caveat of the use of the drag coefficients is that the Cartesian geometry of the simulations from which they're derived doesn't capture the geometry of flow near the center of a star, when angular differences become important. Again, future work is required to expand both the geometry and range of mass ratios that the drag coefficients can suitably represent.

Additionally, the simple prescription for pre-CE mass loss utilized in this work does not account for changes in stellar structure that occur on the timescale of that mass loss, but future simulations will reveal if the simple prescription is nonetheless satisfactory for this framework. Understanding how the envelope responds to mass loss during onset is, again, vital to predicting if a CE event will occur or be avoided.

3.6 Summary and Conclusion

In this chapter, we reexamined the standard CE energy formalism through the lens of inspiral dynamics, introducing adjustments and additions that together create a new CE framework for predicting envelope ejection sufficient to end inspiral. We modeled a range of CE binaries in 1D, applying drag prescriptions from HLA and the CE drag formalism, and performed two 3D hydrodynamical simulations which we analyzed with the $\xi - \beta$ framework, finding that the simulation results are broadly consistent with the integrated results. We then discussed considerations for the further validation and future improvement of the $\xi - \beta$ framework.

With the development and application of the $\xi - \beta$ framework for sufficient ejection in CE episodes, we conclude that the combination of parameters built from characteristic timescales that carry information about inspiral dynamics, drag, and stellar structure with an adapted definition of the standard energy formalism presents a promising new direction for the eventual replacement of the energy formalism in widespread use. Further work is needed for refinement and validation more broadly, but in its current form, the $\xi - \beta$ framework provides a straightforward method for interpreting and predicting how inspiral will proceed in a CE episode.

3.7 Software Utilized

`MESA` (Paxton et al. 2011, 2013, 2015, 2018), `FLASH` (Fryxell et al. 2000), `matplotlib` (Hunter 2007), `NumPy` (van der Walt et al. 2011), `py_mesa_reader` (Wolf & Schwab 2017).

Chapter 4

The Art of Modeling Stellar Mergers and the Case of the B[e] Supergiant R4 in the Small Magellanic Cloud

Abstract

Most massive stars exchange mass with a companion, leading to evolution which is altered drastically from that expected of stars in isolation. Such systems result from unusual binary evolution pathways and can place stringent constraints on the physics of these interactions. We use the R4 binary system's B[e] supergiant, which has been postulated to be the product of a stellar merger, to guide our understanding of such outcomes by comparing observations of R4 to the results of simulating a merger with the 3D hydrodynamics code `FLASH`. Our approach tailors the simulation initial conditions to observed properties of R4 and implements realistic stellar profiles from the 1D stellar evolution code `MESA` onto the 3D grid, resolving the merger inspiral to within $0.02\,R_{\odot}$. We map the merger remnant into `MESA` to track its evolution on the HR diagram over a period of 10^4 years. This generates a model for a B[e] supergiant with stellar properties, age, and nebula structure in qualitative agreement with that of the R4 system. Our calculations provide evidence to support the idea that R4's B[e] supergiant was originally a member of a triple system in which the inner binary merged after its most massive member evolved off the main sequence, producing a new object of similar mass but significantly more luminosity than the A supergiant companion. The code framework presented in this paper, which was constructed to model tidal encounters, can be used to generate accurate models of a wide variety of merger stellar remnants.

4.1 Introduction

Most massive stars exist in binaries or multiples, and the inevitable interaction with their companions via mass exchange dominates their evolution (Sana et al. 2012). Of these interacting massive binaries, ≈ 25% will merge with their companion, which has significant implications for the resulting star's subsequent evolution (Podsiadlowski et al. 1992; Sana et al. 2012; de Mink et al.

2014). These mergers and related binary interactions may give rise to peculiar phenomena such as gamma ray bursts (Podsiadlowski et al. 2004; Izzard et al. 2004; Tout et al. 2011), luminous blue variables (Justham et al. 2014), and B[e] supergiants. In particular, Podsiadlowski et al. (2006) argued that products of merger events are likely to be observed as B[e] supergiants as the merger adds mass to the core of the expanding primary star, modifying the core-envelope structure and altering the star's evolution so that it naturally populates the blue supergiant region of the HR diagram.

One such B[e] supergiant is observed in the R4 system in the Small Magellanic Cloud (Zickgraf et al. 1996) along with an A supergiant companion. The observed properties of this system exhibit an Algol-type paradox, which cannot be resolved by modeling the stars as evolving in isolation (Zickgraf et al. 1996; Pasquali et al. 2000). The B[e] supergiant in R4 thus appears to be an ideal candidate for a merged stellar remnant with clear observational constraints for the initial conditions and end state of the system. However, very few such potential merger products have been identified from observations (e.g., Schneider et al. 2016).

Along with the rarity of observational constraints, realizing a fully self-consistent treatment of binary stellar mergers has been impeded by the complexity of the problem, which involves many physical processes spanning many orders of magnitude both spatially and temporally. One way to approach this is to divide the problem into separate phases, such that a different physical process dominates in each phase, and investigate each with a tailored numerical scheme (Podsiadlowski 2001).

For example, when binary stars merge, the distorted internal structure of the stars has to be taken into consideration, and one must switch to a hydrodynamical description to follow the encounter. Hydrodynamical calculations need to be employed to study the deformations and exchange of energy and angular momentum, as well as the complete merger between the binary members (Sills & Lombardi 1997; Glebbeek et al. 2013; Nandez et al. 2014; Schneider et al. 2019).

After the dust has settled, one then has to update the stellar models for the stars involved, and in the case of mergers one has to construct new models from scratch, often with highly unusual chemical compositions and physical conditions. The timescales for the stellar remnants to regain their thermal equilibrium are vastly longer than the timescales needed for dynamical equilibrium to be restored. In such cases, the merger remnant needs to be evolved in one dimension using an active stellar evolution code (Glebbeek et al. 2013; Schneider et al. 2020).

There is a history of over half a century of stellar evolution calculations (e.g. Henyey et al. 1959; Bertelli et al. 1994; Heger et al. 2000; Meynet & Maeder 2000; Paxton et al. 2011), and significant work on the hydrodynamics of stellar encounters has been done, in particular in the context of smoothed particle hydrodynamics (SPH) simulations of blue stragglers (e.g. Freitag & Benz 2005; Dale & Davies 2006; Suzuki et al. 2007) and stellar collisions (e.g. Rasio & Shapiro 1991, 1994, 1995; Sills & Lombardi 1997). Pioneering work by Sills & Lombardi (1997) emphasized the importance of bridging stellar evolution and SPH to achieve realistic collisional products.

The paucity of observations for possible mergers, let alone known merged remnants, motivates us to study the nature of unique systems such as R4 in order to be able to effectively constrain the physics of stellar mergers. As a result, we choose to develop 3D hydrodynamical simulations of mergers using the R4 system as a guide (Section 4.2). We select progenitor stars with structures that exhibit the desired core-envelope distinction and mass ratios that are consistent with the pre-merger system based on simple prescriptions for energy considerations (Section 4.3.1).

Motivated by Sills & Lombardi (1997), in this paper we self-consistently implement `MESA` stellar profiles and corresponding equations of state onto our `FLASH` 3D grid simulation. In particular, we are able to resolve both the dense stellar core and the diffuse envelope on the grid with this realistic profile instead of appealing to the gravitational potential of a point mass to represent the core of the star (Section 4.3.2), a distinction which is crucial to physically relevant simulations in the realm of stellar mergers and common envelope calculations. This approach allows us to resolve the inspiral into the inner few solar radii of the star and enforce a physically motivated stopping criterion for the inspiral. Finally, we map the merger remnant into a 1D stellar evolution code to track its position on the HR diagram as it regains thermal equilibrium. We compare the properties of the remnant and its surrounding nebula to observations of R4 in Sections 4.4 and 4.5. In Sections 4.5 and 4.6, we discuss how our methods, which encapsulate the merger process from inspiral to post-merger evolution, form a proof-of-concept for utilizing this setup to investigate similar systems.

4.2 Initial conditions

In this section, we determine which profiles are viable candidates for the pre-merger primary. We deduce minimum values of the mass unbound and energy injected into the remnant from observed properties of the R4 system. To determine which profiles can achieve these values, we look at a simple comparison of the binding energy of the envelope with the difference in initial and final orbital energies. We also look at whether the energy expected to be injected into the remnant by the secondary during the merger is able to power the excess luminosity. This allows us to generate an initial grid of potential models that will be narrowed down further in Section 4.3.1, using more careful considerations of the effects of drag on the dynamical inspiral phase of a merger.

4.2.1 Observed properties of the R4 system

The R4 system as observed by Zickgraf et al. (1996) consists of an evolved A supergiant and a B[e] supergiant companion separated by $a = 23$ AU. For the A supergiant, Zickgraf et al. (1996) derive an effective temperature $T_{\text{eff}} \approx 9500\text{–}11,000$K and fixed $\log g = 2.5$ from fitting ATLAS8 models. In addition, they estimate mass of $12.9\,M_\odot \pm 2\,M_\odot$ from radial velocity (assuming $\sin^{\mathbf{3}}\mathbf{i} = 1$). By iteratively fitting these parameters using the ATLAS8 models, Zickgraf et al. (1996) find a radius of $R = 33\,R_\odot$, which gives a luminosity of $L \approx 10^4\,L_\odot$. They also derive a mass of $12.6\,M_\odot$ from the radius and $\log g$ values. Using a similar procedure, they find $T_{\rm eff} = 27000\,{\rm K}$, $\log g = 3.2$, $R = 14\,R_\odot$, and $L = 10^5\,L_\odot$ for the B[e] supergiant companion. The mass they derive from radial velocity (R-V) is $M = 13.2\,M_\odot \pm 2\,M_\odot$, and from the radius and $\log g$ they find $M = 11.3\,M_\odot$.

The effective temperature and luminosity of the B[e] star is well described by a supergiant with a ZAMS mass of $\approx 20\,M_\odot$, which is in stark contrast with the mass estimates from both radial velocity and $\log g$. This exemplifies the Algol-type paradox, where the B[e] star appears to have reached a very different stage in its evolution than the A supergiant despite their having similar measured masses.

The system exhibits a bipolar nebula with mean expansion velocity of ~ 100 km/s and an extension of $\sim 2.4.$ pc (Pasquali et al. 2000). Assuming a constant expansion velocity for the expanding material, the nebula's age can be estimated to be $\approx 10^4$ years. Pasquali et al. (2000) conclude that the nebula was likely ejected from the B[e] supergiant as they find it to be nitrogen enriched as well as dynamically linked with the star.

4.2.2 Evolutionary history of R4

Given the observed separation, it is reasonable to assume that the B[e] star and A supergiant companion have not interacted. Therefore, in what follows, we assume that the A supergiant has evolved independently as a single star.

The observed effective temperature and luminosity of the B[e] component are not consistent with the evolution of a single star with the observationally derived mass estimate (Zickgraf et al. 1996). In order to explain this tension, we may appeal to a process which is able to inject a significant amount of energy, resulting in higher luminosity. A stellar merger, in which the B[e] component was preceded by a close binary in a widely separated triple system with the A supergiant evolving independently, is one possibility. We refer to the more massive star in the close binary as the primary, and its less massive companion as the secondary. As a result of the merger, the secondary star injects energy, mass, and angular momentum into the primary and unbinds a significant amount of envelope material. In this case, a merger remnant might be left with properties similar to those observed for the B[e] supergiant (Podsiadlowski et al. 2006).

The existence and shape of the nebula clearly indicates that mass-loss occurred in a non-spherically symmetric fashion, which favors a dynamical event that occurred $\approx 10^4$ years ago. To constrain the initial conditions of this postulated merger event, we first assume that the system consisted previously of three stellar components born at the same time: star A, which evolved into the A supergiant; star B, which represents the aforementioned primary star in the merger that we postulate resulted in the observed B[e] supergiant; and star C, which represents the secondary star engulfed during the merger. Star A is likely to have evolved in isolation, so its age should help constrain the age of the R4 system.

To estimate the age of star A, we run `MESA` (Paxton et al. 2011, 2013, 2015, 2018) simulations for stars evolving into the supergiant phase with masses similar to those derived observationally. All models are generated with `MESA` version 10398. We use initial mass 12.5 $M_{\odot}$, which is within the range reported by Zickgraf et al. (1996). In all calculations, we start with pre-main-sequence models with an initial metallicity of $Z = 0.1 Z_{\odot}$, given the system's location in the Small Magellanic Cloud. [1]

To select viable models for the A supergiant, we match the observed value of $\log g = 2.5$ (Zickgraf et al. 1996) during the supergiant phase of evolution (Figure 4.1, top panel). This leads us to our model for the A supergiant, which has an age of 1.7×10^7 years with a mass of 12.5 $M_{\odot}$ and a radius of 31 $R_{\odot}$ at that age. The mass and radius successfully match the observed mass, radius, and $\log g$ values for the A supergiant.

Since the age of R4's nebula is of the order of 10^4 years, the age of stars B and C at the time that the merger occurred must be approximately 10^4 years less than the current age of star A. Dynamical mergers are driven by the expansion of the primary star. One possibility is that star B was crossing the Hertzsprung gap at that time, such that it was entering a slightly earlier

---

[1] For other parameters not listed, all `MESA` inlists are available upon request.

stage of evolution than star A's current state (supergiant). For star B to have reached a similar stage of evolution as star A only 10^4 years earlier means that it closely matched the evolution of star A. This suggests that the primary star in the merger had a slightly higher initial mass than that of the A supergiant. With this constraint in mind, we use the `MESA` code to generate models for star B, using the same inlist as for star A but with an initial mass of $13\,M_\odot$. This choice is slightly arbitrary, but similar masses ($< \pm 1\,M_\odot$ variations) do not significantly affect the validity of our conclusions. For consistency with the age of the nebula, we limit our consideration to models for the primary which are 8×10^3 years to a few $\times 10^4$ years younger than our A supergiant models. This restricts the size of the primary to $55\,R_\odot \lesssim R \lesssim 120\,R_\odot$.

From the models within this range of radii, we select pre-merger primary profiles that have the capacity to release sufficient energy and unbind the required amount of mass. To estimate the radius at which energy will be released and mass unbound, we make use of the energy formalism, which equates the change in orbital energy of the secondary with the binding energy of the stellar envelope (van den Heuvel 1976; Webbink 1984; Livio & Soker 1988; Iben & Livio 1993). We use the following form, calculated at each radial coordinate r:

$$E_{\rm bind}(r) = \Delta E_{\rm orb} = -\frac{GM_1M_2}{2R} + \frac{GM_{\rm 1,enc}M_2}{2r} \tag{4.1}$$

where R and M_1 are the initial radius and mass of the primary, M_2 is the mass

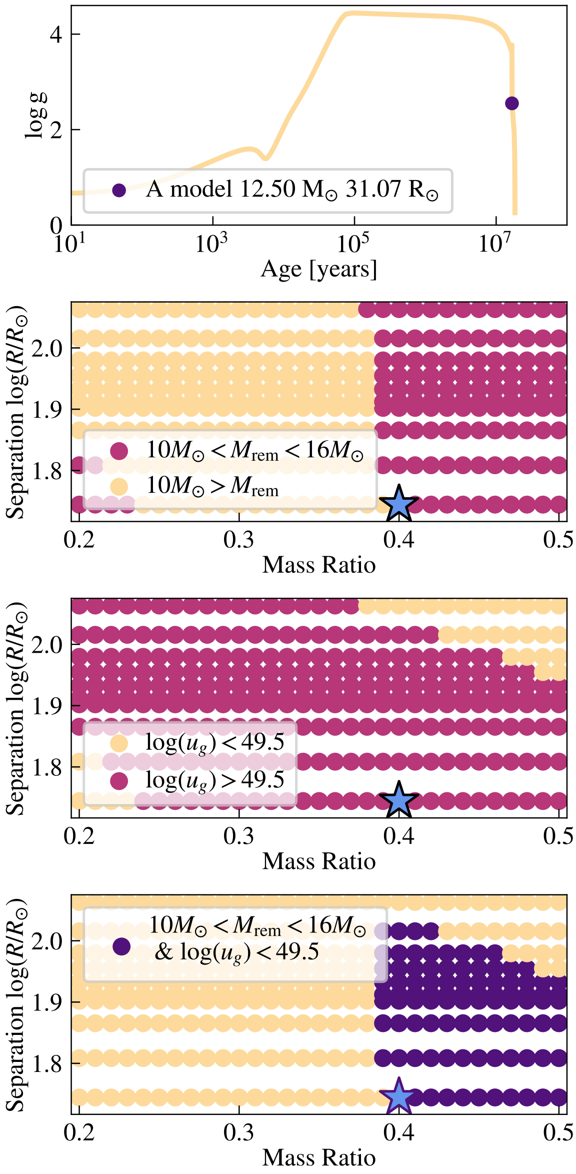

Figure 4.1 *Panel 1:* Evolution of $\log g$ over time for our A supergiant `MESA` model. The selected model (purple point) is within the mass, radius, and $\log g$ constraints of the observed R4 system. Model used for the hydrodynamical simulation performed with `FLASH` is shown as a blue star in each of the bottom three panels. *Panel 2:* Pairs of mass ratios q and binary separations at the onset of common envelope, which we equate to the radius of a range of primary models, are shown as scatter points color-coded by the resultant remnant mass. Each scatter point represents a profile during the evolution of a `MESA` model with initial mass $13.0\,M_\odot$ and companion of mass ratio $0.2 \leq q \leq 0.5$. *Panel 3:* Scatter points represent the same pairs shown in Panel 2, color-coded by the energy in ergs released by the merger. *Panel 4:* Scatter points represent the same pairs as plotted in Panel 2. Purple dots are pairs that satisfy both criteria we seek, e.g. the following: $M_{\rm rem} = 13\,M_\odot \pm 3\,M_\odot$ and $\log(E[\text{ergs}]) > 49.5$; peach points do not satisfy one or both of these criteria.

of the secondary, and $M_{1,\mathrm{enc}}$ is the enclosed mass of the primary at radius r. Here $E_{\mathrm{bind}}(r)$ is the binding energy of the stellar envelope beyond the chosen radial coordinate, and we use all available orbital energy to eject this portion of the envelope. Applying this formalism, we determine the coordinate in mass and radius where the change in orbital energy becomes larger than the binding energy of the envelope mass that is beyond this mass coordinate. We apply this criterion to a wide range of stellar profiles and mass ratios q, where $qM_{\mathrm{B}} = M_{\mathrm{C}}$ for primary mass M_{B} and companion mass M_{C}.

According to the energy formalism, the amount of orbital energy released at the mass coordinate of the crossing point is sufficient to unbind the envelope above this mass coordinate. As a result, the remaining mass of the primary star after the merger, M_{f}, is equal to this mass coordinate. The mass of the remnant $M_{\mathrm{rem}} = M_{\mathrm{f}} + M_{\mathrm{C}}$ is shown for various combinations of radii and mass ratio in the second panel of Figure 4.1. We retain for further analysis the pairs of radii and mass ratio that produce remnant masses of $13\,M_{\odot} \pm 3\,M_{\odot}$, within 2σ of the approximate derived R-V mass for the B[e] supergiant. In addition, the radius of each profile represents the pre-merger separation between the primary and its companion under the premise that the merger started as the companion came into contact with the remaining bound envelope.

Moreover, the amount of orbital energy released at this mass coordinate provides an estimate of the amount of energy injected into the merger, which is expected to increase as the secondary plunges deeper into the core until it is tidally disrupted. At the end of the secondary's inspiral, $E_{\mathrm{orb}}/E_{\mathrm{bind}} \approx$

$q^{-2/3}$, where $E_{\rm bind}$ is the binding energy. Since $q \lesssim 1$, the binding energy of the secondary, which will be deposited into the remnant is comparable or smaller than the orbital energy during the inspiral. The value of the orbital energy is therefore a simple proxy for how much energy will be deposited into the remnant. We select profiles with the capacity to inject more than $10^{49.5}$ ergs in addition to producing the desired remnant mass. The range of released energy u_g for each pair of radius and mass ratio are shown in the third panel of Figure 4.1. This estimate for the minimum injected energy was calculated assuming that the merger remnant needs to at least supply the current observed luminosity of $L_{\rm rem} \approx 10^5\, L_\odot$ for at least the age of the nebula, which is estimated to be $\approx 10^4$ years.

The parameter space of potential primaries is represented by the intersection of the regions where $10\, M_\odot < M_{\rm rem} < 16\, M_\odot$ and where $\log(u_g) > 49.5$. This intersection is shown in purple in the bottom panel of Figure 4.1. In the next section, we describe how we select our simulation initial conditions from this subset of viable pre-merger binaries.

4.3 Methods

4.3.1 Initial Models

In this section, we select models to serve as the primary star in our hydrodynamical simulations. To narrow down the grid of models generated in Section 4.2.2, we focus our simulations on the dynamical inspiral phase of a

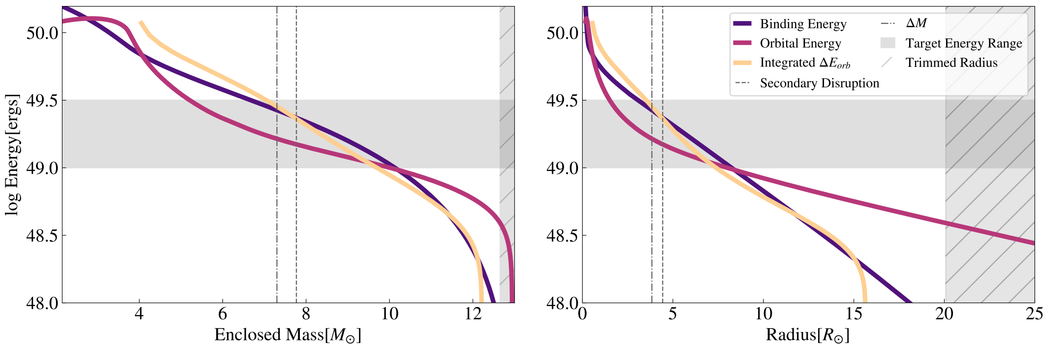

Figure 4.2 Relevant quantities for envelope unbinding during common envelope, shown on the left in mass coordinates and on the right in radius coordinates. These are presented for the model used as the initial condition for hydrodynamical simulation, with mass 12.9 $M_\odot$, radius 55 $R_\odot$, and secondary mass ratio $q = 0.4$. The radius of the companion's disruption (dashed), total primary mass minus companion mass $\delta\mathbf{M}$ (dot-dashed), and released energy needed to match observed luminosity and age (grey region) are shown. The binding energy of material exterior to a given radial coordinate (purple), the corresponding difference in orbital energy relative to the initial orbit (magenta), and the integrated orbital energy dissipated from the inspiral (peach) are plotted against the mass and radius coordinate for each model.The region of the stellar profile removed for the `FLASH` simulations is shown in the grey hatched region.

merger and take into account the effects of drag during this phase. We decide on a model for the primary and mass ratio in which energy dissipation due to drag forces can unbind the necessary envelope mass so that the remnant mass $M_{\rm rem}$ matches mass estimates of R4's B[e] supergiant.

In Figure 4.2, we plot the properties of the stellar model which we have selected as the initial condition for the hydrodynamical simulation that we present in this paper. Figure 4.2 shows as a function of the radial (mass) coordinate the binding energy of the envelope, the change in the orbital energy from the start of the inspiral, and the energy dissipated by drag during the dynamical inspiral.

We first note that the change in orbital energy curve (magenta) is above the binding energy curve (purple) at a relatively large outer radius. For radii beyond this crossing point, one can consider the envelope material, which contains a negligible fraction of the total mass, to be easily ejected. This justifies our trimming of the stellar envelope at $R \approx 20\,R_{\odot}$ when mapping into the hydrodynamical simulations. The core and the envelope of the star can then be well-resolved in 3D without prohibitive computational costs. This is also motivated by Podsiadlowski (2001), who note that the secondary's contact with the low-density outer envelope at the onset of mass transfer will produce a frictional luminosity able to unbind stellar material well before the dynamical inspiral begins.

By trimming our envelope, we effectively focus our simulations on the dynamical inspiral phase and consider the envelope material beyond the crossing point to be ejected by the starting point of our simulations. Motivated by this, we consider modifications to the simple energy formalism used in section 4.2.2 that take into account the importance of drag in driving the inspiral. We re-examine our profiles using Bondi-Hoyle-Lyttleton accretion (HLA) theory (Hoyle & Lyttleton 1939) to calculate the energy dissipated due to drag, which is related to the gravitational drag force $F_{\mathrm{d,HL}}$ by

$$\dot{E}_{\mathrm{orb}}(r) = -F_{\mathrm{d,HL}} v_{\infty}(r) \tag{4.2}$$

where v_∞ is the orbital speed of the secondary at a certain radius r, given by

$$v_\infty = f_{\rm kep} v_{\rm kep}. \tag{4.3}$$

Here $f_{\rm kep}$ is a factor describing the secondary's speed relative to the Keplerian velocity. The gravitational drag force is

$$F_{\rm d,HL}(r) = 4\pi G^2 M_2^2 \rho_\infty(r)/v_\infty^2(r) \tag{4.4}$$

where M_2 is the mass of the secondary and ρ_∞ is the density of the primary at that radius. Using this formalism, we integrate $\dot{E}_{\rm orb}$ to find the total energy dissipated from the orbit $\Delta E_{\rm orb}$ along the inspiraling (non-circular) trajectory (peach curves in Figure 4.2). We calculate the mass coordinate and energy where the curve for $\Delta E_{\rm orb}$ rises above the binding energy and take these values to be the mass unbound and energy released by the inspiral for that primary profile and given mass ratio q.

We address these effects in more detail in Section 4.4 but note here that these values provide a reasonable lower limit to the energy injection, as the steep density gradients in the envelope would increase the energy dissipation rate from the one described by $F_{\rm d,HL}$ (MacLeod et al. 2017b; De et al. 2020; Everson et al. 2020).

We also note that the dynamical inspiral will be terminated at an inner radius at which the secondary star would be tidally disrupted by the primary's core,

$$r_{\rm disrupt} = R_2 \left(\frac{2\rho_{\rm enc}}{\rho_2} \right)^{1/3}, \tag{4.5}$$

where $\rho_{\rm enc}$ is the average enclosed density of the primary at $r_{\rm disrupt}$ and R_2 and ρ_2 are the radius and average density of the secondary (Roche 1849). The radius of disruption in Figure 4.2 shows the location where the secondary would begin to lose significant mass and can no longer be treated as a point mass as assumed by the equation of motion used to calculate the inspiral. In fact, we anticipate that at this radius the material of the secondary should begin to stream onto the core of the primary (Ivanova et al. 2002; Ivanova 2002).

In the binary model that we selected for the 3D simulation (Figure 4.2), the HLA drag formalism predicts that enough energy will be dissipated in order to unbind a mass comparable to the mass of the secondary. This is expected to occur at a similar but larger mass coordinate than that at which the secondary would be disrupted by the primary's core, which was one of our key criteria. That is, the inspiral will likely terminate after the secondary dissipates enough energy to unbind the amount of mass needed to match the mass estimates of the B[e] progenitor. Our chosen model for the pre-merger system has a primary mass of $12.9\,M_\odot$, secondary mass ratio $q = 0.4$, and radius of $55\,R_\odot$. Its age is $\approx 10^4$ years younger than the A supergiant model described in Section 4.2. Since we avoid prohibitively high resolution in our 3D hydrodynamics simulation by using only the inner $20 R_\odot$ of the primary profile and representing the secondary with a point mass (Section 4.3.2), our simulation setup has the ability to most closely reproduce an initial condition with smaller primary and secondary sizes. This consideration guided us to select this model, which pairs the smallest allowed values of separation and mass ratio as predicted by the overlap region shown in the bottom panel of Figure 4.1. Note that the methods of this section yield other valid pre-merger models that satisfy these conditions and are within the overlap region of Figure 4.1; in this paper, we present the results of simulating one of these options.

4.3.2 Description of simulation

We map the density, pressure, temperature, and composition of the 1D `MESA` profile onto a 3D grid using `FLASH` (Fryxell et al. 2000) version 4.3, a grid-based adaptive mesh refinement hydrodynamics code. Our setup is adapted from Guillochon & Ramirez-Ruiz (2013), but it uses an extended Helmholtz equation of state (Timmes & Swesty 2000) instead of a polytropic EOS. In addition, we track the composition of elements as described in Law-Smith et al. (2019).

In order to resolve the inspiral near the core while utilizing a reasonable amount of computational resources, we trim the profile to $20\,R_\odot$ for the simulation, which we justify with analytical results presented in Figure 4.2. The computational domain is cubical with volume $(80\,R_\odot)^3$ and is initially composed of an 8^3 block grid with a minimum cell size of $0.019\,R_\odot$.

To setup the initial condition, we initially relax the stellar profile for a few dynamical times. During relaxation, a point mass (constructed to represent the secondary) is placed at $15 R_{\odot}$, initially at rest. The velocity of the secondary is then gradually increased during the relaxation process until it attains an approximate Keplerian velocity as determined by the enclosed mass at $15\,R_{\odot}$. The mass of the secondary is $5.18\,M_{\odot}$, corresponding to $q = 0.4$. Once relaxation ends, the primary model is in hydrostatic equilibrium and the inspiral trajectory is calculated self-consistently. The properties of the merger outcome are found to be rather insensitive to the exact initial conditions of the secondary's velocity, provided it is close to Keplerian. This assumption is justified by the inspiral calculations presented in Section 4.3.1. We stop the simulation once the particle reaches the tidal radius (Equation 4.5). We compare the numerical trajectories with the analytic/HLA drag predictions presented in Section 4.3.1 and find that while both show a dynamical plunge, the secondary in the hydrodynamical simulation inspirals at a slightly faster rate. This is expected to be the case as the HLA drag coefficients are systematically lower than those derived when the stellar density gradients are included, as shown by MacLeod & Ramirez-Ruiz (2015b) and MacLeod et al. (2017b).

4.3.3 Constructing `MESA` Models for the Remnant

To understand the merger remnant in terms of observables, we map our simulation results into `MESA` and allow the resulting profiles to evolve further. Applying the relaxation module to the merger model, we relax the composition,

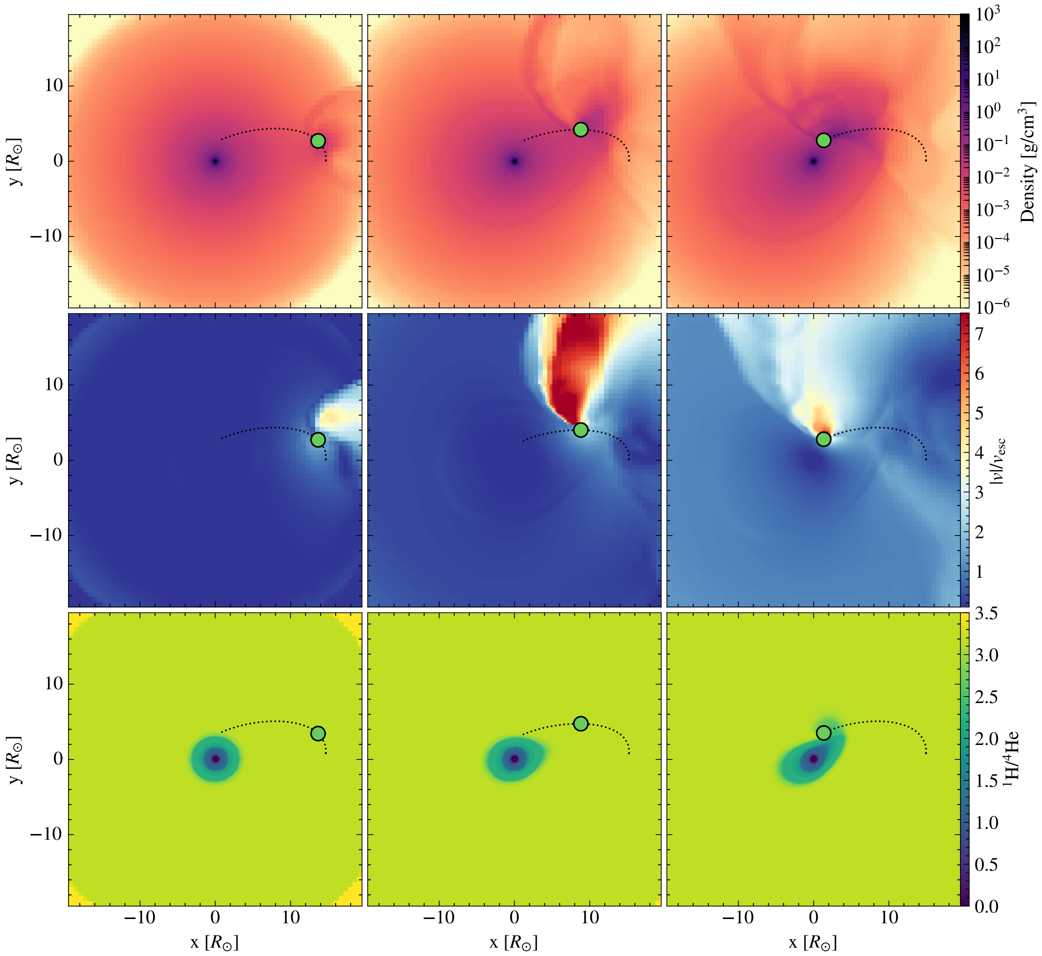

Figure 4.3 2D slices in the xy plane, showing snapshots of the simulation at $t = 14\,t_{\rm dyn}, t = 24\,t_{\rm dyn}$, and $t = t_{\rm disrupt} = 28t_{\rm dyn}$, where $t_{\rm dyn}$ is the core dynamical time and $t_{\rm disrupt}$ is the time when the secondary reaches the tidal disruption radius. Increasing time is read from left to right. *Top:* Density of all material. *Middle:* Velocity magnitude divided by the core escape velocity $v_{\rm esc} \approx 10^8\,{\rm cm/s}$. *Bottom:* Ratio of ^{1}H and ^{4}He mass fractions. The secondary is shown as a green dot and its inspiral is shown by the dotted line. The color of the star is chosen from the colorbar in the bottom panel, based on the secondary's hydrogen-to-helium ratio.

then the entropy, using `MESA`'s `inlist_massive_defaults` along with an inlist specifying parameters for relaxation.

Before importing the 3D simulation results to `MESA`, the material of the bound primary mass has to be combined with the secondary. At the end of the hydrodynamical simulation, the secondary has reached a radius at which it would tidally disrupt due to the gravitational influence of the primary's core ($r_{\rm disrupt}$), causing material and energy to be deposited around that radius. We approximate the tidal disruption of the secondary by adding the mass and chemical composition of the secondary to the bound primary material in the vicinity of the tidal disruption radius. Using a `MESA` model of a $5.18 M_\odot$ main sequence star to determine the secondary's chemical and thermal profile, we distribute the mass of the secondary across the outer mass shells of the bound primary material such that the greatest amount of mass is added around the mass coordinate of $r_{\rm disrupt}$, with the remaining mass added in a tail skewing towards larger radius. This in turn determines the distribution of the combined chemical and thermal structure. We then sort the shells of the combined remnant profile by entropy, such that entropy increases with radius (Lombardi et al. 2002).

We map this remnant into the 1D stellar evolution code `MESA`. This entails making a `MESA` model of a star whose total mass is equal to the sum of the bound primary mass and the secondary mass, as well as having chemical and thermal structure that matches that of the combined merger remnant. Using the methods outlined in Schneider et al. (2016, 2019, 2020), we achieve a 1D

`MESA` model with a structure that is a close match to that of the combined merger remnant described above.

To account for the deposition of energy from the disruption of the secondary, we add heat to the remnant during the `MESA` evolution. A total energy equal to the binding energy of the secondary is injected into the remnant during evolution at shells in the vicinity of $r_{\rm disrupt}$. This is certainly a lower limit to the amount of energy injected into the remnant, as we must also consider the secondary's remaining orbital energy. However, it is not clear what proportion of the remaining orbital energy is dissipated into the remnant rather than being used to spin off the envelope of the primary once the secondary is tidally disrupted. A detailed understanding of this requires 3D hydrodynamical simulations of this stage that resolve both objects in order to determine the resultant energy dissipation and rotational profiles. For simplicity, here we take the conservative approach of only adding the binding energy. Each shell receives the same heat per unit mass at a constant rate $\approx E_{\rm bind} \times 10^{-7}{\rm s}^{-1}$ until energy equal to the binding energy has accumulated, at ≈ 6 years. This is much shorter than the total time over which the remnant is evolved ($\gtrsim 10^5$ years).

We evolve the resulting relaxed combined model in `MESA` using `inlist_massive_defaults` along with a base inlist for evolution until the end of helium burning.

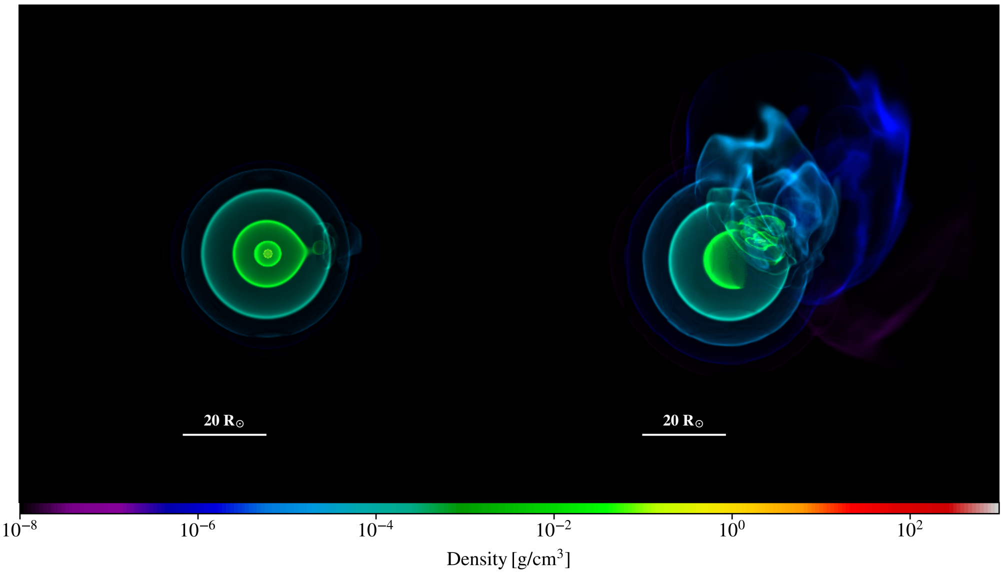

Figure 4.4 *Left Panel:* 3D rendering of density of all material in the 3D hydrodynamical simulation, shown at $t = 14t_{\rm dyn}$. The diameter of material depicted is $40R_\odot$ across. *Right Panel:* 3D rendering of density of only unbound material at $t = t_{\rm disrupt}$.

4.4 Hydrodynamical Simulation

In this section we present the results of our `FLASH` simulation modeling the merger of a binary chosen in Section 4.3.1 to represent the progenitor of R4's B[e] supergiant. In our simulation, the initial mass of the primary model is $13\,M_\odot$ and has a companion-to-primary mass ratio of $q = 0.4$, corresponding to a secondary with mass $5.18\,M_\odot$. The primary star's initial radius before trimming is $55\,R_\odot$; after being trimmed to $20\,R_\odot$, the pre-merger primary mass is $12.7\,M_\odot$. In addition to the simulation presented here, we ran simulations with different initial conditions that also met the requirements outlined in Sections 4.2 and 4.3.1. We find the results presented here to be representative, as only minor differences are observed.

4.4.1 Dynamical Inspiral

As the inspiral progresses over time (left to right in the top 3 panels of Figure 4.3), the secondary rapidly plunges into the core of the primary via dynamical inspiral. We expected this steep plunge-in from our initial conditions, as we placed the secondary deep in the envelope of the primary where the inspiral would be driven by strong drag forces.

In Section 4.3.1 we narrowed down our profiles using HLA drag theory to predict the amount of unbound mass and released energy, but the results of such an approach are thought to serve as a rough estimate for these values. In practice, the initial conditions of the simulation push the limits of the power that HLA drag theory possesses to predict the path of our expected inspiral, since HLA is predicated on the assumption that the inspiral deviates only mildly from a Keplerian orbit throughout. In a steep spiral-in the trajectory is far from Keplerian, as we see in the progression of the inspiral for the 55 $R_\odot$ profile in Figure 4.3.

However, based on the ideas of MacLeod et al. (2017b), the steep density gradient of the primary's envelope and the high q value indicate that the effects of drag can be approximated by multiplying the drag force $F_{\mathrm{d,HL}}$ by a constant coefficient C_d, applied only in the tangential direction and opposing the direction of motion. To guide our understanding of how these factors steepened the inspiral, we calculate an average C_d by comparing the timescale of the inspiral with the ratio of the change in orbital energy, ΔE, and the rate of energy dissipation by gravitational drag, $\dot{E}$. We use the following relation

$$C_d = \Delta E_{\rm orb}/(F_{\rm d,HL} v_2 t_{\rm orb}) \tag{4.6}$$

with the average values of density and velocity for $r_{\rm disrupt} < R < 20\,R_\odot$ and the change in orbital energy from $R = 20\,R_\odot$ to $R = r_{\rm disrupt}$, and we find an average $C_d = 2.6$. Here $r_{\rm disrupt}$ is the tidal disruption radius as in Equation 4.5 (see section 4.4.2 for value). Thus on average, the drag force is a factor of 2.6 higher than the HLA prediction, which is in agreement with the results of MacLeod et al. (2017b). A higher drag force implies that we would expect the orbital energy to be dissipated at a smaller mass coordinate and the inspiral to proceed more rapidly than the one predicted by HLA. This aligns with the results of our simulation, which tends to unbind slightly more mass and has a steeper inspiral trajectory than that predicted in Section 4.3.1. In addition, the change in orbital energy deviates from that commonly assumed by the α formalism, which assumes circular orbits. As Figure 4.2 shows, the change in orbital energy due to drag dissipation (peach) rises above the binding energy curve (purple) at different mass coordinates than the difference in orbital energy calculated under the assumptions of the α formalism (magenta).

4.4.2 End of Inspiral

The simulation is evolved until the point mass representing the secondary reaches the disruption radius, at $3.85\,R_\odot$. In the bottom three panels of Figure

4.3, we see that as the inspiral proceeds (left to right), the core of the primary becomes distorted and even partially disrupted once the secondary reaches its own tidal disruption radius. At this stage, $\approx 4.6\,M_\odot$ of mass is unbound. Our calculations of the initial conditions predicted that the secondary would unbind $\approx 5\,M_\odot$ by the time the engulfed star reached its tidal disruption radius for both primaries, which agrees well with the total amount of mass found to be ejected in our simulation. We also note that $\lesssim 8\%$ of the original primary mass or $\lesssim 1\,M_\odot$ has left the simulation box over the duration of the simulation.

4.4.3 Remnant and Nebula

Once the secondary has reached the tidal disruption radius, we treat the merger remnant as composed of material from the disrupted secondary and the bound mass of the primary. At this point in the simulation, $8.3\,M_\odot$ of primary material remains bound. The bottom right panel of Figure 4.3 shows the ratio of ^{1}H to ^{4}He mass fractions at the end of the simulation for both the primary and secondary. The composition of the bound remnant will be mixed in the outer layers with the different composition of the secondary.

The nebula produced by the merger will consist of unbound material whose velocity is greater than the escape velocity of the core of the primary star. In the middle three panels of Figure 4.3, we plot the velocity magnitude divided by the escape velocity of the core throughout the simulation. As the inspiral progresses (left to right), more material reaches large enough velocities to be able to escape. The plunge-in of the secondary up to the tidal disruption radius highly disturbs the envelope material and causes an asymmetric ejection of unbound material; the 3D renderings in Figure 4.4 depict how the primary star's envelope is affected at $t = 14t_{\rm dyn}$ and $t = 28t_{\rm dyn}$. Although the material in the path of the inspiral is preferentially accelerated along the path of least resistance, a significant fraction of material at a radial distance $\gtrsim 5R_\odot$ becomes unbound in all directions by the time the secondary reaches the tidal disruption radius.

The total kinetic energy of the unbound material is 3.2×10^{50} ergs and its average velocity is 1.7×10^8 cm/s, which is $1.8\,v_{\rm esc}$ (the core's escape velocity). As shown in the center-right panel of Figure 4.3, the majority of the unbound material moves initially at speeds that are in excess of those observed in R4's nebula, which exhibits velocities of $\approx 10^7$ cm/s. As the ejected nebula material expands, it will sweep up the surrounding material and, as a result, it will decelerate. The displaced volume as derived from the size of the observed nebula implies that the ejected material will sweep a mass that is larger than its own ($\approx 4 - 5\,M_\odot$) and thus is expected to decelerate significantly.

The morphology of the unbound material in the simulations once the secondary has reached the disruption radius provides us with a qualitative picture for the shape of the nebula resulting from the merger. The 3D rendering in the right panel of Figure 4.4 of the density of unbound material forms an asymmetric bipolar structure. Pasquali et al. (2000) conclude from kinematics that R4's nebula also is not strictly bipolar. However, R4's nebula clearly has a complicated structure and resolving its morphology requires higher-resolution

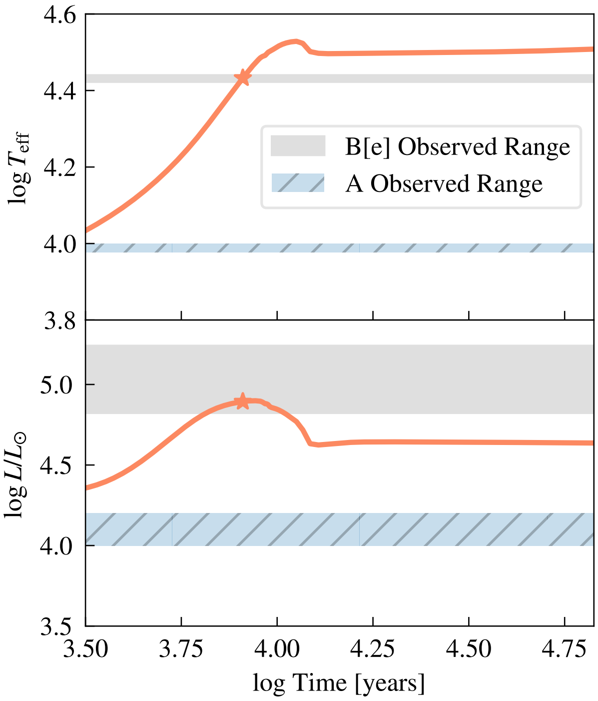

Figure 4.5 Evolution of the temperature and luminosity of the merger remnant in `MESA`. Here time is measured in years since the merger. The grey bar shows the range of $T_{\rm eff}$ and L observed for the B[e] component. The remnant remains hotter and more luminous than the observed A component (blue hatched bar) throughout the cooling period, the duration of which is also in agreement with the age of the remnant as derived by the age of the nebula. The star symbol denotes the model for the merger remnant described in Section 4.5 that best exhibits the observed properties.

observations. In addition, any detailed comparison of the merger ejecta with simulations will need long-term modelling of the ejecta's expansion including interactions with the ISM and the stellar winds, and the illumination from the merger remnant.

4.5 Long Term Evolution

Figure 4.5 shows the track of the remnant's evolution in effective temperature and luminosity over time. Zickgraf et al. (1996) determined the effective temperature and luminosity of the B[e] star by taking their best fits to the effective temperature $T_{\rm eff}$ and $\log g$ values, then calculating the bolometric luminosity using the radius they found from $\log g$ and their spectroscopic mass with $\sin i \approx 1$. From Figure 8 of Zickgraf et al. (1996), we deduce approximate error bars of $T_{\rm eff} = 27000\,{\rm K} \pm 500\,{\rm K}$ and $\log g = 3.2 \pm 0.175$ (mean values correspond to those cited in Section 4.2.1 for the B[e] star). We also deduce a bolometric luminosity $L = 10^{4.95}\,L_\odot$ from Figure 10 of Zickgraf et al. (1996) and derive error bars on the luminosity measurement from those on $T_{\rm eff}$ and $\log g$. The 1σ ranges for $T_{\rm eff}$ and L are shown in grey in Figure 4.5.

We cite values for the evolution of the merger remnant from the $55\,R_\odot$ simulation here. The remnant attains $T_{\rm eff} = 27000\,{\rm K}$ at 8.14×10^3 years (Figure 4.5, top panel). This model (star symbol in Figure 4.5) has $\log g = 3.34$, corresponding to a mass of $12.9\,M_\odot$ and radius $12.73\,R_\odot$.

The $T_{\rm eff}$, $\log g$, and mass values are within the errors for the observed values, and the radii resulting from these values are close to the radius $14\,R_\odot$ derived from the observed values of Zickgraf et al. (1996). The luminosity is $L = 10^{4.9}\,L_\odot$ (Figure 4.5, bottom panel), again very near the derived value of Zickgraf et al. (1996).

Our long-term evolution of the merger remnant produces a model which achieves the same effective temperature, luminosity, radius, and mass as the observed B[e] supergiant. This model exhibits all the observed characteristics at 8×10^3 years post-merger. We compare in Figure 4.5 the evolution of the merger remnant to the observed properties of star A (blue hatched region), which has a similar mass but has solely undergone single-star evolution. The evolution of the merger remnant starts to deviate from the evolution of star A soon after the merger, as large amounts of heat are injected deep into its interior that must be radiated away. This allows the merger remnant to remain extremely luminous for a cooling phase of about 10^5 years.

Since in this scenario we expect the nebula to be the result of ejected material from the merger, we take the age of the remnant to be equal to the age of the nebula, which is derived from the observed expansion velocity and nebula size to be $\sim 10^4$ years. Thus our model is able to successfully reproduce the observed properties of the B[e] supergiant at the expected age of the remnant. Our evolved merger remnant therefore constitutes a viable model for the B[e] supergiant of the R4 system.

It is important to note that the late-time evolution ($t \gtrsim 10^5$ years) of our merger remnant is sensitive to our mixing prescription and whether we include rotation. Details of how the merger remnant may evolve on the HR diagram after the cooling period will be explored in future work.

Ultimately, achieving our goal of studying the long-term evolution of the remnant depended on our ability to map our merger remnant from the 3D hydrodynamical code `FLASH` into `MESA`, a 1D stellar evolution code. Bridging this gap allowed us to make more concrete statements about how applicable our merger models truly are to a particular system. Furthermore, we were able to treat the long-term evolution as a natural continuation of the merger process for the system by mapping the final conditions of the 3D simulation onto the initial conditions of the 1D simulation. The combination of our highly resolved hydrodynamical simulations with the stellar evolution code allowed us to investigate various stages of the merger that proceed on widely different timescales, all of which are needed in order to accurately compute the evolution of systems hosting multiple interacting stars.

4.6 Summary and Conclusions

We have studied the evolutionary history of the R4 system using 3D hydrodynamical simulations and a 1D stellar evolution code to model its B[e] supergiant. We chose this system because it has been postulated that a binary stellar merger produced the B[e] supergiant. Furthermore, the R4 system was especially conducive to the study of binary stellar mergers since the observations provided enough constraints on the properties of the system to develop sensible initial conditions (Section 4.2). Observations of the nebula size and expansion velocity limited the age of the nebula, which is a proxy for the time since merger. We also appealed to the large observed separation between the stars in the R4 system to deduce that the A supergiant companion evolved independently, and to the observed luminosity of the B[e] star to set a lower limit on the amount of energy injected into the merger.

Using initial conditions driven by the observed properties of the R4 system, we have simulated a binary stellar merger using a 3D hydrodynamics code and mapped the merger remnant into a 1D stellar evolution code to study its long-term evolution. As a result, we were able to compare the R4 system to the remnant at a time since merger that matches the nebula age. We find that our methods produce a model for the merger remnant at the appropriate time whose stellar properties are in good agreement with the B[e] supergiant. The long-term evolution also suggests that the remnant is still undergoing a cooling phase after the merger, during which period it remains extremely luminous and attains the paradoxically high effective temperature and luminosity of the B[e] supergiant.

Even with the observational constraints, some degeneracy remains in the choice of progenitor masses and separations (Section 4.2.2). We have chosen to simulate a particular combination that satisfies the initial conditions outlined in Section 4.2. The success of the exercise applied to this choice serves as a proof-of-concept for the methods laid out in this paper to study similar problems by transitioning between `FLASH` and `MESA`. In particular, the dynamical inspiral of the merger process was consistently extended to the long-term evolution of the remnant. The process may be applied to different progenitors and different systems to generate models of a variety of merger remnants, which, as thoughtfully argued by Sana et al. (2012), are expected to be common.

Note that the `MESA` models for the merger remnant were evolved without rotation. During the plunging of the companion, a significant fraction of the orbital angular momentum is transferred to the unbound envelope material in our simulations. At the time the companion reaches the tidal disruption radius, it has a sub-Keplerian velocity $v \approx 0.6\,v_{\rm kep}$. The companion will be disrupted at this stage and its orbital angular momentum is expected to be effectively transferred to the merger remnant. Assuming that the secondary's angular momentum is distributed uniformly over the remnant, we can calculate the remnant's final rotation velocity. The angular velocity that the remnant gains from merging with the secondary is given by $\Delta\Omega = \frac{\Delta J}{I}$, where $I = \frac{2}{5}(M_{\rm bound} + M_2)R^2$ is the moment of inertia of the remnant. Here $\Delta J = f_{\rm kep} M_2 \sqrt{G M_{\rm bound} R}$ is the additional angular momentum of the secondary, where the orbital speed of the secondary is measured relative to the Keplerian velocity as in Equation 4.3. Evaluating this at the tidal disruption radius we find $f_{\rm kep} = 0.6$, which implies that the addition of the angular momentum of the secondary is expected to spin up the merger remnant to $\approx 36\%$ of its breakup velocity. In our parameter space of initial conditions, there are some initial conditions that would give the final merger product even higher rotation as the final ratio of M_2 to $M_{\rm bound}$ could be closer to unity. Although in principle this rotation would serve as another reservoir of energy for the remnant to draw upon, more detailed study of the angular momentum transport throughout the remnant is required to robustly estimate its dissipation rate. Here we take the simplest approach of not including rotation in our `MESA` model, which will provide a lower limit to the luminosity of the merger product over its thermal timescale.

In addition to a more careful treatment of rotation in our remnant, we envision many other avenues for extending our work in the future. It would be useful to investigate the details of how late-term evolution of the merger remnant, after the thermal relaxation period is over, will proceed. In particular, the effects of different mixing prescriptions and of the ensuing rotational profile of the remnant ought to be better quantified. Furthermore, while in this work the secondary was modeled as a point mass, endeavors to model both primary and secondary using realistic stellar profiles from `MESA` are already underway. This would allow the 3D hydrodynamical simulation to realistically follow the inspiral all the way to merger instead of stopping at the secondary's tidal disruption radius. A simulation using realistic profiles would moreover resolve how the material of the secondary streams on to the core of the primary. This would provide a more accurate model for the size and shape of the merger remnant and would also narrow the uncertainty in the mixing prescription used to map the remnant into `MESA`.

To conclude, the proposed numerical formalism may be applied to model the outcomes of mergers, collisions, and tidal disruptions (Law-Smith et al. 2019, 2020b). On the timescale of the study, we could only hope to explore in detail merely some subset of the interesting possible encounters that could have given rise to the R4 system (Figure 4.1). In the near future, we hope to develop a comprehensive model database of remnants and their predicted observational outcomes for a range of events. Such a formalism would serve as a valuable theoretical counterpart to the increasing number of merger remnant products expected to be uncovered in future observational surveys (Sana et al. 2013b; Almeida et al. 2017; Mahy et al. 2020).

4.7 Software Utilized

`MESA` (Paxton et al. 2011, 2013, 2015, 2018), `FLASH` (Fryxell et al. 2000), `matplotlib` (Hunter 2007), `yt` (Turk et al. 2011), `NumPy` (van der Walt et al. 2011).

Chapter 5

Rethinking Thorne-Żytkow Object Formation: Assembly via Common Envelope in Field Binaries

Abstract

Thorne-Żytkow objects (TŻOs), hypothetical merger products in which a neutron star is embedded in a stellar core, are traditionally considered steady-state configurations. Their assembly, especially through dynamical channels, is not well-understood. The predominant focus in the literature has been the observational signatures related to the long-term fate and evolution of TŻOs, with their initial formation often treated as a given. However, the foundational calculations supporting the existence of TŻOs assume non-rotating spherically-symmetric initial conditions that are inconsistent with a merger scenario. In this work, we explore the implications of post-merger dynamics in TŻO formation scenarios with field binary progenitors, specifically the role that angular momentum transport during the common envelope phase plays in constraining possible merger products, using the tools of stellar evolution and three-dimensional hydrodynamics. We also propose an alternative steady-state outcome for these mergers: the thin-envelope TŻO. These configurations may be of interest to upcoming time-domain surveys as potential X-ray sources that may be preceded by a series of bright transient events.

5.1 Introduction

The study of interacting binaries seeks to understand how the products of multiple stellar evolution differ from those expected from single stellar evolution. To do this, it is necessary to constrain the formation channels of many types of remnant systems, including exotic or unusual merger products. Stellar mergers can result in a range of transients, such as gamma-ray bursts and luminous fast blue optical transients (Metzger & Perley 2023), as well as unusual stars, such as the too-bright B[e] supergiant of R4 in the SMC (Wu et al. 2020) and the hypothetical Thorne-Żytkow object (TŻO; Thorne & Żytkow 1975, 1977).

A classical TŻO is described as an exotic astrophysical object that may appear to be an extended post-main sequence star, but is in fact an accretion-powered stellar merger product with a neutron star (NS) at its core (Thorne & Żytkow 1975, 1977), or alternatively, for TŻOs with mass greater than $12 - 16\ M_\odot$, the envelope may be supported by nuclear burning rather than accretion (Eich et al. 1989; Biehle 1991; Cannon et al. 1992; Cannon 1993). Though the existence of TŻOs is controversial, a few observations tentatively support the possibility (see, e.g., Levesque et al. 2014; O'Grady et al. 2023). However, the preliminary conclusions of these observations have incurred numerous rebuttals (Tout et al. 2014; Maccarone & de Mink 2016; Beasor et al. 2018; O'Grady et al. 2020). For a recent review, see Liu & Zhang (2022).

There are thought to be several potential pathways for TŻO formation: merging of a field (i.e., isolated) binary composed of a post-main sequence star and compact object (CO) through a common envelope (CE) phase (Taam et al. 1978; Terman et al. 1995; Ghosh et al. 1997; Ablimit et al. 2022), direct impact of a NS with its companion due to a kick (Leonard et al. 1994; Hirai & Podsiadlowski 2022), or dynamical merger within a triple system or stellar cluster (Ray et al. 1987; Eisner et al. 2022). The rates of the latter two channels are much lower than the first (Podsiadlowski et al. 1995), therefore the CE channel in field binaries is the focus of this work. Though it has been suggested that TŻO formation via CE is unlikely due to the formation of jets launched by the NS as it inspirals through the stellar envelope (Chevalier 1993; Papish et al. 2015), detailed hydrodynamic simulations by MacLeod & Ramirez-Ruiz (2015a) demonstrate that accretion onto NSs may become very inefficient when a density gradient is present during the CE phase, precluding jet formation during inspiral.

Historically, much theoretical effort has gone toward describing the evolution and fate of TŻOs while tending to avoid modeling their formation altogether (see, e.g., Thorne & Żytkow 1977; Biehle 1991; Cannon et al. 1992; Farmer et al. 2023) except through population synthesis (Podsiadlowski et al. 1995; Hutilukejiang et al. 2018; Ablimit et al. 2022). The foundational calculations that supported the existence of TŻOs carried the assumption of a non-rotating, spherically symmetric configuration (e.g., Thorne & Żytkow 1977; Biehle 1991). In the case of formation via a CE channel, rotation cannot be ignored as the angular momentum content of the material surrounding the NS has serious implications about how accretion will take place and the impact of the type of accretion on the structure of the merger product (see discussions in Sections 5.2.2 and 5.3). It is widely accepted that accretion disk formation spells the end to a TŻO (Podsiadlowski et al. 1995) due to feedback, underscoring the importance of understanding when disk formation occurs (Murguia-Berthier et al. 2020) in regards to the lifetime and overall stability of TŻOs.

A companion paper to this work (Hutchinson-Smith et al. 2023) uses 3D hydrodynamic simulations to model TŻO formation, providing new insights into how formation occurs as well as key factors that impact merger outcomes. Hutchinson-Smith et al. (2023) model the future merger of the X-ray binary LMC X-4 (Lang et al. 1981) as an ideal TŻO progenitor, exploring the effects of merger dynamics on angular momentum content, accretion rate, and energetics. The impact of angular momentum deposition via orbital decay on the stability of the accretion powered "core" suggests further study on the constraints of T$\dot{Z}$O formation via CE altogether, which we present here.

In this paper we aim to discover the binary conditions under which the inspiraling CO, upon merging with the core, can subsequently accrete without forming a disk and, as a result, avoid generating feedback (e.g., Lee & Ramirez-Ruiz 2006; Zalamea & Beloborodov 2009; Perna et al. 2014; Murguia-Berthier et al. 2020) that would prevent the formation of a classical T$\dot{Z}$O. However, if the feedback from the accreting CO is significant, as shown by Hutchinson-Smith et al. (2023), a classical T$\dot{Z}$O is precluded, and the merger is likely to be followed by a bright transient whose properties may depend sensitively on the orientation of the observer with respect to the plane of the merging binary. In the latter case, we expect a significant fraction of the envelope to be ejected, thus challenging one of the most commonly invoked avenues for T$\dot{Z}$O formation.

The paper is structured as follows. In Section 5.2, we explore the merger pathways of field binaries that are traditionally invoked for T$\dot{Z}$O assembly and the implied outcomes of these pathways, based on angular momentum conservation. In Section 5.3, we analyze a broad parameter space of binary merger scenarios to identify the most optimistic regime for the formation of T$\dot{Z}$Os or similar astrophysical objects. Section 5.4 presents an alternative to supersede T$\dot{Z}$Os as a distinguishable transient merger product. We summarize our findings in Section 5.5.

5.2 Merger Pathways

We can understand the potential formation pathways of TŻOs and related merger products through the global properties of their respective progenitor systems. Though field binaries are not the only potential TŻO progenitors, the following analysis applies only to field binaries comprised of a compact object, i.e. neutron star (NS) or stellar-mass black hole (BH), and a star which are close enough to interact during the evolution of the stellar companion.

5.2.1 Common Envelope Evolution

In field binaries, the onset of an interaction begins when a stellar companion (hereafter referred to as the "primary") reaches the end of its life and begins to expand. The stellar envelope increases in radius until its companion (hereafter referred to as the "secondary") begins to accrete envelope material. A common envelope (CE) interaction occurs when this accretion becomes dynamically unstable and the secondary is engulfed by the envelope of the primary.

A CE configuration is a precursor to all merger scenarios, though it can also function as a mechanism for orbital tightening (i.e., hardening) in cases where the envelope is ejected and a short period binary is formed. In order to define the parameter space in which we expect TŻOs to form, we must exclude scenarios in which the envelope is ejected during CE. Typically, a simple energy formalism, i.e. the α-formalism (van den Heuvel 1976; Webbink 1984), is used to discern when ejection is likely.

The α-formalism compares the orbital energy $\Delta E_{\rm orb}$ deposited into the envelope by the secondary to the gravitational binding energy $E_{\rm bind}$ of the envelope. We define $\Delta E_{\rm orb}$ as

$$\Delta E_{\rm orb} = \frac{GM_* M_{\rm CO}}{2a_{\rm initial}} - \frac{GM_{\rm enc} M_{\rm CO}}{2a_{\rm final}}, \tag{5.1}$$

in which G is the gravitational constant, $a_{\rm initial}$ and $a_{\rm final}$ are the initial and final separation, respectively, M_* is the total mass of the extended primary star, $M_{\rm CO}$ is the mass of the embedded compact object, and $M_{\rm enc}$ is the enclosed mass of the primary at $a_{\rm final}$. As our interest is in merging systems, we set $a_{\rm final}$ to the radius of the primary's core $R_{\rm core}$. We then define the gravitational binding energy of the envelope as

$$E_{\rm bind} = \int_{M_{\rm core}}^{M_*} -\frac{GM(r)}{r} dm, \tag{5.2}$$

in which $M_{\rm core}$ is the mass of the core of the primary and $M(r)$ is the enclosed primary mass within the radius r.

Roughly, if $\alpha \Delta E_{\rm orb} \geq E_{\rm bind}$, then CE ejection is said to be successful. It is understood that various factors impact the efficiency of the orbital energy in contributing to envelope ejection and that other possible energy reservoirs may play a role; all of these considerations are combined in the efficiency term α. Depending on the characteristics of the system, this term has been shown to have a possible range as broad as $0.01 - 10$ (Zorotovic et al. 2010). Typical values are below unity, but to give a conservative estimate for the number of mergers we assume the transfer of orbital energy to be perfectly efficient with $\alpha = 1$.

In Figure 5.1 we show the various outcomes for a broad range of CE interactions between a typical compact object and post-main sequence stellar companion according to this energy formalism. The compact object masses chosen correspond to the peak distribution masses of NSs and stellar-mass BHs as obtained by the COMPAS[2] binary population synthesis code (Stevenson et al. 2017; Vigna-Gómez et al. 2018; Team COMPAS: Riley et al. 2022). We include systems with BHs here to illustrate the differences between merger products with disrupted and non-disrupted cores (Section 5.2.2), and to approach merger outcomes agnostically. To integrate the binding energy, we utilize a library of stellar models generated with `MESA` v22.05.1[3] (Paxton et al. 2011, 2013, 2015, 2018, 2019) with initial mass $5 - 40\,M_{\odot}$ at solar metallicity ($Z = 0.02$) from the end of the main sequence to the maximum radius reached during the giant branch.

The three outcomes denoted by colored regions in Figure 5.1 are CE ejection, merger with core disruption, and merger with core intact. The ejection scenarios must be excluded from further analysis as they do not represent TŻO progenitors, while the merger scenarios are explored further. We discuss the

---

[2] Publicly available via the GitHub repository.

[3] Results were compared to the same analysis using `MESA` v23.05.1 (Jermyn et al. 2023) with no qualitative differences.

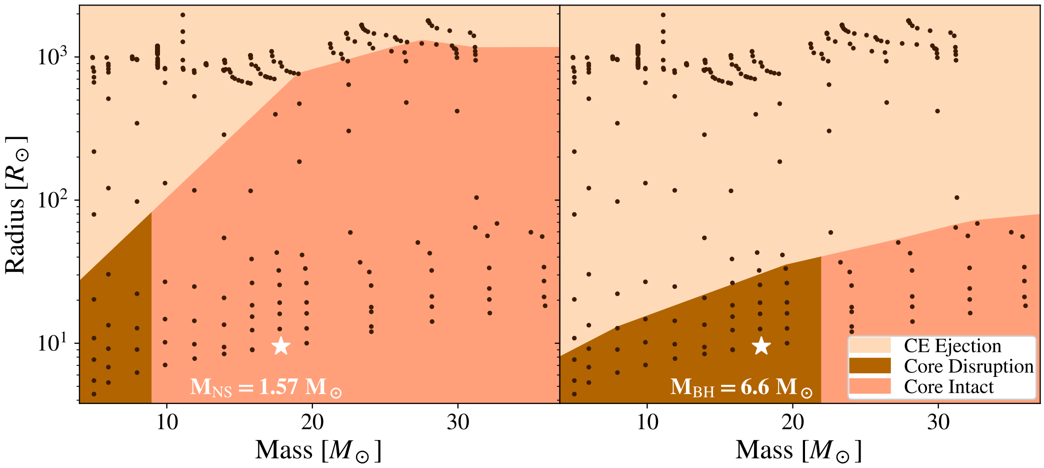

Figure 5.1 Outcomes of common envelope interactions between `MESA` models of 5-40 $M_\odot$ at solar metallicity and a typical NS (left panel) and stellar-mass BH (right panel). The `MESA` models (black dots) evolve from the terminal-age main sequence to the tip of the giant branch, with radius as a proxy for evolutionary state. The stellar model used in the 3D merger simulations included in this work and Hutchinson-Smith et al. (2023) is indicated by the white star. Colored regions denote whether the interaction results in successful CE ejection (beige), merger with core disruption (brown), or merger with core intact (coral).

rationale for dividing the merger scenarios in the following section in accordance with Equations 5.4 and 5.5. We proceed to show that the assumption that any merger between a NS and stellar companion will lead to a classical TŻO is unfounded, and ignores the impact of angular momentum deposition on the accretion that should power the TŻO.

5.2.2 Comparison of Disruptive and Non-Disruptive Merger

To begin to understand the impact of angular momentum deposition on TŻO formation, we first focus on how the angular momentum carried by the compact object impacts the core of the primary. There are clear differences in structure between a disrupted (e.g., Zhang & Fryer 2001; Law-Smith et al.

2020a) and non-disrupted core (e.g, Hutchinson-Smith et al. 2023), the implications of which we explore here.

Every field binary merger will spin up both the envelope material and the core of the primary (see, e.g., Schneider et al. 2019). Due to shocks generated from the inspiral of the compact object, the envelope will absorb most of the orbital angular momentum, but some will be deposited in the core upon merger.

In Figure 5.2, we demonstrate the impact on core structure of a disruptive and non-disruptive merger by comparing the results of two representative 3D hydrodynamical simulations using the setup described in Hutchinson-Smith et al. (2023), adapted from Wu et al. (2020) and Law-Smith et al. (2020a). Using the `FLASH` adaptive mesh refinement hydrodynamics code (Fryxell et al. 2000), we map the non-rotating `MESA` profile of a star of initial mass 18 $M_\odot$ at 9.5 $R_\odot$ as it leaves the main sequence, resolving the core, and introduce a point-mass compact object moving at Keplerian velocity at the limb which proceeds to plunge inward due to drag, shock-heating the envelope. Figure 5.2 provides a zoomed-in view of the stellar core near the end of the compact object inspiral. Top panels show the case of a typical BH of mass 6.6 $M_\odot$ and bottom panels show the case of a typical NS of mass 1.57 $M_\odot$ when the compact object is approximately 0.5 $R_\odot$ from the tidal radius $R_{\rm tidal}$ (left) and when the compact object reaches $0.5R_{\rm tidal}$ (right), defined as follows:

$$R_{\rm tidal} \approx \left(\frac{M_{\rm CO}}{M_{\rm core}}\right)^{1/3} R_{\rm core}, \tag{5.3}$$

in which M_{CO} is the mass of the compact object and M_{core} and R_{core} are the mass and radius of the core, respectively. The global parameters of these simulations are indicated by white stars in both panels of Figure 5.1.

Though classical TŻOs are powered only by NSs, we introduce a BH here in order to give a one-to-one comparison of the core structure of the same primary star at the same stage of evolution in both the disrupted and non-disrupted case. Utilizing a secondary with a larger mass allows us to test both cases controlling for all other factors.

Though both cores are initially deformed by the incoming compact object, the strong shocks created by the BH completely disrupt the core while the weaker shocks of the NS allow the highest density material to remain centrally concentrated. Both cores are spun up through this process, but as long as the spin is lower than that required to form a disk, we can assume quasi-spherical accretion that is requisite to power a classical TŻO.

An accounting of the angular momentum budget as the compact object merges with the core may provide us with a parameter space of progenitor systems in which quasi-spherical accretion is possible.

Disruptive Merger

In cases in which an inspiraling compact object will disrupt the core of its stellar companion prior to merging with it, an accretion disk will be formed.

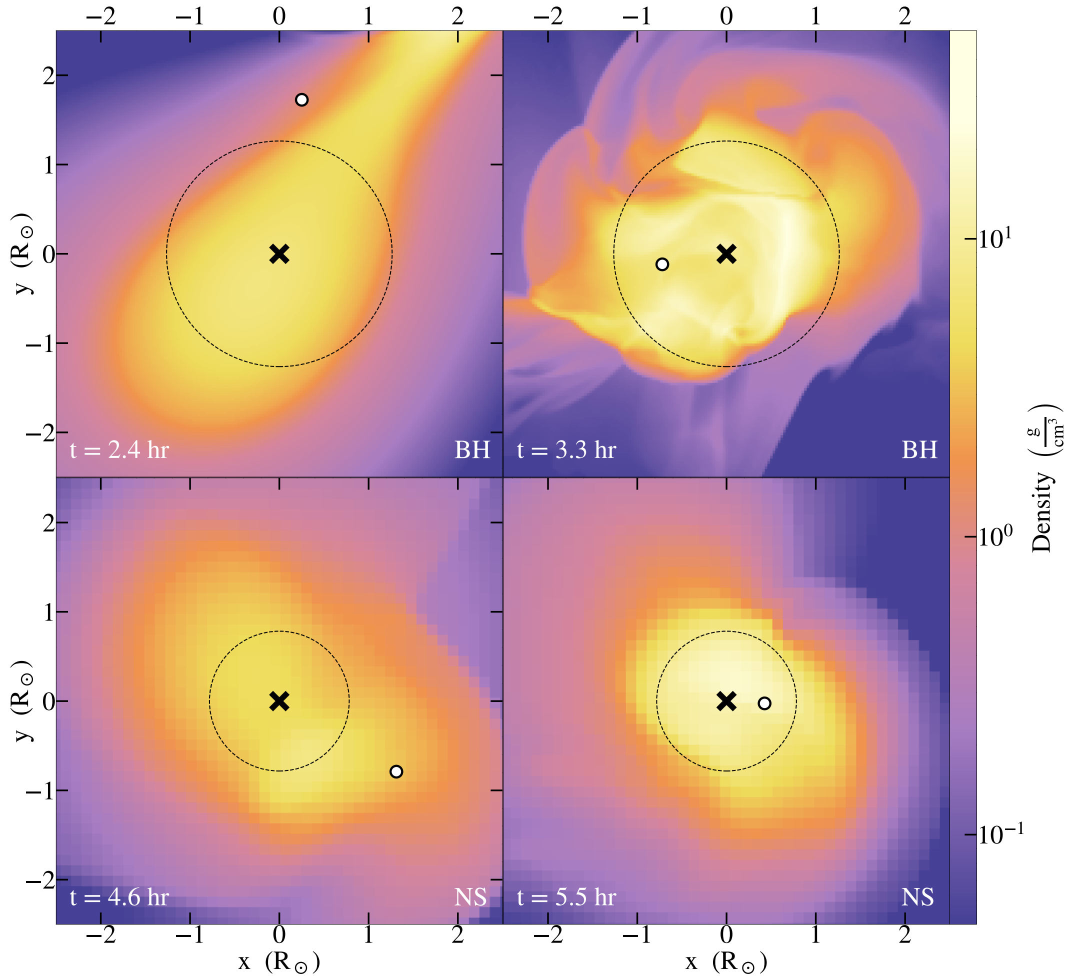

Figure 5.2 Comparison of simulated merger between 18 $M_\odot$ stellar model with 6.6 $M_\odot$ BH ($q_c \approx 3/2$, top panels) and 1.57 $M_\odot$ NS ($q_c \approx 1/3$, bottom panels, adapted from Hutchinson-Smith et al. 2023). The black cross indicates the center of mass of the primary, the white circle with black outline indicates the position of the inspiraling compact object, and the black dashed circle indicates the tidal radius. In the top panels, note that the core (yellow to orange) is deformed as the BH approaches the tidal radius, and is then fully disrupted, indicated by the distribution of shock-heated material surrounding the center of mass. In the bottom panels, we still see deformation to a lesser degree, with the highest density material remaining centrally concentrated.

When the tidal radius is greater than the size of the stellar core,

$$\frac{R_{\rm tidal}}{R_{\rm core}} \approx \left(\frac{M_{\rm CO}}{M_{\rm core}}\right)^{1/3} > 1, \tag{5.4}$$

causing material to be dynamically stripped from the core and ejected by tidal torques through the outer Lagrange points, transporting angular momentum and forming an extended centrifugally supported structure.

Here, we define the mass ratio between the compact object and the core of the companion as

$$q_c := \frac{M_{\rm CO}}{M_{\rm core}}, \tag{5.5}$$

giving the criterion that for a disruptive merger, $q_c > 1$, which defines the vertical boundary between the "Core Disruption" and "Core Intact" regions of Figure 5.1. An accretion disk is guaranteed in this case, precluding classical TŻO formation.

Therefore we limit our remaining analysis to systems in which $q_c < 1$, as shown in the "Core Intact" regions of Figure 5.1.

Non-disruptive Merger

For typical TŻO progenitor systems, which is to say primaries partnered with NSs, excluding those which are likely to lead to envelope ejection or core disruption, q_c values remain fairly constant. In Figure 5.3, we map the q_c values over the relevant parameter space interpolated from the `MESA` library. Evolutionary tracks proceed from bottom to top as radius increases, and slightly from right to left due to wind-driven mass loss. Recalling that NS accretion during inspiral is very minimal (MacLeod & Ramirez-Ruiz 2015b,a; Hutchinson-Smith et al. 2023), we assume a $1.57 M_\odot$ NS with constant mass, and note that although cores become more compact during evolution on the giant branch, their mass increases only slightly, if at all, within this parameter space. This allows us to simplify our approach with the assumption that for any model of a given initial mass that satisfies $q_c < 1$, any profile from its evolution still satisfies this criterion in the merger regime.

Knowing the value of q_c, though sufficient as a disruption criterion, does not directly inform whether an accretion disk is formed. In fact, disruption of the core is not required for accretion disk formation, suggesting there may be a critical rotation rate $\Omega_{\rm crit}$ below which TŻO formation is possible. To derive this value, we first define the minimum specific angular momentum required to maintain an orbit about the compact object as

$$j_{\rm isco} \approx \frac{2GM_{\rm CO}}{v_{\rm esc}}, \tag{5.6}$$

in which $v_{\rm esc}$ is the escape velocity of the compact object. Post-merger, the core material surrounds the central compact object, and has been spun up to some degree by the end of the inspiral process. We can approximate the total angular momentum of the core as

$$J \approx M_{\rm CO}\sqrt{G(M_{\rm CO} + M_{\rm core})R_{\rm core}}, \tag{5.7}$$

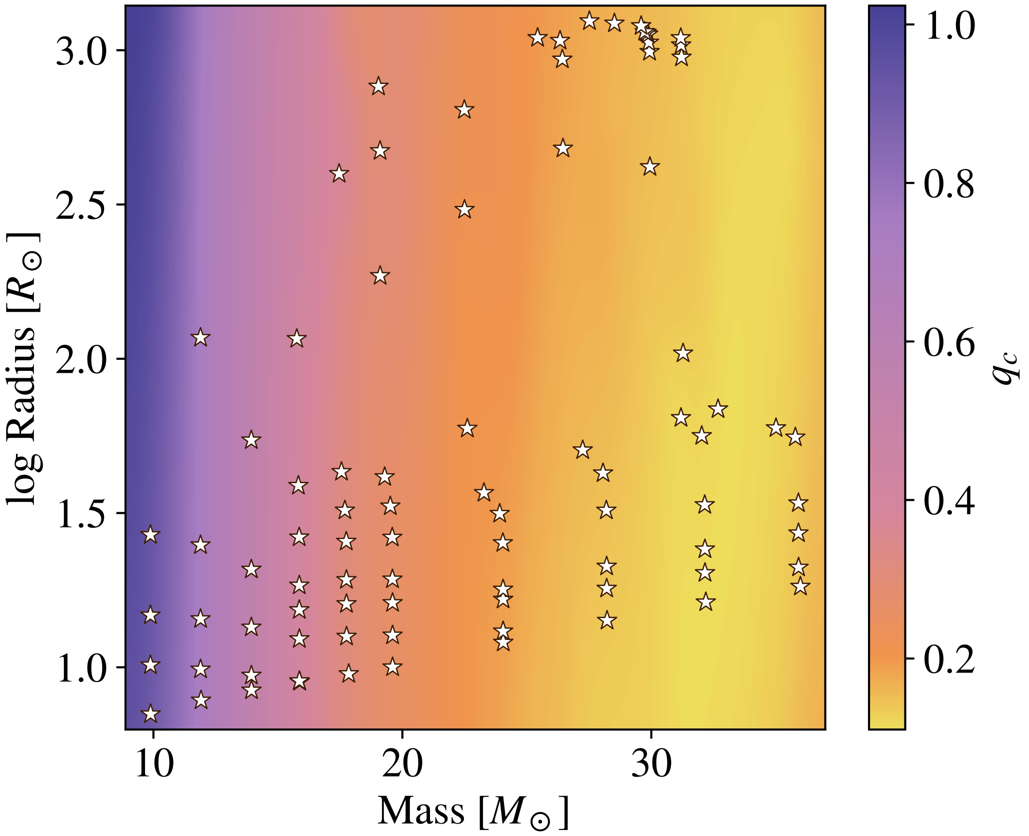

Figure 5.3 NS merger models in which the core remains intact (white stars), overplotted on mapped values of the mass ratio of the compact object and core: $q_c := M_{\rm CO}/M_{\rm core}$. Stellar tracks evolve bottom to top, and slightly leftward due to wind-driven mass loss. Note that, although total stellar mass decreases during post-main sequence evolution, the q_c values shown here are more or less constant with radius because core masses change very little within this parameter space. Complete core disruption occurs for $q_c > 1$, shown on the left edge in dark purple.

assuming the limiting case in which the inspiraling compact object transfers all of its angular momentum to an initially non-rotating core. This gives a rotation rate of $\Omega = J/I_{\rm core}$, in which $I_{\rm core}$ is the moment of inertia of the core given solid-body rotation.

In order to avoid accretion disk formation, the specific angular momentum of the core material must be less than that required to main orbit, $j_{\rm isco}$. Therefore, the rotation rate of the core Ω must be less than the critical rate of

$$\Omega_{\rm crit} = \frac{j_{\rm isco} M_{\rm core}}{I_{\rm core}}. \tag{5.8}$$

This provides an expression for the critical rotation rate that is dependent on the properties of the compact object and the core:

$$\Omega_{\rm crit} = \frac{2GM_{\rm CO}}{\xi v_{\rm esc} R_{\rm core}^2}, \tag{5.9}$$

in which $\xi = I_{\rm core}/M_{\rm core}R_{\rm core}^2$ parameterizes the internal structure of the core after the merger. We then have the condition for TŻO formation that

$$\frac{\Omega}{\Omega_{\rm crit}} = \frac{v_{\rm esc}}{2M_{\rm core}} \sqrt{\frac{(M_{\rm CO} + M_{\rm core})R_{\rm core}}{G}} < 1. \tag{5.10}$$

The values of this expression mapped over the TŻO progenitor systems are shown in Figure 5.4. Throughout the relevant parameter space, the minimum of this value is $\Omega/\Omega_{\rm crit} \approx 36$, which implies that disk formation is inevitable. Yet, perhaps disk formation is not instantaneous throughout the core: the

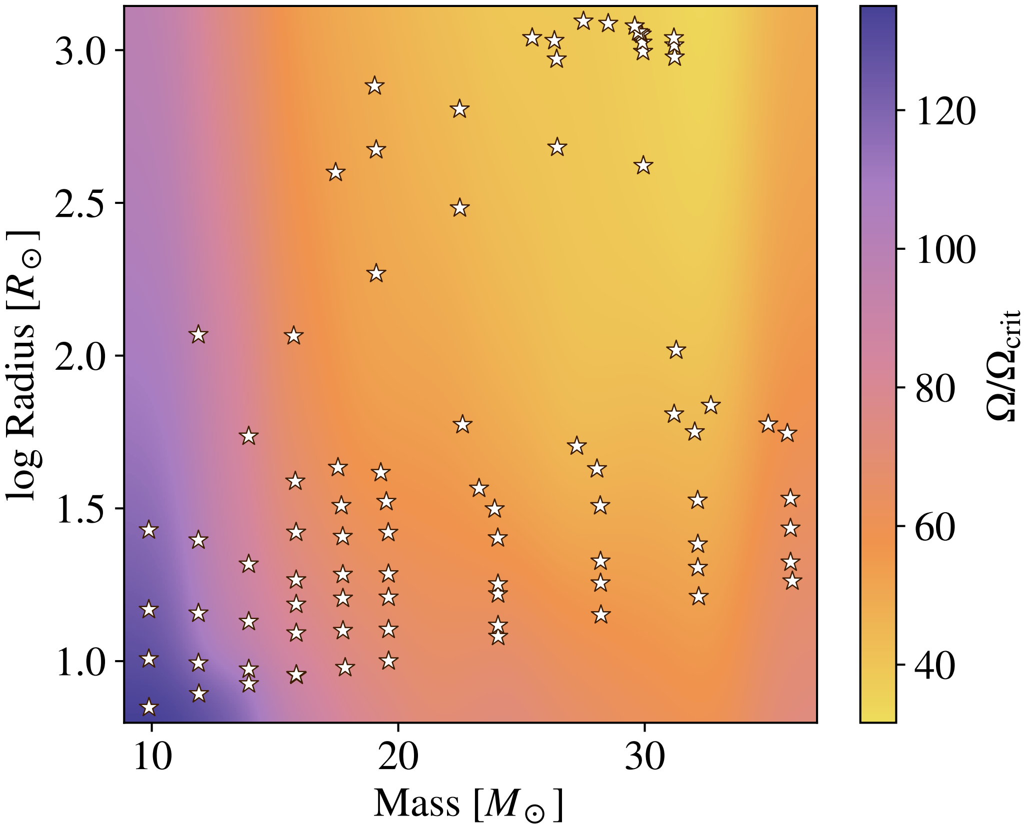

Figure 5.4 Minimum rotation rates for mergers with NS in which the core remains intact, normalized by the critical rotation rate for disk formation. Modeled systems are overplotted with white stars. Typical rotation rates in this parameter space are 1-2 orders of magnitude higher than Ω_crit, showing disk formation in the core to be inevitable upon merger.

specific angular momentum j of the core material is a function of density in the core and cannot be treated as constant. We proceed to look more deeply into core structure to investigate how and where disk formation may occur.

5.3 Implications of Core Structure on Disk Formation

In order to perform a broad analysis of angular momentum content in a range of progenitor cores upon merger, we use the `MESA` model library described in Section 5.2.1 to cover the relevant parameter space. In all cases, we use the conservative estimate that the post-merger core undergoes solid-body rotation at the rate defined by the total angular momentum content of the secondary at R_{core}, neglecting any prior spin up due to shocks.

In Figure 5.5, we show that this approximation is consistent with the core's angular momentum content as measured in our 3D hydrodynamic simulations at the end of inspiral. The NS case is shown for a secondary of $1.57 M_{\odot}$, with the specific angular momentum profiles normalized by j_{isco} as in Equation 5.6. Roughly, j/j_{isco} is a more detailed, structure-dependent proxy of $\Omega/\Omega_{\mathrm{crit}}$, in that these ratios would be equivalent if j is a constant for the core. The profiles in copper are calculated from a 1D spherical average about the center of mass in the 3D `FLASH` simulation described in Section 5.2.2, shown at various radii during inspiral. Depicted in yellow is the same quantity derived from the initial mass 18 $M_{\odot}$ `MESA` model that provided the stellar structure for the `FLASH` simulation.

We define the mass and radius of the `MESA` profile's stellar core using the traditional core boundary criterion of $X_{\mathrm{H}} = 0.1$; the appropriate definition of the core boundary in CE and merger calculations is still an area of active

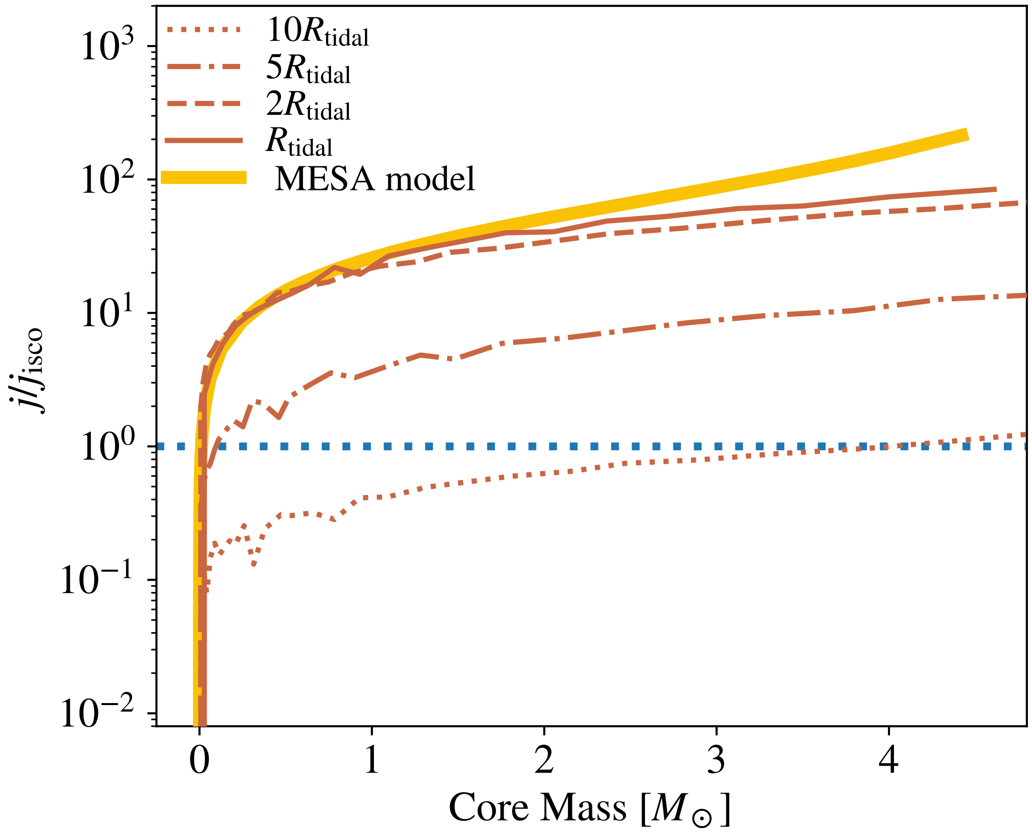

Figure 5.5 Comparison of normalized specific angular momentum content $j/j_{\rm isco}$ of the core of 18 $M_\odot$ model in `FLASH` (3D) and `MESA` (1D). The specific angular momentum ratio required for disk formation ($j/j_{\rm isco} > 1$) is delimited by the blue dotted line. The `MESA` model corresponding to the `FLASH` simulation is shown in yellow, spun up in solid-body rotation to the total orbital angular momentum of a NS secondary at $R_{\rm core}$. The angular momentum from the `FLASH` simulation is shown in copper at different depths during inspiral, from 10 $R_{\rm tidal}$ to $R_{\rm tidal}$ (within the core, in this case). The 1D model in solid-body rotation gives a close approximation to the initial state of the core during merger, therefore we use this approach to investigate the prevalence of disk formation in cores across the parameter space during merger.

discussion, and we defer to that used most often in the literature as it provides a lower limit for available angular momentum while recognizing that more nuanced definitions may ultimately be more physically relevant (see, e.g., Tauris & Dewi 2001; Ivanova et al. 2013; Everson et al. 2020; Vigna-Gómez et al. 2022).

We then calculate the total angular momentum (Equation 5.7) as the orbital angular momentum of the NS at $R_{\rm core}$ and derive the rate of solid-body rotation Ω with the integrated moment of inertia $I_{\rm core}$ from the `MESA` profile. The radial profile of the core combined with the rate of rotation gives the specific angular momentum profile, which we then compare to our simulation results.

It is clear that in the simulated merger, shocks during inspiral begin to spin up the core long before the arrival of the NS (Figure 5.5, copper profiles from bottom to top), however this doesn't create a large departure from the 1D profile. For non-disrupted cores such as this one, $R_{\rm tidal} < R_{\rm core}$, so the specific angular momentum profile at $R_{\rm tidal}$ gives a snapshot of the rotation as merger is occurring. The assumption of solid-body rotation in the core upon merger gives a close approximation to the rotation of the simulated core at that moment.

Most notable is how much greater than unity the profiles shown in Figure 5.5 are: the blue dotted line represents the minimum value of j required for disk formation about the NS, and this specific stellar model achieves this while the NS is still plunging through the envelope. Nonetheless, differences in the internal structure of the core during post-main sequence evolution will impact the shape of these profiles, further motivating the analysis of the full set of `MESA` models in search of a case that does not meet this minimum, at least in part.

In Figure 5.6, we show a representative sample in the NS case of how the angular momentum content of the stellar core differs as the primary evolves through the giant branch and the core becomes more compact. The center panel shows a schematic of the evolution of an 8 $M_\odot$ star (A→B) and an 18 $M_\odot$ star (C→D) through the mass-radius parameter space shown in the left panel of Figure 5.1, with time proceeding bottom to top. These stellar models are selected as representative of mergers with disrupted and non-disrupted cores, respectively, while the 18 $M_\odot$ model is the same used for analysis in Figures 5.2 and 5.5, as well as in the simulations of Hutchinson-Smith et al. (2023).

The outer panels of Figure 5.6 show the specific angular momentum content of the core material, normalized by $j_{\rm isco}$, as a function of mass for the series of models represented in the center panel, with time proceeding top to bottom, calculated with `MESA` profiles in the same manner we describe above. The evolution depicted in the outer panels is representative of the evolution of all other models in the same regimes (disruptive or non-disruptive mergers). Line color corresponds to the region in the center panel that the stellar model occupies, such that all beige models are excluded from forming TŻOs due to envelope ejection prior to merger.

In order to form something like a classical TŻO, the NS star would need to

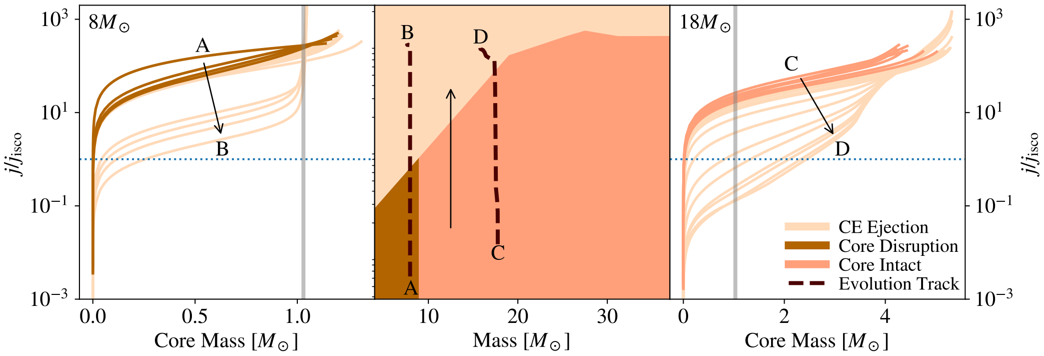

Figure 5.6 Normalized specific angular momentum of cores of 8 $M_\odot$ (left panel) and 18 $M_\odot$ (right panel) `MESA` models undergoing solid-body rotation at the rate defined by $J_{\rm NS}(R_{\rm tidal})$ at various stages of post-main sequence evolution. The center panel shows the CE outcome regions detailed in Figure 1, left panel, with dashed lines mapping the increase in radius from bottom to top over the post-main sequence of two stellar models. Outside panels show the normalized specific angular momentum profile of the core through the evolution tracks shown, with line color matching the corresponding region of CE outcome. The minimum specific angular momentum value required for disk formation is indicated by the blue dotted line, and the minimum core mass required to collapse the NS to BH is indicated by the vertical gray line. Note that in every case in which merger occurs (brown and coral), the cores undergo total disk formation with the most conservative assumptions about rotation. Partial disk formation would only be possible when merging with extended models (beige), but CE ejection prevents such mergers from occurring.

undergo quasi-spherical accretion for some length of time. In Figure 5.6, this would appear as a model for which some central region of the core maintains $j/j_{\rm isco}$ values below unity, depicted by the blue dotted line, in which partial-disk formation might occur in the outer region of the core while the interior undergoes quasi-spherical accretion. The only cores which would satisfy such partial-disk formation in Figure 5.6 are CE ejection cases (beige). In fact, when we apply this analysis across the full parameter space of models ($5-40\,M_\odot$), we find that in every binary system that fulfills the energetic criterion for merger (coral or brown), the core is rotating well above this limit based solely on the orbital angular momentum of the NS at $R_{\rm core}$.

In all so-called TŻO progenitor systems, the core must undergo total disk formation upon merger. This is further supported by the `FLASH` simulations (Figure 5.5), in which the shockwaves from inspiral spin up the core such that its angular momentum content satisfies the criterion for total disk formation when the secondary is still as much as $5R_{\rm tidal}$ away from the center of mass and has not yet merged with the core.

This should not be surprising: recent work on the collapse of single giant stars has shown that disk formation is difficult to avoid (Murguia-Berthier et al. 2020), and that even with zero net angular momentum, convection in the extended hydrogen envelope leads to specific angular momentum profiles greater than $j_{\rm isco}$ (Quataert et al. 2019; Antoni & Quataert 2022), leading to accretion disk formation. Though mergers tend to happen when envelopes are more compact, the deposition throughout the primary of orbital angular momentum via shocks guarantees a non-zero net angular momentum even in the innermost core material.

5.4 Discussion

The above analysis suggests that it is not accretion feedback nor the accompanying jets during inspiral that prevent the formation of TŻOs, but the immediate formation of an accretion disk upon merger, disallowing any stable radial accretion to power the star. Consideration of the most basic details of CE inspiral thus precludes the formation of classical TŻOs from field binaries altogether.

This is not to say that so-called TŻO progenitors are not of great interest. Such systems may be the precursors to a broad range of transients occurring in succession in the same system: starting as an X-ray binary, then producing a recombination transient through partial envelope ejection during CE inspiral (i.e. luminous red nova; see, e.g., MacLeod et al. 2017a, 2022), followed by collapse to a black hole and a subsequent accretion feedback transient (i.e., gamma-ray burst; MacFadyen & Woosley 1999; MacFadyen et al. 2001; Zhang & Fryer 2001; Izzard et al. 2004). The effects of the unique post-merger mass distribution and morphology of these systems may even lend them to new types of transients (e.g., Schrøder et al. 2020) that could be detected by surveys like LSST (Ivezić et al. 2019) and Swift (Gehrels et al. 2009).

But perhaps the story of TŻOs need not end here. After the dynamic process of merger and the NS's collapse to BH, we speculate that an alternative steady-state merger product may be possible: a thin-envelope T$\dot{\text{Z}}$O (TET$\dot{\text{Z}}$O).

5.4.1 Reimagining T$\dot{\text{Z}}$Os

Some fraction of the envelope will be ejected during CE inspiral, but due to accretion feedback, any remaining envelope will be quickly unbound in most cases. However, in cases where the core's binding energy is not as dominant when compared to that of the envelope, a thin-envelope may be retained close to the core if the efficiency of feedback is sufficiently low. The ratio of the binding energy of the core to the binding energy of the envelope is shown for the NS case in Figure 5.7. Only in the the late stages of the main sequence and the earliest stages of the post-main sequence is this ratio at or below unity, suggesting that TET$\dot{\text{Z}}$O candidates are most likely formed from close binaries in which the stellar partner has not evolved far from the main sequence, as we see in the forward-evolved model of LMC X-4 from Hutchinson-Smith et al. (2023).

In comparison to wider binaries at the onset of merger, such systems contain less total angular momentum and orbital energy while having a more tightly bound envelope, all of which serve to increase the likelihood some envelope may remain once the merger and subsequent collapse are complete. A steady-state TET$\dot{\text{Z}}$O occurs when the envelope remnant, supported by radiation pressure, is able to achieve hydrostatic equilibrium about the accreting BH. The timescale from merger to TET$\dot{\text{Z}}$O formation is unclear due to vari-

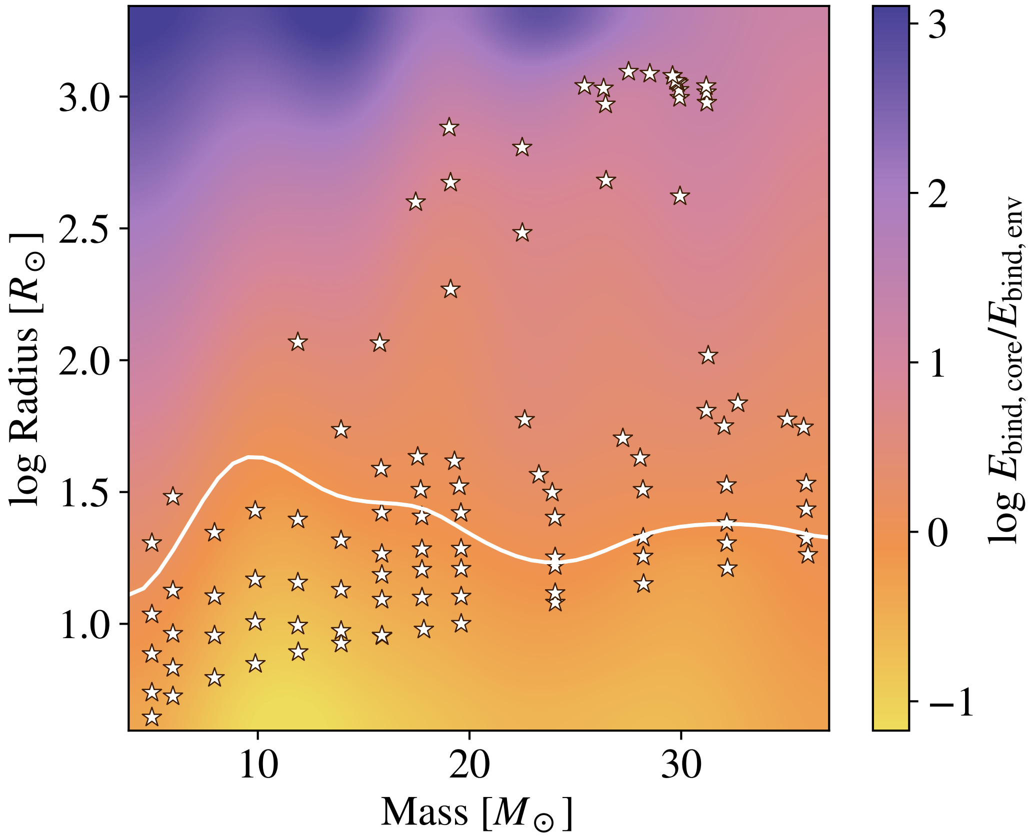

Figure 5.7 NS merger models (white stars) overplotted on mapped values of the ratio of the gravitational binding energy held in the stellar core versus that held in the envelope. In order to retain a thin envelope in a merger scenario, the energy deposition due to the accretion of the core should be insufficient to unbind the remaining envelope (roughly, $E_{\rm bind,core}/E_{\rm bind,env} < 1$, delimited by the white line). Using this ratio as a rough estimate, this criterion is satisfied only for stellar companions in the early stages of the post-main sequence.

ous uncertainties in mass ejection and the intervening transient events noted above; these will be explored in detail in a follow-up paper.

A schematic of the general structure of a TETŻO is shown in Figure 5.8. We consider a radiation supported envelope with negligible self gravity, with less than 1% of the initial envelope mass remaining with the rest being ejected by accretion feedback that gave rise to the bright transient. The thin envelope is feeding matter to the black hole, converting a fraction ϵ of the accreting mass into radiation ($L = \epsilon \dot{M} c^2$), which is reprocessed through the surrounding optically thick envelope before it reaches the observer. The conversion of envelope mass into radiation in the accretion disk would then fuel the surrounding envelope in much the same way as originally envisioned by Thorne and Żytkow.

Under these circumstances, the surrounding envelope might approach a steady state in which the interplay between gravity and radiation pressure provides a stabilizing feedback. This is because an increase in the luminosity above the Eddington limit,

$$\begin{aligned} L = L_{\mathrm{Edd}} &= \frac{4\pi G \mu_e m_p c M_{\mathrm{bh}}}{\sigma_T} \\ &= 1.4 \times 10^{39} \left(\frac{M_{\mathrm{bh}}}{10\, M_\odot} \right) \mathrm{erg/s}, \end{aligned} \tag{5.11}$$

would result in an outflow and, as a result, will reduce the accretion luminosity. Here μ_e is the mean atomic weight per electron. Conservation of momentum demands that mass is ejected from the photosphere of this envelope as a wind,

$\dot{M}_{\rm wind} v_\infty \approx L_{\rm Edd}/c$, where v_∞ is the escape velocity at the photosphere (R_τ).

Accretion below the Eddington limit would, on the other hand, increase the infall rate and hence bring the luminosity back to its equilibrium value (Cowie et al. 1978). In this configuration, which is similar to the one envisioned by Loeb & Ulmer (1997) for tidal disruption events, the gravitational force is provided primarily by the central point mass, whereas in a classical TŻO it is given by the self-gravity of a massive envelope. The existence of a steady, spherical, optically thick envelope around the black hole should thus be regarded as the most optimistic expectation for the appearance of a TETŻO.

The luminosity at the photosphere depends on the effective temperature (Loeb & Ulmer 1997),

$$\begin{aligned} T_{\rm ph} &\approx \left(\frac{L_{\rm Edd}}{4\pi R_\tau^2}\right)^{1/4} \\ &\approx 10^6 \left(\frac{M_{\rm bh}}{10\,M_\odot}\right)^{1/4} \left(\frac{M_{\rm env}}{5\times 10^{-3}\,M_\odot}\right)^{-1/4} {\rm K}. \end{aligned} \tag{5.12}$$

The effective temperature has a very weak dependence on $M_{\rm bh}$ and $M_{\rm env}$, and would be commonly associated with an ultra-luminous ($\gtrsim 10^{39}$ erg/s) soft X-ray source. The color prediction of such TETŻOs appear relatively robust unless a sizable fraction of the envelope remains and the ultra-luminous sources would instead peak at UV energies. For a constant radiative efficiency ($\epsilon = 0.1\epsilon_{-1}$), the lifetime of a TETŻO can thus be written as

$$t_{\rm life} \approx 10^4 \left(\frac{M_{\rm bh}}{10\,M_\odot}\right)^{-1} \left(\frac{M_{\rm env}}{5\times 10^{-3}\,M_\odot}\right) \epsilon_{-1}\ {\rm yr}. \tag{5.13}$$

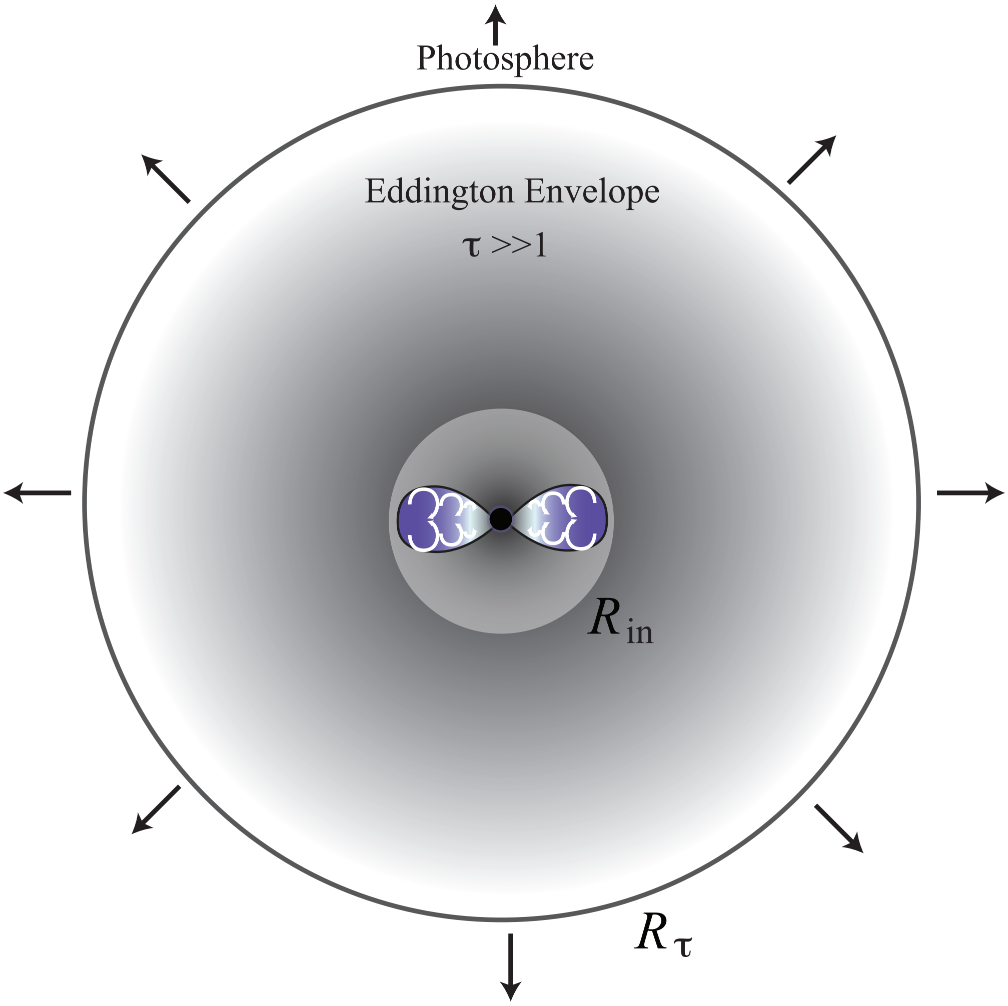

Figure 5.8 A schematic of the structure of a TETŻO is shown, illustrating a possible configuration for merger remnants following several transient events. After most of the stellar envelope has been ejected or depleted and the NS has collapsed due to mass accretion, a central BH accretes via disk (with a typical circularization radius R_{in}) with the disk providing radiation support to an optically-thick thin envelope that extends to the photosphere at R_τ. This radius is calculated where the radiation-dominated diffuse envelope transitions from being optical thick to optically thin.

The above envelope configuration could exist for as long as $\approx 10^4 - 10^6$ years, depending on $M_{\rm bh}$, ϵ, and $M_{\rm env}$.

We can then estimate how many TETŻOs are predicted to reside in galaxies like our own. Based on CE population synthesis models (Vigna-Gómez et al. 2020; Schrøder et al. 2020), we expect a TETŻO formation rate for Milky Way-type galaxies to be $\approx 10^{-3}$ yr^{-1}. With a lifetime of $\approx 10^4$ years (Equation 5.13), we thus expect a handful of candidates per galaxy (although we note that this estimate is highly sensitive to $M_{\rm env}$).

5.4.2 In Search of TETŻOs

Interestingly, TETŻOs have predicted luminosities ($\approx 10^{39}$ erg/s) and photon temperatures (≈ 0.1 keV) that are similar to ultraluminous X-ray sources (ULX) and should occur at similar rates of a few per galaxy (Tranin et al. 2024). ULXs preferentially appear in regions that have recently undergone high rates of star formation, as do X-ray binaries and massive stars (see, e.g., Liu et al. 2006; Shields et al. 2012; Earnshaw et al. 2019), implying that they share the ideal environment for TETŻO formation. Though it is still an open question whether NSs or BHs are the dominant engines of ULXs (Gúrpide et al. 2021; Walton et al. 2022), there is high-quality data supporting that some ULX properties may be best explained by accreting stellar-mass BHs (Pintore et al. 2018). Therefore it is plausible that TETŻOs may not only be the end products of CE events that lead to the merger of X-ray binaries, but that they may have already been uncovered.

One indication that a ULX may be associated with a TETŻO could come from high-cadence time-domain surveys such as LSST (Ivezić et al. 2019) and eRosita (Merloni et al. 2020): the formation of a TETŻO would begin with the detection of a bright transient due to the central BH accreting the dense remnant core from the primary. A fairly bright and fairly isotropic optical transient is expected to accompany the disruption of the envelope (Schrøder et al. 2020) while an ultra-long gamma-ray burst (Hutchinson-Smith et al. 2023) might be detected for observers along the axis of the jet. Rather than fading away, the remnant would instead settle down over time to a steady-state ULX. An event of this kind would need to be relatively close for the post-merger ULX to be seen, but could be a clear signature indicating TETŻO formation.

5.5 Summary

In this paper, we set out to find the formation pathways that would lead to TŻO formation from field binaries. After constraining our parameter space of progenitors through the lens of common envelope ejection criteria, we have explored the implications of angular momentum deposition on the primary's core based on global properties of the star and its companion (e.g. $M_{\rm core}$, $R_{\rm core}$, $M_{\rm CO}$), 3D hydrodynamics based on the setup of Hutchinson-Smith et al. (2023), and analysis of a library of detailed 1D stellar models. Upon ruling out the formation of TŻOs from these systems, we have proposed other possible outcomes based on our findings. So-called T$\dot{Z}$O progenitors are of great interest to transient astronomy due to their potential to sequentially produce a broad range of transient phenomena across the electromagnetic spectrum, and further work to understand the varied and dynamic lifetimes of these systems is merited.

The key conclusions of this work are the following:

- Classical T$\dot{Z}$Os, if they exist, are unlikely to be assembled in field binaries. The merger process favors the conditions required to form an accretion disk in the core, which prevent the radial accretion that would power a steady-state T$\dot{Z}$O. The core structure of the primary during merger has no bearing on T$\dot{Z}$O formation, regardless of whether it remains intact or is disrupted.
- We propose an alternative merger product that may form around the resulting stellar-mass black hole after collapse: the thin-envelope T$\dot{Z}$O (TET$\dot{Z}$O). Feedback from the accretion of the remaining core material is likely to eject most or all of the stellar envelope, but if a minimal amount ($\lesssim 1\%$) remains, a steady-state configuration may arise in which the optically thick thin-envelope is powered by the accretion luminosity of the black hole.
- We find that post-merger TET$\dot{Z}$Os are likely to be associated with ultraluminous soft X-ray sources and that they may have already been detected in nearby galaxies at rates that are comparable with those pre-

dicted here.

5.6 Software Utilized

`Python`, `MESA` (Paxton et al. 2011, 2013, 2015, 2018, 2019), `FLASH` (Fryxell et al. 2000), `COMPAS` (Team COMPAS: Riley et al. 2022), `matplotlib` (Hunter 2007), `yt` (Turk et al. 2011), `NumPy` (van der Walt et al. 2011), `py_mesa_reader` (Wolf & Schwab 2017).

Chapter 6

Conclusion

6.1 Summary

Common envelope evolution is an essential component in the dynamic evolution of interacting binary systems, reshaping and rejuvenating the population of remnant binaries and merger products that these events leave behind. Though a fully developed understanding of the CE phase remains elusive, its broad relevance in transient astrophysics motivates the continued development and refinement of semi-analytical and numerical treatments for CE that are capable of mapping initial conditions to post-CE outcomes. This dissertation broke new ground in this effort, elucidating new pathways toward the improvement of the theoretical foundations of CE evolution by incorporating inspiral dynamics, developing a new combined 1D/3D numerical framework that can capture the broad range of relevant timescales in a CE event, and demonstrating the important role of inspiral dynamics in predictive models and specific merger outcomes.

6.2 Future Directions

6.2.1 Modeling Light Curves of Common Envelope Ejecta

The field of CE evolution is extremely active, with upcoming high-cadence time-domain surveys ushering in the exciting prospect of plentiful observational constraints on CE physics. Over the last decade, it has become clear that luminous red novae (LRNe) are the most promising events for studying CE evolution via observation (Ivanova et al. 2020). Since seminal work by Tylenda et al. (2011) demonstrated that V1309 Sco was the product of a contact binary merging explosively through a CE phase, much effort has been devoted to analyzing and modeling the handful of known events, including M31-LRN2015 (MacLeod et al. 2017a), M101-OT2015-1 (Blagorodnova et al. 2017), and a half dozen others (Tylenda et al. 2005; Smith et al. 2016; Pastorello et al. 2023). It is generally accepted that LRNe are CE events, along with their dimmer cousins, the red novae, that have been proposed to be lower mass, dust-obscured versions of LRNe (Pastorello et al. 2019; MacLeod et al. 2022).

There are several open questions related to LRNe that are yet to be addressed: there is a discrepancy between the velocity of the ejecta, which tends to be several times greater than escape velocity and implies ejection from deep within the primary, and the relatively low mass of the ejecta, which favors ejection from the surface layers of the primary; additionally, it is unclear whether recombination or shocks are responsible for powering the emission from ejecta, or if it happens to be a combination of both, which properties of the LRN progenitor define which process dominates.

Though several current models do a fair job at reproducing the light curves from LRNe, the prescriptions used for CE mass ejection are either fine-tuned to match observation through parameterization in population synthesis (e.g., Howitt et al. 2020) or are based on the assumption of spherical symmetry inherent in 1D models (e.g., Matsumoto & Metzger 2022). Both of these approaches result in a mass-loss prescription that, even if it works, is phenomenological at best. Blagorodnova et al. (2021) modeled the last stages of merger after a LRN with 3D smooth particle hydrodynamics, but did so by injecting mass to simulate the observed ejecta, again taking a phenomenological approach.

The addition of radiation transport to detailed global simulations with realistic equations of state, such as those presented in this dissertation, can support the generation of realistic light curves for comparison to 1D models to constrain the conditions under which 1D calculations adequately capture the physical processes reflected in 3D. Additionally, such global simulations, especially if core-resolved, can track the origin of CE ejecta to resolve the velocity discrepancy and provide insight on how orbital energy deposition during onset is distributed in the outer envelope. As the primary observational sources of information about CE, insights gained from modeling LRNe in great detail will have implications across the entire field of interacting binaries.

6.2.2 The End of Common Envelope Inspiral

One of the most pressing questions for the modeling of CE interactions, particularly for those that study this mechanism as a channel for the formation of close binaries, is how the CE process comes to a successful conclusion, i.e. the envelope is fully ejected and binarity of the system is preserved. To date, the most common workaround to this issue in 1D calculations and population synthesis has been to parameterize the efficiency term α (see Subsection 3.2.1) such that the outcome is consistent with an observed population (Ivanova et al. 2013). However, a first-principles understanding of the various physical processes that contribute to the outcome remains elusive.

An extensive body of work using 3D simulations to study CE events has neither shown full envelope ejection, even when the CE energy formalism predicts it, nor the secondary's transition from the initial plunge to a separation that reflects the observed population of post-CE binaries (see Röpke & De Marco 2023, and references therein). Though these models' inability to unbind the envelope may point to missing physics (i.e., reionization and/or accretion feedback) or energy transport timescale considerations (e.g., Chapter 3), the mechanisms that slow the secondary's plunge to bring it into a much shallower, self-regulated inspiral and final separation at the end of a CE event are obscured by the models' treatment of the primary's core. In all of these simulations, the stellar core is replaced with a softened-potential gravitational point mass that cannot react to the changes in stellar structure brought on by CE. This is a shortcoming that a core-resolved numerical setup is able to overcome because it resolves changes in and around the core material throughout a CE event and can reveal its effects on the end of the dynamical plunge. However, the tradeoff of resolving the core is that the extent of the primary is constrained by numerical limitations: in order to carry out a global simulation of CE, the primary must be relatively compact which energetically predisposes the system to merger. Approaching this problem for systems that fit the criteria for envelope ejection requires a synthesis of several computational tools, informed by prior 3D results.

This limitation was addressed by Law-Smith et al. (2020a) by simulating a stripped primary, though, as discussed in Chapter 3, the amount of envelope removed was informed by the energy criterion only, without regard to relevant CE timescales. By selecting initial conditions for such models with these timescales in mind, and perhaps additional lessons learned about CE onset, the results would provide more robust insight into the role that the response of the core plays in the final stages of CE inspiral and help characterize how CE events come to an end. Such results could also improve simpler prescriptions that have recently been proposed to describe this phase of CE (Hirai & Mandel 2022) that, similar to the 3D simulations described above, give final separations too wide to be consistent with the observed populations when incorporated into binary population synthesis (Romero-Shaw et al. 2023).

6.2.3 Upgrading the Common Envelope Energy Formalism

Among the CE community, it is a frequent topic of discussion that the energy formalism described in Subsection 3.2.1 and applied throughout this work is insufficient to capture the complexities of CE evolution and should be replaced, or overhauled at the very least. It has been updated occasionally with the addition of more free parameters (de Kool 1990) or incorporating angular momentum (Nelemans et al. 2000; Hirai & Mandel 2022), but the question of the efficiency of envelope ejection has remained one of the most puzzling and complex aspects of CE. After forty years, the most up-to-date binary population synthesis codes still rely on the traditional energy formalism, or some modification thereof, with efficiency as a free parameter (e.g., Breivik et al. 2020; Hamers et al. 2021; Fragos et al. 2023). After decades of trying to incrementally improve this formalism, it is unclear whether it is even possible to create effective functional forms of its parameters due to fundamental uncertainties about stellar evolution and CE itself (Ivanova et al. 2013, 2020).

The work presented in Chapters 2 and 3 suggests the possibility of broad prescriptive application of the CE drag formalism through an updated CE framework that combines energy considerations with details of inspiral dynamics. However, a better understanding of the structural changes induced by onset as well as the transition from dynamical inspiral to self-regulated inspiral would greatly improve this preliminary framework and broaden its applicability, with the objective of implementing the updated CE treatment as a module for binary population synthesis codes. A physically-motivated alternative to the traditional CE energy formalism would directly answer the call from the community of CE researchers for a viable alternative to a dated formalism that does not address the complexities of any single phase of CE evolution.

The results presented in this work provide the foundation for a number of high-impact and timely studies with the potential to significantly move the field forward. It is an exciting time to be working at the interface of time-domain astronomy and binary stellar evolution, where the cosmic choreography of the common envelope phase shapes and reshapes systems of partnered stars across the universe in a brilliant, sweeping dance.

Bibliography

Abbott B. P., et al., 2019, Phys. Rev. X, 9, 031040

Abbott R., et al., 2023, Phys. Rev. X, 13, 041039

Ablimit I., Podsiadlowski P., Hirai R., Wicker J., 2022, MNRAS, 513, 4802

Almeida L. A., et al., 2017, A&A, 598, A84

Antoni A., Quataert E., 2022, MNRAS, 511, 176

Beasor E. R., Davies B., Cabrera-Ziri I., Hurst G., 2018, MNRAS, 479, 3101

Belczynski K., Kalogera V., Bulik T., 2002, ApJ, 572, 407

Belczynski K., et al., 2022, ApJ, 925, 69

Bertelli G., Bressan A., Chiosi C., Fagotto F., Nasi E., 1994, A&AS, 106, 275

Bethe H. A., Brown G. E., 1998, ApJ, 506, 780

Biehle G. T., 1991, ApJ, 380, 167

Blagorodnova N., et al., 2017, ApJ, 834, 1

Blagorodnova N., et al., 2021, A&A, 653, A134

Bondi H., Hoyle F., 1944, MNRAS, 104, 273

Breivik K., et al., 2020, ApJ, 898, 71

Cannon R. C., 1993, MNRAS, 263, 817

Cannon R. C., Eggleton P. P., Zytkow A. N., Podsiadlowski P., 1992, ApJ, 386, 206

Chamandy L., et al., 2018, MNRAS, 480, 1898

Chamandy L., Tu Y., Blackman E. G., Carroll-Nellenback J., Frank A., Liu B., Nordhaus J., 2019a, MNRAS, 486, 1070

Chamandy L., Blackman E. G., Frank A., Carroll-Nellenback J., Zou Y., Tu Y., 2019b, MNRAS, 490, 3727

Chevalier R. A., 1993, ApJ, 411, L33

Choi J., Dotter A., Conroy C., Cantiello M., Paxton B., Johnson B. D., 2016, ApJ, 823, 102

Claeys J. S. W., Pols O. R., Izzard R. G., Vink J., Verbunt F. W. M., 2014, A&A, 563, A83

Clayton M., Podsiadlowski P., Ivanova N., Justham S., 2017, MNRAS, 470, 1788

Cowie L. L., Ostriker J. P., Stark A. A., 1978, ApJ, 226, 1041

Dale J. E., Davies M. B., 2006, MNRAS, 366, 1424

Dan M., Rosswog S., Guillochon J., Ramirez-Ruiz E., 2011, ApJ, 737, 89

Davis P. J., Kolb U., Willems B., 2010, MNRAS, 403, 179

De S., MacLeod M., Everson R. W., Mandel I., Ramirez-Ruiz E., 2020, ApJ, 897, 130

Dotter A., 2016, ApJS, 222, 8

Earnshaw H. P., Roberts T. P., Middleton M. J., Walton D. J., Mateos S., 2019, MNRAS, 483, 5554

Eggleton P. P., 1983, ApJ, 268, 368

Eich C., Zimmermann M. E., Thorne K. S., Zytkow A. N., 1989, ApJ, 346, 277

Eisner N. L., et al., 2022, MNRAS, 511, 4710

Everson R. W., MacLeod M., De S., Macias P., Ramirez-Ruiz E., 2020, ApJ, 899, 77

Everson R. W., Hutchinson-Smith T., Vigna-Gómez A., Ramirez-Ruiz E., 2023, arXiv e-prints, p. arXiv:2310.08658

Farmer R., Renzo M., Götberg Y., Bellinger E., Justham S., de Mink S. E., 2023, MNRAS, 524, 1692

Fragos T., Andrews J. J., Ramirez-Ruiz E., Meynet G., Kalogera V., Taam R. E., Zezas A., 2019, ApJ, 883, L45

Fragos T., et al., 2023, ApJS, 264, 45

Freitag M., Benz W., 2005, MNRAS, 358, 1133

Fryxell B., et al., 2000, ApJS, 131, 273

Gallegos-Garcia M., Berry C. P. L., Marchant P., Kalogera V., 2021, ApJ, 922, 110

Gehrels N., Ramirez-Ruiz E., Fox D. B., 2009, ARA&A, 47, 567

Ghosh P., Angelini L., White N. E., 1997, ApJ, 478, 713

Glanz H., Perets H. B., 2018, MNRAS, 478, L12

Glebbeek E., Gaburov E., Portegies Zwart S., Pols O. R., 2013, MNRAS, 434, 3497

Grichener A., Sabach E., Soker N., 2018, MNRAS, 478, 1818

Guillochon J., Ramirez-Ruiz E., 2013, ApJ, 767, 25

Guillochon J., Ramirez-Ruiz E., Rosswog S., Kasen D., 2009, ApJ, 705, 844

Gúrpide A., Godet O., Koliopanos F., Webb N., Olive J. F., 2021, A&A, 649, A104

Guzik J., Fontes C., Fryer C., 2018, Atoms, 6, 31

Hamers A. S., Rantala A., Neunteufel P., Preece H., Vynatheya P., 2021, MNRAS, 502, 4479

Harpaz A., 1984, MNRAS, 210, 633

Heger A., Langer N., Woosley S. E., 2000, ApJ, 528, 368

Henyey L. G., Wilets L., Böhm K. H., Lelevier R., Levee R. D., 1959, ApJ, 129, 628

Hirai R., Mandel I., 2022, ApJ, 937, L42

Hirai R., Podsiadlowski P., 2022, MNRAS, 517, 4544

Howitt G., Stevenson S., Vigna-Gómez A., Justham S., Ivanova N., Woods T. E., Neijssel C. J., Mandel I., 2020, MNRAS, 492, 3229

Hoyle F., Lyttleton R., 1939, PCPS, 35, 405

Hunter J. D., 2007, Computing In Science & Engineering, 9, 90

Hutchinson-Smith T., Everson R. W., Batta A., Yarza R., Law-Smith J. A. P., Ramirez-Ruiz E., 2023, arXiv e-prints, p. arXiv:2311.06741

Hutilukejiang B., Zhu C., Wang Z., Lü G., 2018, Journal of Astrophysics and Astronomy, 39, 21

Iaconi R., Reichardt T., Staff J., De Marco O., Passy J.-C., Price D., Wurster J., Herwig F., 2017, MNRAS, 464, 4028

Iben Icko J., Livio M., 1993, PASP, 105, 1373

Ivanova N., 2002, PhD thesis, University of Oxford

Ivanova N., 2017, in Eldridge J. J., Bray J. C., McClelland L. A. S., Xiao L., eds, Proceedings of the International Astronomical Union Symposia and Colloquia Vol. 329, The Lives and Death-Throes of Massive Stars. pp 199–206 (`arXiv:1706.07580`), doi:10.1017/S1743921317003398

Ivanova N., Nandez J. L., 2016, MNRAS, 462, 362

Ivanova N., Podsiadlowski P., Spruit H., 2002, MNRAS, 334, 819

Ivanova N., et al., 2013, A&A Rev., 21, 59

Ivanova N., Justham S., Ricker P., 2020, Common Envelope Evolution. IOP Publishing, doi:10.1088/2514-3433/abb6f0

Ivezić Ž., et al., 2019, ApJ, 873, 111

Izzard R. G., Ramirez-Ruiz E., Tout C. A., 2004, MNRAS, 348, 1215

Jermyn A. S., et al., 2023, ApJS, 265, 15

Jiang Y. F., Cantiello M., Bildsten L., Quataert E., Blaes O., 2015, ApJ, 813, 74

Justham S., Podsiadlowski P., Vink J. S., 2014, ApJ, 796, 121

Kaplan D. L., Bildsten L., Steinfadt J. D. R., 2012, ApJ, 758, 64

Kruckow M. U., Tauris T. M., Langer N., Szecsi D., Marchant P., Podsiadlowski P., 2016, A&A, 596, 1

Lang F. L., et al., 1981, ApJ, 246, L21

Law-Smith J., Guillochon J., Ramirez-Ruiz E., 2019, ApJ, 882, L25

Law-Smith J. A. P., et al., 2020a, arXiv e-prints, p. arXiv:2011.06630

Law-Smith J. A. P., Coulter D. A., Guillochon J., Mockler B., Ramirez-Ruiz

E., 2020b, ApJ, 905, 141

Lee W. H., Ramirez-Ruiz E., 2006, ApJ, 641, 961

Lee W. H., Ramirez-Ruiz E., 2007, New Journal of Physics, 9, 17

Leonard P. J. T., Hills J. G., Dewey R. J., 1994, ApJ, 423, L19

Levesque E. M., Massey P., Zytkow A. N., Morrell N., 2014, MNRAS, 443, L94

Liu J.-y., Zhang F., 2022, Chinese Astron. Astrophys., 46, 164

Liu J.-F., Bregman J. N., Irwin J., 2006, ApJ, 642, 171

Livio M., Soker N., 1988, ApJ, 329, 764

Loeb A., Ulmer A., 1997, The Astrophysical Journal, 489, 573

Lombardi James C. J., Warren J. S., Rasio F. A., Sills A., Warren A. R., 2002, ApJ, 568, 939

MacFadyen A. I., Woosley S. E., 1999, ApJ, 524, 262

MacFadyen A. I., Woosley S. E., Heger A., 2001, ApJ, 550, 410

MacLeod M., Loeb A., 2020a, ApJ, 893, 106

MacLeod M., Loeb A., 2020b, ApJ, 895, 29

MacLeod M., Ramirez-Ruiz E., 2015a, ApJ, 798, L19

MacLeod M., Ramirez-Ruiz E., 2015b, ApJ, 803, 41

MacLeod M., Macias P., Ramirez-Ruiz E., Grindlay J., Batta A., Montes G., 2017a, ApJ, 835, 282

MacLeod M., Antoni A., Murguia-Berthier A., Macias P., Ramirez-Ruiz E., 2017b, ApJ, 838, 56

MacLeod M., Ostriker E. C., Stone J. M., 2018a, ApJ, 863, 5

MacLeod M., Ostriker E. C., Stone J. M., 2018b, ApJ, 868, 136

MacLeod M., De K., Loeb A., 2022, ApJ, 937, 96

Maccarone T. J., de Mink S. E., 2016, MNRAS, 458, L1

Mahy L., et al., 2020, A&A, 634, A119

Mandel I., de Mink S. E., 2016, MNRAS, 458, 2634

Marchant P., Pappas K. M. W., Gallegos-Garcia M., Berry C. P. L., Taam R. E., Kalogera V., Podsiadlowski P., 2021, A&A, 650, A107

Matsumoto T., Metzger B. D., 2022, ApJ, 938, 5

Merloni A., Nandra K., Predehl P., 2020, Nature Astronomy, 4, 634

Metzger B. D., Perley D. A., 2023, ApJ, 944, 74

Meynet G., Maeder A., 2000, A&A, 361, 101

Moe M., Di Stefano R., 2017, ApJS, 230, 15

Moreno M. M., Schneider F. R. N., Röpke F. K., Ohlmann S. T., Pakmor R., Podsiadlowski P., Sand C., 2022, A&A, 667, A72

Murguia-Berthier A., MacLeod M., Ramirez-Ruiz E., Antoni A., Macias P., 2017, ApJ, 845, 173

Murguia-Berthier A., Batta A., Janiuk A., Ramirez-Ruiz E., Mandel I., Noble S. C., Everson R. W., 2020, ApJ, 901, L24

Nandez J. L. A., Ivanova N., 2016, MNRAS, 460, 3992

Nandez J. L. A., Ivanova N., Lombardi J. C. J., 2014, ApJ, 786, 39

Nelemans G., Verbunt F., Yungelson L. R., Portegies Zwart S. F., 2000, A&A, 360, 1011

O'Grady A. J. G., et al., 2020, ApJ, 901, 135

O'Grady A. J. G., et al., 2023, ApJ, 943, 18

Ohlmann S. T., Röpke F. K., Pakmor R., Springel V., Müller E., 2016a, MNRAS, 462, L121

Ohlmann S. T., Röpke F. K., Pakmor R., Springel V., 2016b, ApJ, 816, L9

Ohlmann S. T., Röpke F. K., Pakmor R., Springel V., 2017, A&A, 599, A5

Paczynski B., 1976, in Eggleton P., Mitton S., Whelan J., eds, IAU Symp. 73, Structure and Evolution of Close Binary Systems. Dordrecht: D. Reidel, pp 75–80

Papish O., Soker N., Bukay I., 2015, MNRAS, 449, 288

Pasquali A., Nota A., Langer N., Schulte-Ladbeck R. E., Clampin M., 2000, AJ, 119, 1352

Passy J.-C., et al., 2012, ApJ, 744, 52

Pastorello A., et al., 2019, A&A, 630, A75

Pastorello A., et al., 2023, A&A, 671, A158

Paxton B., Bildsten L., Dotter A., Herwig F., Lesaffre P., Timmes F., 2011, ApJS, 192, 3

Paxton B., et al., 2013, ApJS, 208, 4

Paxton B., et al., 2015, ApJS, 220, 15

Paxton B., et al., 2018, ApJS, 234, 34

Paxton B., et al., 2019, ApJS, 243, 10

Perna R., Duffell P., Cantiello M., MacFadyen A. I., 2014, ApJ, 781, 119

Pintore F., et al., 2018, MNRAS, 479, 4271

Podsiadlowski P., 2001, in Podsiadlowski P., Rappaport S., King A. R., D'Antona F., Burderi L., eds, Astronomical Society of the Pacific Conference Series Vol. 229, Evolution of Binary and Multiple Star Systems. p. 239

Podsiadlowski P., Joss P. C., Hsu J. J. L., 1992, ApJ, 391, 246

Podsiadlowski P., Cannon R. C., Rees M. J., 1995, MNRAS, 274, 485

Podsiadlowski P., Mazzali P. A., Nomoto K., Lazzati D., Cappellaro E., 2004, ApJ, 607, L17

Podsiadlowski P., Morris T. S., Ivanova N., 2006, in Kraus M., Miroshnichenko A. S., eds, Astronomical Society of the Pacific Conference Series Vol. 355, Stars with the B[e] Phenomenon. p. 259

Postnov K. A., Yungelson L. R., 2014, Living Reviews in Relativity, 17, 3

Priyatikanto R., Knigge C., Scaringi S., Brink J., Buckley D. A. H., 2022, MNRAS, 516, 1183

Prust L. J., Chang P., 2019, MNRAS, 486, 5809

Quataert E., Lecoanet D., Coughlin E. R., 2019, MNRAS, 485, L83

Rasio F. A., Shapiro S. L., 1991, ApJ, 377, 559

Rasio F. A., Shapiro S. L., 1994, ApJ, 432, 242

Rasio F. A., Shapiro S. L., 1995, ApJ, 438, 887

Ray A., Kembhavi A. K., Antia H. M., 1987, A&A, 184, 164

Reichardt T. A., De Marco O., Iaconi R., Tout C. A., Price D. J., 2019, MNRAS, 484, 631

Ricker P. M., Taam R. E., 2008, ApJ, 672, L41

Ricker P. M., Taam R. E., 2012, ApJ, 746, 74

Ricker P. M., Timmes F. X., Taam R. E., Webbink R. F., 2019, in Oskinova

L. M., Bozzo E., Bulik T., Gies D. R., eds, Proceedings of the International Astronomical Union Symposia and Colloquia Vol. 346, High-mass X-ray Binaries: Illuminating the Passage from Massive Binaries to Merging Compact Objects. pp 449–454 (`arXiv:1811.03656`), doi:10.1017/S1743921318007433

Roche E., 1849, Académie des sciences et des lettres de Montpellier, 1, 243

Rodriguez C. L., Amaro-Seoane P., Chatterjee S., Rasio F. A., 2018, Phys. Rev. Lett., 120, 151101

Rodriguez C. L., Kremer K., Chatterjee S., Fragione G., Loeb A., Rasio F. A., Weatherford N. C., Ye C. S., 2021, Research Notes of the American Astronomical Society, 5, 19

Romero-Shaw I., Hirai R., Bahramian A., Willcox R., Mandel I., 2023, MNRAS, 524, 245

Röpke F. K., De Marco O., 2023, Living Reviews in Computational Astrophysics, 9, 2

Rosselli-Calderon A., Yarza R., Murguia-Berthier A., Rohoza V., Everson R. W., Antoni A., MacLeod M., Ramirez-Ruiz E., 2024, arXiv e-prints, p. arXiv:2404.08037

Safarzadeh M., 2020, ApJ, 892, L8

Samsing J., 2018, Phys. Rev. D, 97, 103014

Sana H., et al., 2012, Science, 337, 444

Sana H., et al., 2013a, in Pugliese G., de Koter A., Wijburg M., eds, Astronomical Society of the Pacific Conference Series Vol. 470, 370 Years of Astronomy in Utrecht. p. 141 (`arXiv:1211.4740`), doi:10.48550/arXiv.1211.4740

Sana H., et al., 2013b, A&A, 550, A107

Sand C., Ohlmann S. T., Schneider F. R. N., Pakmor R., Röpke F. K., 2020, A&A, 644, A60

Sanyal D., Grassitelli L., Langer N., Bestenlehner J. M., 2015, A&A, 580, A20

Scherbak P., Fuller J., 2023, MNRAS, 518, 3966

Schneider F. R. N., Podsiadlowski P., Langer N., Castro N., Fossati L., 2016, MNRAS, 457, 2355

Schneider F. R. N., Ohlmann S. T., Podsiadlowski P., Röpke F. K., Balbus S. A., Pakmor R., Springel V., 2019, Nature, 574, 211

Schneider F. R. N., Ohlmann S. T., Podsiadlowski P., Röpke F. K., Balbus S. A., Pakmor R., 2020, MNRAS, 495, 2796

Schrøder S. L., MacLeod M., Loeb A., Vigna-Gómez A., Mandel I., 2020, ApJ, 892, 13

Sen K., et al., 2023, A&A, 672, A198

Shiber S., Iaconi R., De Marco O., Soker N., 2019, MNRAS, 488, 5615

Shields J. C., Böker T., Ho L. C., Rix H.-W., van der Marel R. P., Walcher C. J., 2012, AJ, 144, 12

Sills A., Lombardi James C. J., 1997, ApJ, 484, L51

Smith N., et al., 2016, MNRAS, 458, 950

Soker N., 1992, ApJ, 399, 185

Soker N., 2017, MNRAS, 471, 4839

Soker N., 2022, Research in Astronomy and Astrophysics, 22, 055010

Staff J. E., De Marco O., Macdonald D., Galaviz P., Passy J.-C., Iaconi R., Low M.-M. M., 2015, MNRAS, 455, 3511

Staff J. E., De Marco O., Wood P., Galaviz P., Passy J.-C., 2016, MNRAS, 458, 832

Stevenson S., Vigna-Gómez A., Mandel I., Barrett J. W., Neijssel C. J., Perkins D., de Mink S. E., 2017, Nature Communications, 8, 14906

Suzuki T. K., Nakasato N., Baumgardt H., Ibukiyama A., Makino J., Ebisuzaki T., 2007, ApJ, 668, 435

Taam R. E., Ricker P. M., 2010, New Ast. Rev., 54, 65

Taam R. E., Sandquist E. L., 2000, ARA&A, 38, 113

Taam R. E., Bodenheimer P., Ostriker J. P., 1978, ApJ, 222, 269

Tauris T. M., Dewi J. D. M., 2001, A&A, 369, 170

Team COMPAS: Riley J., et al., 2022, ApJS, 258, 34

Terman J. L., Taam R. E., Hernquist L., 1995, ApJ, 445, 367

Thorne K. S., Żytkow A. N., 1975, ApJ, 199, L19

Thorne K. S., Żytkow A. N., 1977, ApJ, 212, 832

Timmes F. X., Swesty F. D., 2000, ApJS, 126, 501

Toonen S., Hamers A., Portegies Zwart S., 2016, Comput. Astrophys. & Cosm., 3, 6

Tout C. A., Wickramasinghe D. T., Lau H. H. B., Pringle J. E., Ferrario L., 2011, MNRAS, 410, 2458

Tout C. A., Zytkow A. N., Church R. P., Lau H. H. B., Doherty C. L., Izzard R. G., 2014, MNRAS, 445, L36

Tranin H., Webb N., Godet O., Quintin E., 2024, A&A, 681, A16

Turk M. J., Smith B. D., Oishi J. S., Skory S., Skillman S. W., Abel T., Norman M. L., 2011, ApJS, 192, 9

Tylenda R., Soker N., Szczerba R., 2005, A&A, 441, 1099

Tylenda R., et al., 2011, A&A, 528, A114

Vigna-Gómez A., et al., 2018, MNRAS, 481, 4009

Vigna-Gómez A., et al., 2020, PASA, 37, e038

Vigna-Gómez A., Wassink M., Klencki J., Istrate A., Nelemans G., Mandel I., 2022, MNRAS, 511, 2326

Walton D. J., Mackenzie A. D. A., Gully H., Patel N. R., Roberts T. P., Earnshaw H. P., Mateos S., 2022, MNRAS, 509, 1587

Webbink R. F., 1984, ApJ, 277, 355

Wilson E. C., Nordhaus J., 2019, MNRAS, 485, 4492

Wilson E. C., Nordhaus J., 2020, MNRAS, 497, 1895

Wolf B., Schwab J., 2017, wmwolf/py_mesa_reader: Interact with MESA Output, doi:10.5281/zenodo.826958

Wu S., Everson R. W., Schneider F. R. N., Podsiadlowski P., Ramirez-Ruiz E., 2020, ApJ, 901, 44

Xu X.-J., Li X.-D., 2010a, ApJ, 716, 114

Xu X.-J., Li X.-D., 2010b, ApJ, 722, 1985

Yarza R., et al., 2023, ApJ, 954, 176

Zalamea I., Beloborodov A. M., 2009, MNRAS, 398, 2005

Zevin M., et al., 2021, ApJ, 910, 152

Zhang W., Fryer C. L., 2001, ApJ, 550, 357

Zickgraf F. J., Kovacs J., Wolf B., Stahl O., Kaufer A., Appenzeller I., 1996, A&A, 309, 505

Zorotovic M., Schreiber M. R., Gänsicke B. T., Nebot Gómez-Morán A., 2010, A&A, 520, A86

de Kool M., 1990, ApJ, 358, 189

de Mink S. E., Sana H., Langer N., Izzard R. G., Schneider F. R. N., 2014, ApJ, 782, 7

van Rensbergen W., de Greve J.-P., 2021, Galaxies, 9, 19

van den Heuvel E. P. J., 1976, in Eggleton P., Mitton S., Whelan J., eds, IAU Symp. 73, Structure and Evolution of Close Binary Systems. Dordrecht: D. Reidel, p. 35

van den Heuvel E. P. J., Portegies Zwart S. F., de Mink S. E., 2017, MNRAS, 471, 4256

van der Walt S., Colbert S. C., Varoquaux G., 2011, Computing in Science & Engineering, 13, 22